

Dissertation zur Erlangung des Doktorgrades
der Fakultät für Chemie und Pharmazie
der Ludwig-Maximilians-Universität München

Iron-based Superconductors via Soft Chemistry

Gina Maya Friederichs
aus
Dachau, Deutschland

2015

Erklärung:

Diese Dissertation wurde im Sinne von §7 der Promotionsordnung vom 28. November 2011 von Herrn Prof. Dr. Dirk Johrendt betreut.

Eidesstattliche Versicherung:

Diese Dissertation wurde eigenständig und ohne erlaubte Hilfe erarbeitet.

München, den 27.05.2015

Gina Maya Friederichs

Dissertation eingereicht am: 09.06.2015

1. Gutachter: Prof. Dr. Dirk Johrendt

2. Gutachter: Prof. Dr. Hubert Huppertz

Mündliche Prüfung am: 30.06.2015

Danksagung

An dieser Stelle möchte ich mich bei allen Menschen bedanken, die mich bei dieser Arbeit unterstützt haben.

Mein besonderer Dank gilt hierbei Prof. Dr. Dirk Johrendt für die Aufnahme in seinen Arbeitskreis und die Möglichkeit dieses interessante Thema unter hervorragenden Bedingungen und großem Freiraum bearbeiten zu dürfen.

Prof. Dr. Hubert Huppertz danke ich sehr herzlich für die Übernahme des Zweitgutachtens.

Prof. Dr. Konstantin Karaghiosoff, Prof. Dr. Hendrik Zipse, Prof. Dr. Hans-Christian Böttcher und Prof. Dr. Andreas Kornath danke ich sehr herzlich, dass sie sich bereit erklärt haben an meinem Rigorosum teilzunehmen.

Ausserdem möchte ich mich bei den folgenden Personen bedanken:

Für die superherzliche Aufnahme in den AK und eine wirklich lustige und unvergessliche Zeit in vielerlei Hinsicht danke ich im Besonderen Rainer Frankovsky, Franziska Hummel, Marcus Tegel und Erwin Wiesenmayer.

Allen ehemaligen und aktuellen AK-Kollegen für das tolle, freundschaftliche Miteinander und die schöne Zeit: Daniel Bichler, Katharina Förg, Marianne Martin (geb. Rotter), Veronika Zinth, Constantin von Schirnding, Lola Lilenstein, Andreas Binek, Fabian Nitsche, Tina Markovic, Anne Schulz, Juliane Stahl, Lars Bulthaupt, Tobias Stürzer, Christine Stürzer (geb. Hieke), Roman Pobel, Simon Peschke, Ursula Pachmayr und Catrin Löhner.

Allen Mitgliedern der Arbeitskreise Schnick, Lotsch, Oeckler, Schmedt auf der Günne und Fässler (TU) für die gute Zusammenarbeit.

Meinen Bacheloranden und Praktikanten Christian Wagner, Yury Vilk, Matthias Wörsching und Katharina Iwan, für ihre tolle, engagierte Arbeit.

Prof. Dr. Rainer Pöttgen, Inga Schellenberg und Sirko Kamusella für Mößbauer Messungen;

Prof. Dr. Lorenz Kienle und Viola Duppel für TEM Messungen;

Prof. Dr. Jörn Schmedt auf der Günne und Christian Minke für NMR Messungen.

Ohne euch wäre mein Studium nicht mal halb so schön gewesen: Tanja Prommnitz, Johanna Haidt, Annette Frischmuth, Veronika Werner, Tobias Blümke, Ramona Pichl (geb. Branzan), Stefan Pichl und Florian Achrainier. Vielen Dank für die vielen unvergesslichen Momente!

Meiner Familie, im Besonderen meinen Eltern, Großeltern und meiner Schwester, danke ich von Herzen für die stetige Unterstützung und Ermutigung.

Mama und Schirin ich danke euch für das starke Band, das uns verbindet.

Danke Floh, für deine Geduld, dein Verständnis und die wunderschöne gemeinsame Zeit.

Wege entstehen dadurch, dass man sie geht.

Kafka

Table of Contents

1	Introduction.....	1
2	Preparative and analytical methods.....	5
2.1	Starting materials	5
2.2	Vacuum and inert gas line.....	6
2.3	Solid state reactions.....	6
2.4	Synthesis under mild conditions.....	6
2.5	X-ray powder diffraction	7
2.6	Energy dispersive X-ray analysis (EDX)	7
2.7	Magnetic measurements.....	7
2.8	Electrical resistivity	8
2.9	Mössbauer spectroscopy	9
2.10	Solid-state NMR.....	9
2.11	High resolution transmission electron microscopy (HRTEM).....	9
3	FeSe via metathesis	11
3.1	Introduction	11
3.2	Synthesis.....	12
3.3	Crystal structure.....	13
3.4	Magnetic measurements.....	16
3.5	Electrical resistivity	19
3.6	^{57}Fe -Mössbauer spectroscopy.....	20
3.7	Conclusion.....	23
4	Annealing effects in $\text{Fe}_{1+x}\text{Te}_{1-y}\text{Se}_y$ ($x = 0\text{-}0.1$, $y = 0.1\text{-}0.4$)	25
4.1	Introduction	25
4.2	Synthesis.....	26
4.3	Crystal structure.....	27
4.4	Magnetic measurements.....	30
4.5	Electrical resistivity	34
4.6	Conclusion.....	35
4.7	Appendix.....	37

5	K_{1-x}Fe_{2-y}Se₂ via reductive intercalation.....	43
5.1	Introduction.....	43
5.2	Synthesis.....	45
5.3	Crystal structure	46
5.4	Magnetic measurements	50
5.5	Electrical resistivity.....	52
5.6	Conclusion	53
6	NaFe_{1-y}Co_yAs	55
6.1	Introduction.....	55
6.2	Synthesis.....	56
6.3	Crystal structure	56
6.4	Magnetic measurements	58
6.5	Conclusion	59
7	Na_{1-x}Fe_{2-y}As₂ via oxidative deintercalation.....	61
7.1	Introduction.....	61
7.2	Synthesis.....	62
7.3	Crystal structure	63
7.4	Magnetic measurements	67
7.5	⁵⁷ Fe-Mößbauer spectroscopy.....	68
7.6	Solid state NMR spectroscopy.....	69
7.7	TEM measurements.....	70
7.8	Conclusion	72
8	Na(Fe_{1-y}Co_y)₂As₂ via oxidative deintercalation.....	75
8.1	Introduction.....	75
8.2	Synthesis.....	75
8.3	Crystal structure	75
8.4	Magnetic measurements	78
8.5	Electrical resistivity.....	79
8.6	Conclusion	80
9	Summary	81

Abbreviations	86
Bibliography.....	89
Full list of publications	97
Conference contributions.....	98
Curriculum Vitae	99

1 Introduction

Conventional solid state reactions have led to great achievements and highly fascinating materials during the last centuries, like e.g. high-temperature superconductors. However, such reactions often require high temperatures due to the slow diffusion of solid reactants. This favors thermodynamically stable products and prevents the formation of possible metastable phases with potentially new structures and properties. The latter are often accessible by soft chemistry routes, which proceed even at much lower temperatures and comprise a variety of reaction types like cationic exchange, dehydration, dehydroxylation, hydrolysis, metathesis, redox, intercalation or deintercalation reactions. A metathesis reaction utilizes the intrinsic available energy of the reaction partners in order to facilitate the conversion to the desired product.^[1] The common driving force in (solid state) metathesis reactions is the formation of co-formed salts such as alkaline halides.^[2]

Especially intercalation processes in lamellar host compounds like transition metal dichalcogenides (TMDs) and graphite have been in spotlight of science and technology since decades. In general good “host” lattices are layered compounds with only weak interlayer interactions (e.g. van der Waals). Thus, they can easily accommodate guests by offering the ability to adjust the interlayer separation depending on the size of the guest species. Relying on the properties of host and guest the intercalation process may range from molecular, ionic, redox rearrangement or chemically assisted to pseudo.^[3] The mechanism of an intercalation often proceeds via intermediates with different stoichiometry and ordering states. The final products depend on electronic aspects (band structure), electrostatic effects (attractive/repulsive Coulomb interactions) and strain energy (deformation of the host lattice upon intercalation), whereas the structural motifs of the precursor are preserved.^[4]

Possible guest species are H⁺, metal atoms or ions, molecular species or even polymers. As already mentioned, especially TMDs and graphite have been of great interest, because their intercalated compounds (TMDICs and GICs) revealed a variety of interesting physical properties like highly anisotropic electrical conductivity, phase transitions, charge density waves and superconductivity.^[4]

Superconductivity is a phenomenon fascinating scientists for more than 100 years. The discovery of high-temperature superconductivity in layered Fe-based compounds in 2008 represents the beginning of an unexpected new era in superconductor research. Like the cuprates, these materials are unconventional superconductors.^[5] Here, Cooper-pair formation occurs with the help of spin fluctuations but the mechanism is still not completely understood. Although both classes share similarities, their non-superconducting parent compounds significantly differ in their physical properties. While cuprates are Mott insulators with localized magnetic moments at the Cu sites,^[6] Fe-based compounds are semi-metals with only weak, itinerant magnetism.^[7] Contrary to copper oxide superconductors, Fe-based compounds are single-layer structures with one crystallographically independent iron atom per unit cell. However, often just multilayer copper oxides exhibit T_c s above the temperature of liquid nitrogen. Thus, higher critical temperatures are conceivable in multilayer iron-based materials. Artificial FeX multilayer superstructures seem possible by pulsed laser deposition methods,^[8, 9] but yield thin films only. Smart methods like soft chemistry routes may enable access to bulk multilayer superstructures.^[10]

Since the first discovery of superconductivity in fluorine doped LaOFeAs with a T_c of 26 K^[11] several classes of iron-based superconductors have been found. The unifying structural feature of all iron-based superconductors are layers of edge sharing tetrahedra consisting of FeX ($X = \text{Pnictide (Pn), Chalcogenide (Ch)}$) in which superconductivity emerges. These characteristic sheets are separated by more or less complex "building blocks" serving as spacer layers and result in different classes, categorized according to their stoichiometry. Referred to this nomenclature typical representatives are the 11- (FeCh , $Ch = \text{S-Te}$) without any atoms between the sheets, 111- ($A\text{FePn}$ ($A = \text{Alkaline metal}$)) with double layers of alkaline metals between the sheets, 122- ($A/\text{AEFe}_2\text{Pn}_2$, $A/\text{AEFe}_2\text{Ch}_2$ ($AE = \text{Earth alkaline metal}$)) with single layers of cations between the sheets and 1111-type compounds (REOFePn) with tetrahedral layers of REO^+ between the sheets. For $A/\text{AEFe}_2\text{Pn}_2$ only the higher homologues K-Cs and Ca-Ba are known. The smaller cations Li and Na do not form stable phases by conventional solid state reactions. Beside these, more complex structures like the so called 21311-, 32522-, 1038- or 1048-types have been explored.^[12, 13]

In general the stoichiometric parent compounds are not superconducting but exhibit a structural and magnetic (spin density wave, SDW) phase transition at low temperatures. These features are considered to be prerequisites for superconductivity but are not equally easy to detect in all classes and had led to conflicting results. However, they are by now confirmed for iron-pnictide superconductors of the 111-, 122-, and 1111-types. In these parent compounds superconductivity can be induced by pressure or substitution of atoms, either within the layers or indirectly in the spacer layers.

Unlike the Fe-pnictides, iron chalcogenides are often not strictly stoichiometric but exhibit interstitial Fe and/or vacancies crucially influencing the physical properties. Main representatives are 11- and 122-compounds, like FeSe ($T_c = 8 \text{ K}$), $\text{Fe}_{1+x}\text{Te}_{1-y}\text{Se}_y$ ($T_c \approx 9\text{-}15 \text{ K}$) and $\text{K}_{1-x}\text{Fe}_{2-y}\text{Se}_2$ ($T_c = 32 \text{ K}$).

The goal of this thesis was to develop new synthesis strategies for Fe-based superconductors by soft chemistry approaches to overcome difficulties occurring in conventional solid state synthesis on the one hand and to find new metastable, potentially multilayered phases on the other hand. Moreover, the physical properties of the obtained compounds were in the focus of interest.

In the conventional solid state synthesis of FeSe , a common difficulty is the formation of hexagonal FeSe along with the desired tetragonal β -phase. The latter is only stable at temperatures lower than $450 \text{ }^\circ\text{C}$. Thus, conventional synthesis of $\beta\text{-FeSe}$ requires long time annealing below this temperature. To overcome these difficulties a metathesis reaction under ambient conditions is presented in Chapter 3.

In FeSe isovalent substitution of Se with Te leads to $\text{Fe}_{1+x}\text{Te}_{1-y}\text{Se}_y$ with interstitial Fe, which interferes with superconductivity. Post-annealing around $300 \text{ }^\circ\text{C}$ under oxidative conditions improves the superconducting properties,^[14] whereby the mechanism remained unclear. For closer insights, such annealing effects and a possible reversibility under reductive conditions were investigated in Chapter 4.

Phase separation occurs in solid state synthesized $\text{K}_{1-x}\text{Fe}_{2-y}\text{Se}_2$ and the actual stoichiometry of the superconducting phase is subject of ongoing discussion. With its layered structure of uncharged sheets, aforementioned $\beta\text{-FeSe}$ represents an ideal host lattice, capable of accommodating guest species. Thus, the intercalation of K into

FeSe under mild conditions can potentially lead to phase pure $K_{1-x}Fe_{2-y}Se_2$ samples. Several solvent-based approaches, using different organic electron acceptor molecules to solve K, were studied in Chapter 5.

Influences on superconductivity due to substitution of Fe with Co in 111-type NaFeAs were investigated in Chapter 6.

The double layers of sodium atoms in NaFeAs and $NaFe_{1-y}Co_yAs$ could partly be deintercalated by mild oxidation. Removing e.g. half of the Na atoms might result in a new 122-compound. Hereby, the FeAs-layers would have to slide against each other, which could lead to intermediate states, as well. This could enable access to a new combined 111- and 122-type phase and would be a first step towards even more complex stacking sequences. Hence, Chapters 7 and 8 present solvent-assisted oxidative deintercalations in NaFeAs and $NaFe_{1-y}Co_yAs$.

2 Preparative and analytical methods

2.1 Starting materials

Commercially available materials used in this work are listed in Table 2.1 and Table 2.2 along with the supplier, purity and appearance.

Table 2.1 Commercially available inorganic chemicals used in this thesis.

Name	Formula	Supplier	Purity [%]	Appearance
Arsenic	As	Alfa Aesar	99.999	pieces
Barium	Ba	Sigma-Aldrich	99.99	pieces
Cobalt	Co	Sigma-Aldrich	99.9	powder
Iodine	I ₂	Alfa Aesar	99.9985	pieces
Iron	Fe	Chempur	99.9	powder
Iron (II) chloride	FeCl ₂	Sigma-Aldrich	99.9	beads
Hydrogen	H ₂	Air Liquide	99.9	gas
Lithium	Li	Sigma-Aldrich	99.99	ingot
Oxygen	O ₂	Air Liquide	n/s	gas
Potassium	K	Sigma-Aldrich	99.95	ingot
Selenium	Se	Chempur	99.999	pieces
Sodium	Na	Alfa Aesar	99.8	ingot
Tellurium	Te	Sigma-Aldrich	99.999	pieces

Table 2.2 Commercially available organic chemicals used in this thesis.

Name	Formula	Supplier	Purity [%]	Appearance
TEMPO	C ₉ H ₁₈ NO	BASF	98	pieces
15-crown-5	C ₁₀ H ₂₀ O ₅	Alfa Aesar	95	liquid
18-crown-6	C ₁₂ H ₂₄ O ₆	Alfa Aesar	95	pieces
Benzophenone	C ₁₃ H ₁₀ O	Acros Organics	99	pieces
Naphthalene	C ₁₀ H ₈	ABCR	99	pieces
Biphenyl	C ₁₂ H ₁₀	Sigma Aldrich	>99	pieces
THF	C ₄ H ₈ O	Fisher Scientific	99.99	liquid
Acetonitrile	CH ₃ CN	VWR	99.5	liquid

2.2 Vacuum and inert gas line

A combined vacuum and inert gas line was used with purified Ar (Argon 5.0, Air Liquide) as inert gas for handling air sensitive samples. The Argon was further dried by passing the gas through columns filled with BTS-catalyst (copper oxide dispersed on a ceramic carrier matrix, Fluka) kept at 120 °C, molecular sieve (pore size 0.4 nm, Merck) and phosphorous pentoxide on substrate (sicapent, Merck). The combined vacuum / inert gas line was connected to a oil vacuum pump reaching 1 x 10⁻³ mbar.

2.3 Solid state reactions

If not stated otherwise all elements or compounds for solid state reactions were weighed in under Ar-atmosphere in gloveboxes with O₂ and H₂O levels < 1ppm. Solid state reactions were performed in resistance furnaces with Pt/PtRh (type S) thermocouples and programmable PID temperature controllers (model 2408, Eurotherm). Annealing reactions up to 300 °C were performed with a Büchi glass oven (model B585) in sealed Duran ampoules. NaFe_{1-y}Co_yAs compounds were synthesized in Nb tubes, welded under Ar atmosphere with a electric arc melting apparatus.

2.4 Synthesis under mild conditions

All solvent-based reactions were carried out on a glass line using Schlenk's technique for handling air sensitive samples. Syntheses under mild conditions were either performed in 100 mL double neck flasks, connectable to a Schlenk frit or in Schlenk tubes (25-50 mL, Young valve). Glass ware were heated under vacuum three times prior to use. Initial weighing and transferring into the reaction vessel was performed in Ar filled gloveboxes with O₂ and H₂O levels < 1ppm. All further additions of air stable chemicals outside the glovebox were added in continuous Ar flow.

THF was dried over potassium or sodium and benzophenone in a solvent distiller stored under Ar. Physically solved oxygen in the solvent was degassed by directly passing Ar into THF for 1-2 h. The THF was freshly distilled prior to use and transferred with, an argon flushed, syringe.

2.5 X-ray powder diffraction

X-ray powder diffraction (XRPD) patterns were either recorded on HUBER G670 Guinier Imaging Plate Diffractometers with Cu or Co radiation, respectively (Cu-K α_1 , $\lambda = 154.051$ pm or Co-K α_1 , $\lambda = 179.02$ pm, Ge (111)-monochromator, silicon as external standard, oscillating flat sample holder, HUBER G670 Imaging Plate Guinier Camera control software)^[15] or on a STOE Stadi P (Mo-K α_1 radiation, Ge (111) monochromator, $\lambda = 70.93$ pm, silicon as external standard, rotating capillary (0.2-0.3 mm), WinXPOW software package).^[16] Rietveld refinements were performed with the TOPAS program package.^[17] Reflection profiles were generated by the fundamental parameters approach. A modified approach of Le Bail and Jounnaux was used to describe small peak half width and shape anisotropy effects. The preferred orientation of the crystallites was described with a spherical harmonics function. For capillary measurements an absorption correction was performed with estimated powder densities of approximately 60 % of the crystallographic density and the calculated linear absorption coefficient.

2.6 Energy dispersive X-ray analysis (EDX)

For scanning electron microscopy (SEM), a JEOL JSM-6500F scanning electron microscope with EDX detector (model 7418 OXFORD INSTRUMENTS) was used. The samples were sputtered with carbon (Sputter-machine: *BAL-TEC MED 020*, Co. BAL-TEC, Balzers, Netherlands). Data collection and evaluation was performed with the INCA software package.^[18]

SEM was also performed on a Carl Zeiss EVO-MA 10 with SE and BSE detectors, controlled by the SmartSEM^[19] software. The microscope was equipped with a Bruker Nano EDS detector (X-Flash detector 410-M) for EDS investigations using the QUANTAX 200^[20] software to collect and evaluate the spectra.

2.7 Magnetic measurements

A QUANTUM DESIGN MPMS XL5 SQUID magnetometer with the MPMS MultiVu software^[21] was used at temperatures between 1.8 and 380 K and magnetic fields

from 10 to \pm 50kOe. The polycrystalline samples were ground and filled into a gelatine capsule, which was fixed in a plastic straw. Susceptibilities under zero field cooled (zfc) and field cooled (fc) conditions were performed with magnetic fields of 15-30 Oe.

A fully automatic dual-coil AC susceptometer with sample transport for differential measurements was used at a temperature range between 3.5 and 300 K. The measurements were performed at 3.5 Oe (frequency 1333 Hz). The susceptometer consists of a JANIS SHI-950 two-stage closed-cycle Cryostate with ^4He exchange gas, a dual-channel temperature controller (model 332, LAKESHORE), a QUANTUM DESIGN DC-transport unit for sample centring and differential measurements and an EG&G (SIGNAL RECOVERY) 7260 DSP oscillator/lock-in amplifier. Coil assembly, stepper controller, sample holder, control software and further parts are developed by *M. Tegel*.^[22]

2.8 Electrical resistivity

The electrical resistance measurements were performed on the AC susceptometer mentioned above. A Keithley Source-Meter 2400 (Cleveland, U.S.A.) was available as current source. The differential voltage drop between signal-high and signal-low was recorded with a Keithley 2182 Nano-Voltmeter and used to calculate the sample resistance in one direction according to Ohm's law and the specific resistance according to the Van-der-Pauw approximation. For the measurements cold (if not stated otherwise) pressed (5 kN) pellets of respective samples (diameter, 4.0 mm; thickness, 0.3–1.2 mm) were produced. Applying the four-probe method, the pellet was contacted with four equidistant probes using silver conducting paint. All preparations were performed under inert atmosphere in a glovebox.

Semiconducting behavior could generally be described according to "variable range hopping" (VRH). Hereby the charge transport is caused by "hopping" of the charge carriers between localized states and the conductivity can be calculated from the hopping frequency:^[23]

$$\ln \sigma = A - BT^{-1/4} \quad \sigma: \text{conductivity}$$

Thus, VRH-conductivity is present when plotting $-\ln \sigma$ against $T^{-1/4}$ follows a linear slope. This rather simple mechanism was intentionally developed to amorphous materials but have sometimes produced conflicting results, which is why more complex revised models were established.^[24] Data within this work was evaluated with the simple VRH model in order to identify Mott insulators.

2.9 Mössbauer spectroscopy

For the ^{57}Fe -Mössbauer spectra a $^{57}\text{Co}/\text{Rh}$ source with an experimental line width $I_{\text{exp}} = 0.13 \text{ mm/s}$ was used. The sample was placed in thin-walled PVC containers at thicknesses of about $4\text{--}10 \text{ mg Fe/cm}^2$. The measurements were performed in transmission geometry at different temperatures. Fitting of the spectra was carried out with moessfit (by *S. Kamusella*, TU Dresden) or the NORMOS-90 program package^[25]

2.10 Solid-state NMR

NMR experiments were performed on a BRUKER AVANCEIII spectrometer equipped with an 11.7 T magnet and commercial magic-angle spinning probes. The samples were diluted with BaF_2 to allow sample spinning frequencies between 2 and 25 kHz in ZrO_2 rotors. In order that the spectra reflect the ^{23}Na central transitions only, the experimental conditions were adapted accordingly. T_1 relaxation time constants were obtained with the saturation recovery experiment. The chemical shift scale refers to 0.1 mol/L NaCl in D_2O at 0 ppm.

2.11 High resolution transmission electron microscopy (HRTEM)

SAED (selected area electron diffraction) and PED (precession electron diffraction, precession angle = 3°) were performed with a PHILIPS CM30 ST microscope (300 kV, LaB_6 cathode, CS = 1.15 mm). All manipulations for the preparation and transfer of the sample were carried out under Ar with the aid of a self-constructed device.^[26, 27] Simulations of HRTEM images (multislice formalism) were calculated with the EMS program package^[28] (spread of defocus = 70 Å, illumination semiangle = 1.2 mrad).

2 Preparative and analytical methods

All images were evaluated (including Fourier filtering) with the program Digital Micrograph 3.6.1 (Gatan). HRTEM images were filtered after Fourier transformation (ABSF). Elemental analyses by EDX were performed in the nanoprobe mode with a Si/Li detector (Noran NSF 7).

3 FeSe via metathesis

3.1 Introduction

β -FeSe exhibits the simplest structure among the iron-based superconductors. The compound with a tetragonal *anti-PbO*-type structure crystallizes in the space group $P4/nmm$ and consists of the typical structural feature in iron-based superconductors, edge sharing $FeCh_{4/4}$ tetrahedra sheets.^[29]

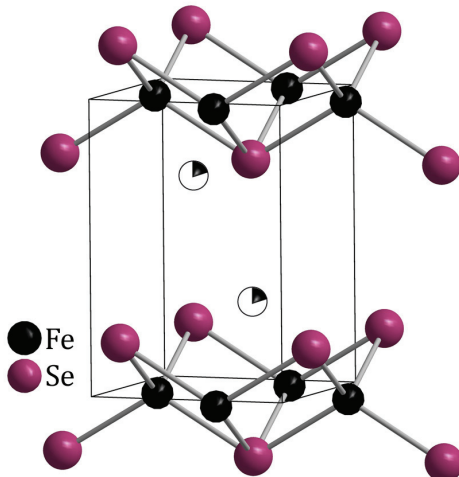


Figure 3.1 Crystal structure of β -FeSe, consisting of edge sharing $FeSe_{4/4}$ tetrahedra layers.

Hereby, up to $\sim 15\%$ interstitial Fe within the van der Waals gap between the layers can occur. These atoms are considered to interfere with superconductivity due to their magnetic moments. Like the parent compounds of iron pnictide superconductors, FeSe undergoes a structural phase transition from tetragonal ($P4/nmm$) to orthorhombic ($Cmme$) symmetry at around 100 K, but subsequently superconductivity emerges below 8-10 K,^[30] instead of magnetic ordering as in the pnictides. The superconducting properties of FeSe are highly sensitive to the stoichiometry, which is affected by the amount of interstitial iron as well as by vacancies within the layers.^[31, 32] By conventional high temperature synthesis of FeSe, the presence of some hexagonal α -FeSe can hardly be prevented since the β -phases stability range is below 450 °C.^[33] Hence, the tetragonal β -phase can only be obtained by long annealing below this temperature.

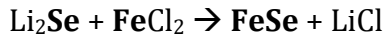
In order to overcome these difficulties, different synthesis methods, ranging from mild to extreme conditions, have been investigated and led to different physical properties. Depending on the synthesis conditions nanoparticles, monolayers/nanosheets or bulk samples were received. Bulk FeSe^[34, 35] has critical temperatures of 8-10 K^[30] which increases to 36 K under pressure^[36] and up to 45 K by intercalation of molecular spacer species.^[37-39] Thin films of FeSe obtained by molecular beam epitaxy (MBE) methods showed indications for critical temperatures (T_c) of up to 100 K.^[40-42] A superconducting-like transition at 30 K was found for FeSe nanoparticles synthesized under pressure and elevated temperatures.^[43]

Among these attempts, several solution based syntheses at mild conditions have been developed. Hereby, refluxing Fe(CO)₅ and Se in trioctylphosphinoxide^[44] or FeCl₂ or Fe(acac)₃ as iron sources in solvents like oleic acid, oleylamine, polyols or water, often under solvothermal conditions, were applied.^[45-49] However, reports about FeSe synthesized at mild conditions hardly found superconductivity, which was recently attributed to oxygen contaminations.^[50] Truly stoichiometric FeSe is metastable and is considered to lack superconductivity due to the exact composition of 1.0:1.0,^[49] while in tetragonal Fe_{1-x}Se phases different Fe-vacancy orders are thought to prevent superconductivity.^[51]

In order to obtain β -FeSe without hexagonal α -FeSe, a metathesis reaction under mild inert conditions in THF was analyzed. The results are discussed also with regard to the aforementioned unexpected properties of FeSe obtained by solvent-based syntheses.

3.2 Synthesis

FeSe was obtained by a two step synthesis via a THF-based metathesis reaction (Scheme 3.1). First, Li₂Se was synthesized from Se (1 eq) and Li (2 eq) with naphthalene (2 eq) in dry THF at room temperature by repeated ultrasonification and stirring for approximately 24 h based on a literature procedure.^[52] Li₂Se was washed twice with dry THF, dried and analyzed by XRPD. This reactive precursor was subsequently combined with FeCl₂ in dry THF.



Scheme 3.1 Formation of FeSe via a metathesis reaction.

The reaction mixture was ultrasonicated (10 min) and stirred for two days at room temperature or 0 °C. The suspension was allowed to settle, washed twice with dry THF in order to remove co-formed LiCl and dried *in vacuo*. FeSe was obtained as black, fine powdered solid which is highly air sensitive. Parts of the samples were further annealed at 200°C for 16-20 h in alumina crucibles in sealed Duran® ampoules. Annealing at higher temperatures (>300 °C) already led to the formation of significant amounts of hexagonal α -FeSe.

3.3 Crystal structure

The X-ray powder diffraction (XRPD) pattern shown in Figure 3.2 displays a large background and broad diffraction peaks. All peak positions are consistent with a tetragonal primitive unit cell (space group $P4/nmm$) and lattice parameters $a = 379.5(1)$ pm and $c = 550.8(4)$ pm, in agreement with those given for FeSe.^[30, 49]

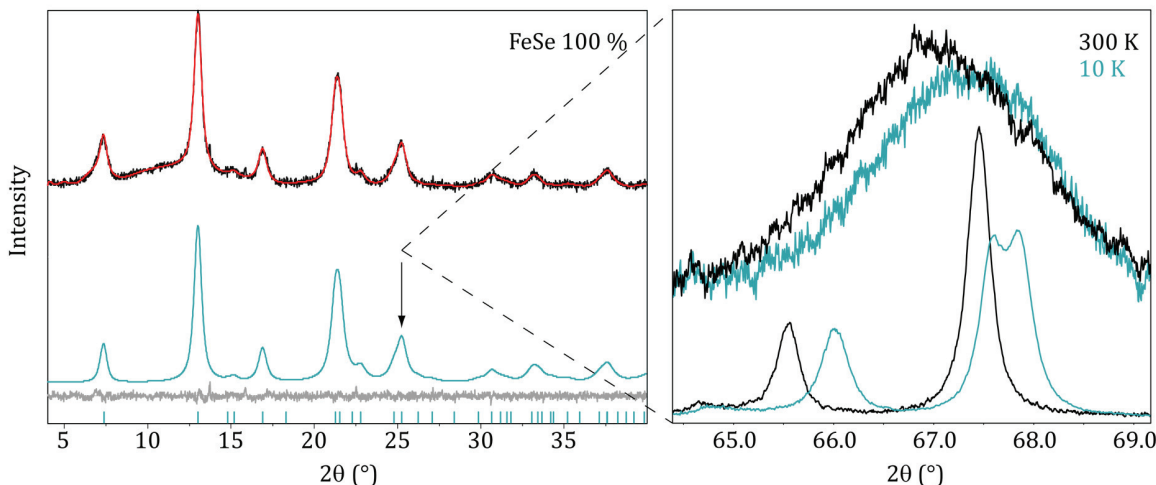


Figure 3.2 Left: X-ray powder diffraction pattern of annealed FeSe (Mo $K_{\alpha 1}$ radiation). Right: selected cutout from low temperature measurement (Co $K_{\alpha 1}$ radiation) where e.g. the reflection at 67.5 2 θ splits due to the structural transition to orthorhombic symmetry in conventionally synthesized FeSe (lower curves). Upper curves show the corresponding reflection from disordered FeSe.

However, the a -axis was found slightly longer and the c -axis slightly shorter than in the literature ($a = 377.3(1)$, $c = 552.6(1)$ pm).^[35] The elongated a -axis may be due to

strain caused by a small particle size and/or some vacancies on the Se-site. A distinctively increased a -axis of 390.5 pm was found in monolayer FeSe on a SrTiO₃ substrate, which is thought to originate from strain as consequence of lattice mismatch.^[53] Recently similar lattice parameter shifts have also been found by a solvent-based synthesis under hydrothermal conditions and were attributed to incorporation of oxygen species.^[50] While the reaction was performed under inert conditions, an oxygen contamination may have occurred during sample mounting for analytic measurements. Due to the very small particle size the FeSe presumably is highly air-sensitive. Refinement of the atomic sites indicated 10(4) % vacancies for Fe1, whereas the Fe2 site is occupied by 6(2) %. However, residual values remained nearly unaffected compared to full Fe1 and no Fe2 occupancy, indicating that the occupancies cannot reliably be refined due to the low degree of crystallinity. The resulting angles are rather regular with 110.1 (4x) and 108.3 (2x) (Table 3.1).

Table 3.1 Crystallographic details of FeSe.

Empirical formula	FeSe		
Diffractometer	Stoe Stadi P Mo K _{α1} , capillary 0.2 mm		
Radiation type	Mo K _{α1} $\lambda = 0.71073 \text{ \AA}$		
Space group	<i>P4/nmm</i> oc 2 ($Z = 2$)		
Lattice parameters (pm)	$a = 379.4(2)$ $c = 550.0(5)$		
Cell volume (\AA^3)	79.15(9)		
Atomic parameters	U_{iso} (\AA^2)		occupancies
Fe1 $2b (\frac{3}{4}, \frac{1}{4}, 0)$	0.051(5) ^a		0.90(4)
Fe2 $2c (\frac{1}{4}, \frac{1}{4}, z)$	z = 0.66(4)		0.06(2)
Se $2c (\frac{1}{4}, \frac{1}{4}, z)$	z = 0.250(3)		1.00(4)
Distances (\AA)	Angles		
Fe1-Se 2.34(1)	Se-Fe1-Se 110.1(3) (4x)		
Fe1-Fe1 2.682(1)	108.3(6) (2x)		
Fe1-Fe2 2.7(2)			
R_{wp} / R_p 1.100 / 0.870			
$\chi^2 / R_{\text{Bragg}}$ 1.022 / 0.029			

a Restrained as maximum value.

b constrained to Fe1 value

In consequence of the structural transition from tetragonal to orthorhombic symmetry at low temperatures, solid state synthesized FeSe shows the expected reflection splitting, visible in XRPD. This is depicted in Figure 3.2 (right) by the splitting of the reflection at $67.5\text{ }2\theta$ (lower curves). The broad reflection peaks in FeSe synthesized via metathesis prevent the detection of this transition (Figure 3.2, right, upper curves).

EDX measurements yielded a mean composition of $\text{Fe}_{1.0}\text{Se}_{0.89(6)}$ when Fe is fixed to 1. In different samples the oxygen content ranged from 0.3 to 0.6 referenced to a formula unit. The high air sensitivity of the product, prevents a reliable statement, if any oxygen is actually present within the sample as discussed in the literature.^[50] ICP measurements excluded a possible intercalation of Li-ions between the $\text{FeSe}_{4/4}$ sheets and further showed a slightly higher Fe content than Se. Thus, some vacancies on the Se-site and/or some interstitial Fe are possible. No changes concerning the crystal structure or composition were observed after annealing.

SEM images revealed tiny particles (Figure 3.3). Due to agglomeration no explicit size determination was possible. A representative particle with an approximate diameter of 250 nm is shown in Figure 3.3 (right).

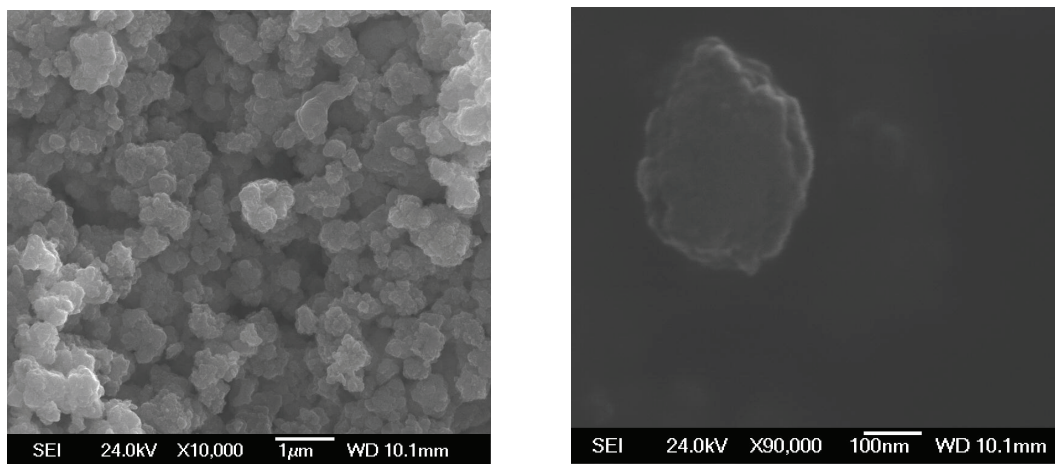


Figure 3.3 SEM images of FeSe (as-prepared).

TEM measurements could not be performed with accessible standard microscopes because of ferromagnetic properties that are present in all samples at room temperature. These may have been caused by a small magnetic impurity.

Future measurements on a special instrument equipped for magnetic samples could give more detailed insights to particle size and structure.

3.4 Magnetic measurements

The magnetic properties of FeSe, synthesized at 0 °C and 25 °C and of annealed samples, were investigated. Depending on the initial synthesis conditions, the samples showed slightly varying behavior at low temperatures. Consistently an anomaly around 100 K was visible in the field cooled part of the susceptibility of as-prepared samples (Figure 3.4, left). This effect can be attributed to the known structural transition, considered to be closely linked to the emergence of superconductivity.^[54, 55] In the field cooled part a broad decrease around 60 K is observed. Such behavior was repeatedly described in the literature for solvent-based synthesized FeSe and has been attributed to AFM ordering.^[44, 47, 50] Recent results indicate that this effect might be a consequence of the incorporation of oxygen or water.^[50] Contrary to former reports, the susceptibility shows negative values below 33 K (25 °C synthesis) in the actual measurement. This may indicate filamentary superconductivity. However, the simultaneous existence of superconductivity and AFM is rather unlikely, because these two effects are thought to be competitive in the FeSe system.^[56] Samples synthesized at 0 °C showed a small upturn of the zfc curve at low temperatures followed by a further decrease, unaltered at different magnetic fields. The other described effects became suppressed with higher fields (Figure 3.4). Splitting of zfc and fc curves over the hole temperature range indicate ferri- or ferromagnetism with T_C higher than 380 K and is commonly observed in solution-based synthesis of FeSe.^[50] As plausible impurity, elemental Fe is expected. This was already found in solid state synthesized samples of FeSe.^[57] Even smallest amounts may cause detectable magnetic signals far beyond detection limits of other analytical methods. By using FeCl_2 as starting material, an Fe impurity is not readily expected. However, Li_2Se could exhibit reducing properties and some FeCl_2 may be reduced to Fe^0 . Assuming that superconductivity causes the decreasing and negative susceptibility the very small volume fraction of ~1 % may arise by the presumed small particle size (~250 nm). Here, the London penetration depth of the magnetic field can become crucial and may minimize or even prevent superconductivity.

Typical penetration depths in metals like Sn or Nb are between 30 and 40 nm but in iron-based superconductors values even up to 1000 nm were determined.^[58] For FeSe_{0.85} a penetration depth of ~400 nm was found.^[59] With a size distribution around 250 nm as indicated by SEM, this scenario might become a valid assumption. However, it has to be stated, that the overall signal is very weak and may not be over-interpreted.

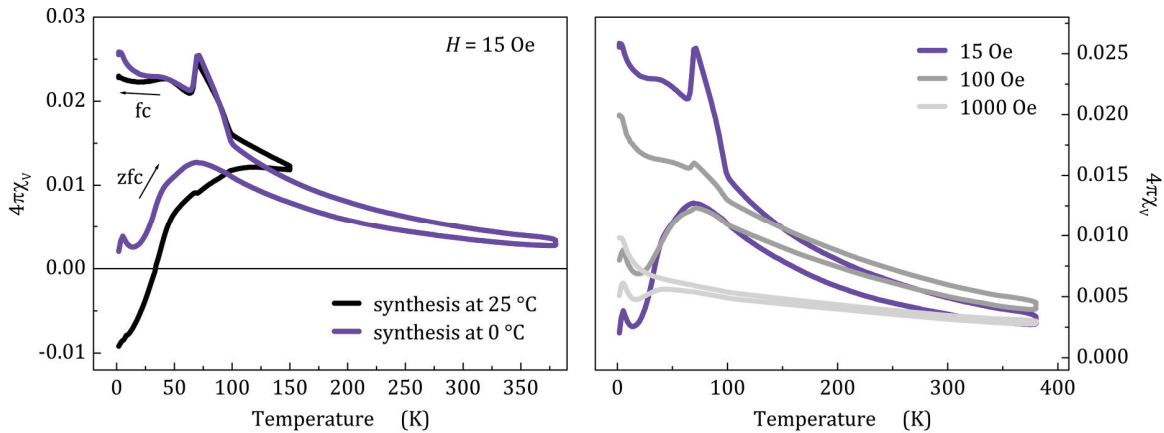


Figure 3.4 Magnetic susceptibility (zfc-fc) of FeSe. Left: Synthesized at 0 °C (blue) and 25 °C (black), right: Synthesized at 0 °C with different magnetic fields applied.

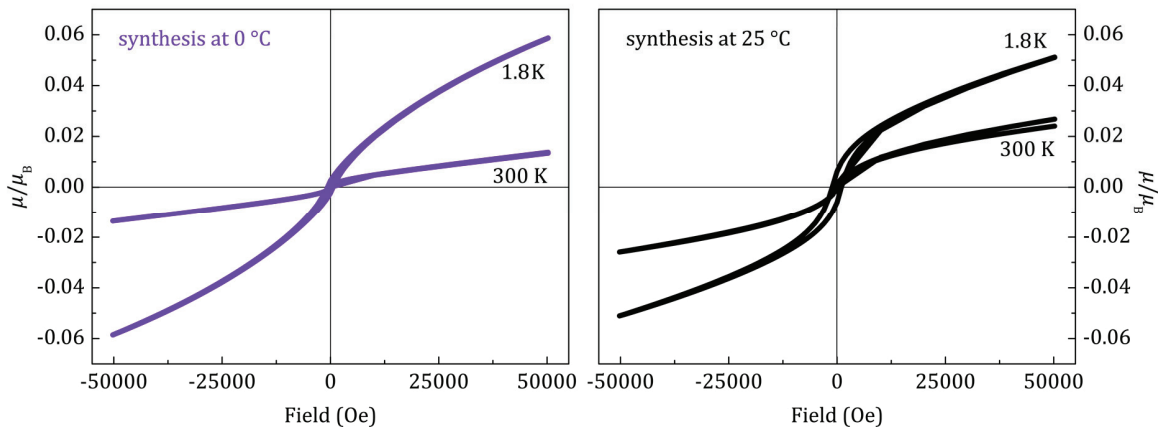


Figure 3.5 Isothermal magnetizations at 300 and 1.8 K. Left: Synthesized at 0 °C (blue); Right: Synthesized at 25 °C (black).

The isothermal magnetization measurements show very low values of only $0.06 \mu/\mu_B$, indicative for minimal amounts of a ferro- or ferrimagnetic impurity, represented by the s-shaped curve. Assuming e.g. Fe ($T_C = 1044$ K, $\mu = 2.2 \mu_B$) or Fe₃O₄ ($T_C = 858$ K, $\mu = 4.1 \mu_B$) to cause the ferromagnetic contribution, the amount was estimated to be 0.13 % (Fe) and 0.07 % (Fe₃O₄) for the synthesis at 0 °C and 0.48 % (Fe) and 0.26 % (Fe₃O₄) for the synthesis at room temperature. Small quantities of an iron oxide

impurity could occur due to the high air sensitivity of small sized FeSe particles with a large surface synthesized at ambient conditions.

Upon annealing the magnetic properties change. Susceptibilities now possess a drop around 120 K and one around 50 K, which were found more or less distinctive in different samples. Zfc and fc parts are again split over the whole temperature range. In Figure 3.6 the magnetic susceptibility of samples annealed 16 h, 20 h and 24 h are depicted. The decrease at 120 K was also found in other samples like β -FeSe, FeTe_{1-y}Se_y^[60-62] and FeTe_{1-y}S_y^[60-62] and likely could be the Verwey transition of Fe₃O₄.^[63] However, also hexagonal FeSe exhibits an anomalous spinfluctuation around this temperature, but is very unlikely to be formed under these mild conditions and was not detected by powder XRD. The drop around 50 K may still correspond with the decrease found in as-prepared samples, thus presumably represent AFM ordering. The black and blue curves in Figure 3.6 (left) exhibit negative susceptibilities below \sim 50 K (10 %) and \sim 110 K (5 %), respectively.

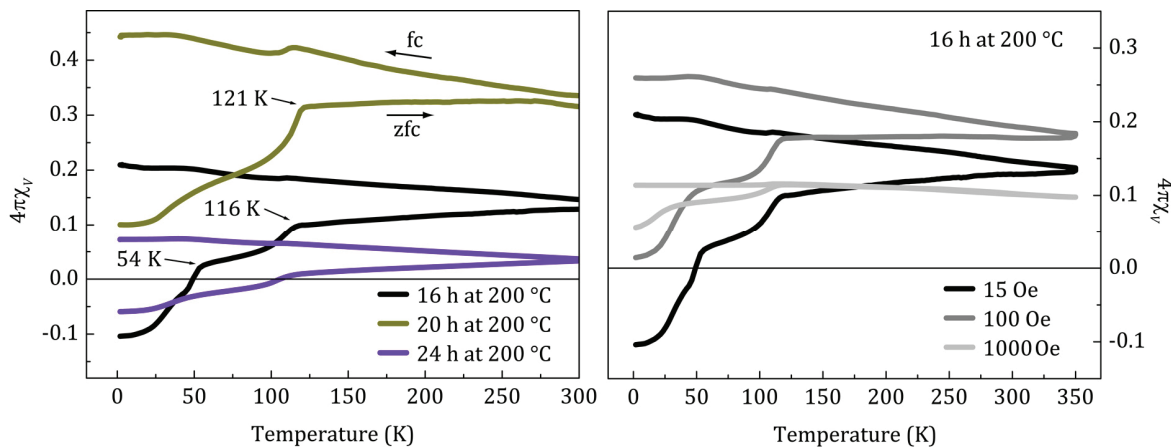


Figure 3.6 Magnetic susceptibility (zfc-fc) of FeSe annealed at 200 °C for 16, 20 and 24 h (left) and with different magnetic fields applied (right).

Both transitions are most obvious in the 16 h annealed sample. By applying larger fields the upper transition remains at 120 K, but less distinctive, whereas the transition at 50 K is shifted to temperatures as low as \sim 25 K. At 1000 Oe the splitting of the zfc and fc part is completely suppressed above 120 K (Figure 3.6, right). Negative susceptibilities may be caused by superconductivity or by a temperature dependent alignment of opposed oriented spin sublattices occurring e.g. in ferrimagnetic materials. The isothermal magnetization measurements indicate magnetic ordering which is already saturated by small fields (Figure 3.7), but still

with low moments not exceeding $0.1 \mu/\mu_B$. Extrapolated from the linear region (at high fields) of the isothermal magnetization at 300 K, the amount of the magnetic impurity was estimated to be approximately 1.5 % Fe_3O_4 (Figure 3.7, right).

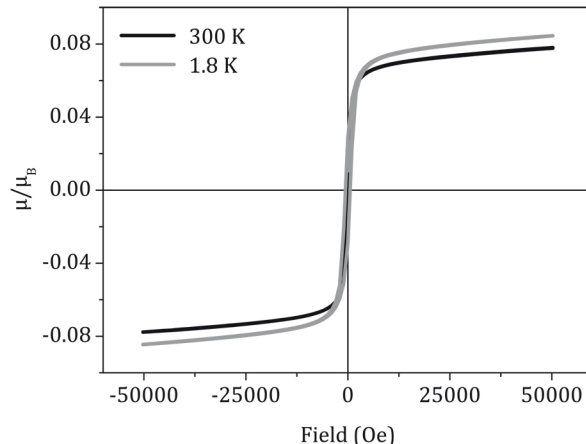


Figure 3.7 Isothermal magnetization at 300 and 1.8 K of FeSe annealed for 16 h.

If the sample is nano structured, also “nano-properties” such as superparamagnetism or a core-shell structure of FeSe core particles and an Fe_3O_4 shell must also be taken into account to cause the observed susceptibilities.

3.5 Electrical resistivity

Electrical resistivity measurements show metallic behavior at room temperature with conductivity values of 5.5×10^3 - 2.1×10^4 S/m. The resistivity increases at low temperatures, indicating semiconducting/insulating properties. In consequence of the assumed small particle size, a surface effect might explain this curvature, too. In this case the increase should be reduced by longer annealing times of the pellets due to a reduced surface. By comparing a sample annealed for 24 h with one annealed for 14 days, a 20 times higher relative resistivity for the long-annealed sample contrary to expectation becomes evident (Figure 3.8). Hence, a surface effect due to particle size can be considered as rather unlikely. Contrary to other reports, no problems concerning high resistivities at room temperature were observed.^[50] The resistivity course might be described by a Mott insulating state. Plotting $-\ln \sigma$ against $T^{-1/4}$ reveals a linear correlation as expected for Mott insulators (Figure 3.8, right).

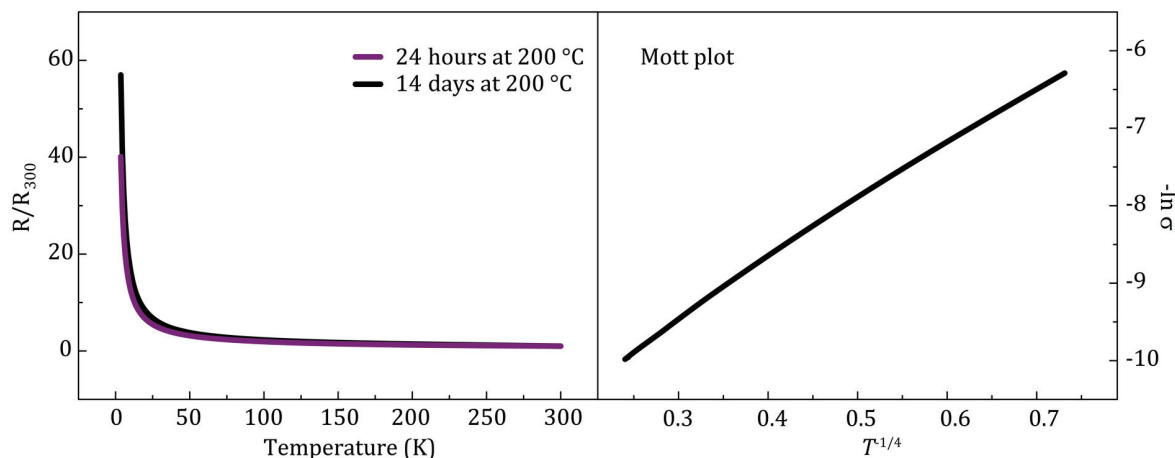


Figure 3.8 Left: Relative resistivity of pelletized, annealed FeSe. Pellet sintered for 24 h (purple) and 14 d (black). Right: Plot according to VRH (variable range hopping)-model by Mott.

3.6 ^{57}Fe -Mössbauer spectroscopy

^{57}Fe -Mössbauer spectroscopy was performed on as-prepared ($0\text{ }^\circ\text{C}$) and annealed FeSe. Crystalline Fe_{1+x}Se exhibits two different crystallographic sites for iron, one for Fe1 in the sheets and one for potential, interstitial Fe2 (Figure 3.9). Depending on the amount of interstitial iron, with ^{57}Fe -Mössbauer spectroscopy one to two iron environments can be observed. Disorder causes asymmetry in the signal by a distribution of centershift (CS) and quadrupol splitting (ΔE_Q) parameters and can be fitted by the maximum entropy method (MEM) (Figure 3.10).

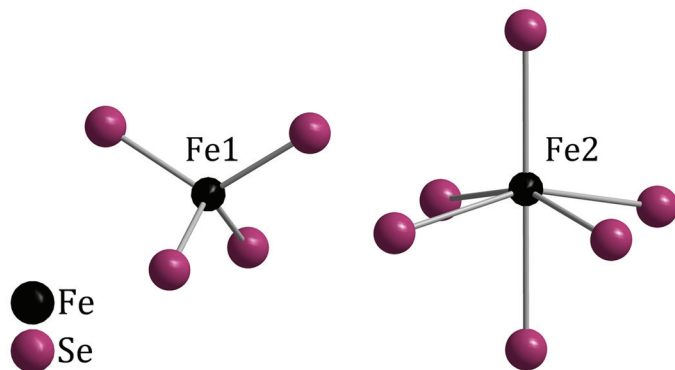


Figure 3.9 Coordination spheres for Fe1 and interstitial Fe2 .

Both FeSe samples showed a main doublet exhibiting asymmetry. A MEM-fit yielded a peak at 300 K with a distribution at center shifts consistent with literature (Figure 3.10a, b).[⁶⁴] The peak extends to larger field gradients and smaller center shifts (increased electron density at Fe) presumably caused by Se vacancies.

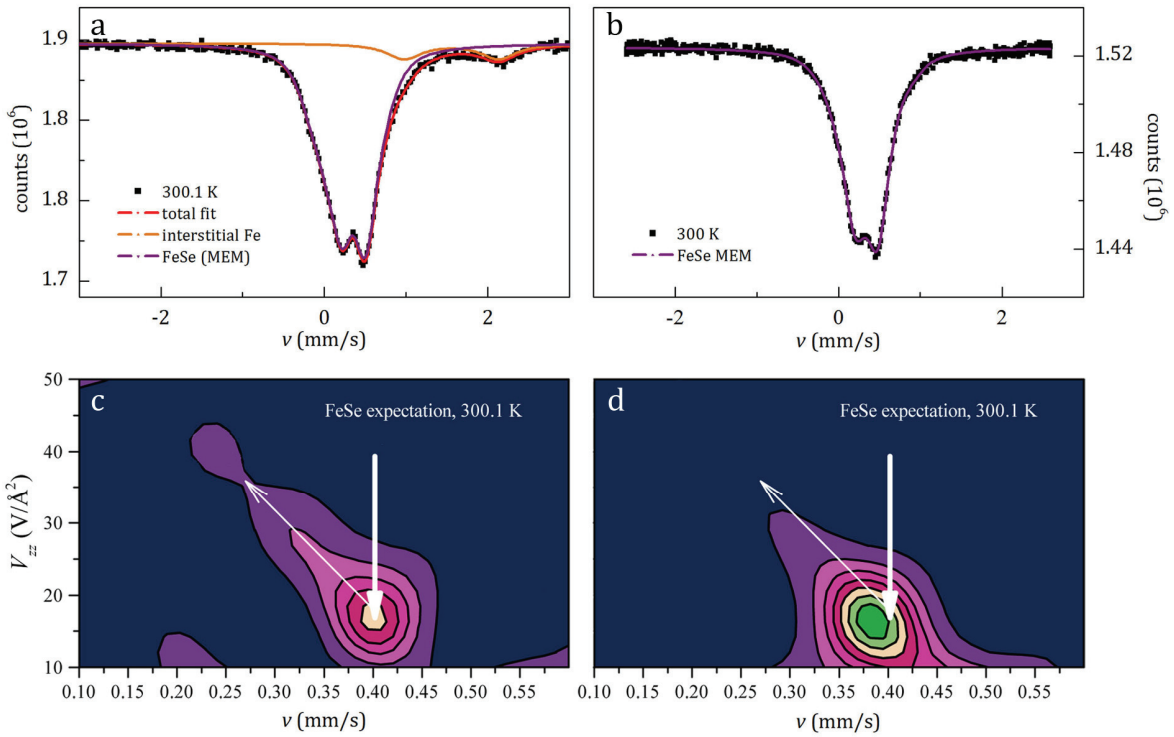


Figure 3.10 MEM fit for a) as-prepared FeSe b) annealed FeSe. Center shift distribution against field gradients V_{zz} for c) as-prepared FeSe d) annealed FeSe.

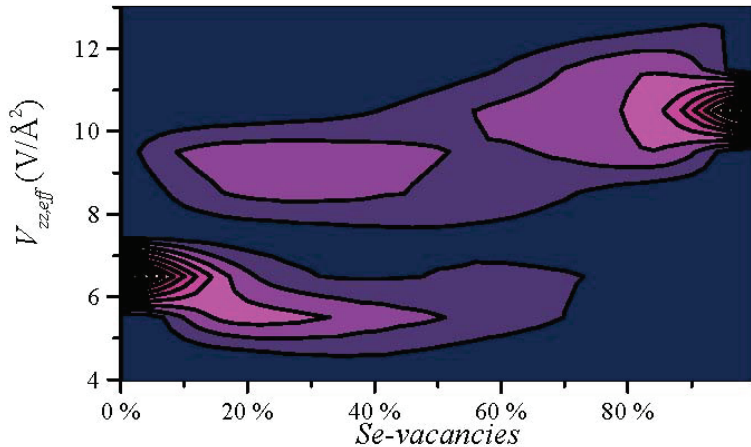


Figure 3.11 Qualitative dependence of $V_{zz,eff}$ and Se-vacancies.

Caused by Se vacancies and disorder many slightly different Fe environments are present. The effect is more distinct for as-prepared FeSe (Figure 3.10c), than for annealed FeSe (Figure 3.10d). Furthermore, a second doublet (10.5(2) %) is visible at 300 K around ($\text{CS} = 1.5 \text{ mm/s}$) and is presumably caused by interstitial Fe as mentioned above.

After annealing the main signal becomes sharper, reflecting a more homogeneous Fe environment. Thus, an explicit fit with single components is possible. The assumed

Se-vacancies generate a further signal with changed hyperfine parameters in addition to the main signal caused by tetrahedrally coordinated Fe without Se vacancies. The response of the field gradient was quantified according to Se vacancies using point charges Fe^{2+} and Se^{2-} with a variable vacancy quantity. The calculation was performed without considering excess Fe, with ± 5 unit cells in a -, b - and ± 2 unit cells in c -direction. Se was distributed randomly according to the number of Se vacancies with 100000 random arrangements (calculation by *Sirko Kamusella*, TU Dresden).

Figure 3.11 illustrates, that the typical vacancy vicinity shows an approximately doubled quadrupolar splitting compared to a fully occupied environment and justifies the inclusion of a further component for fitting the observed signal.

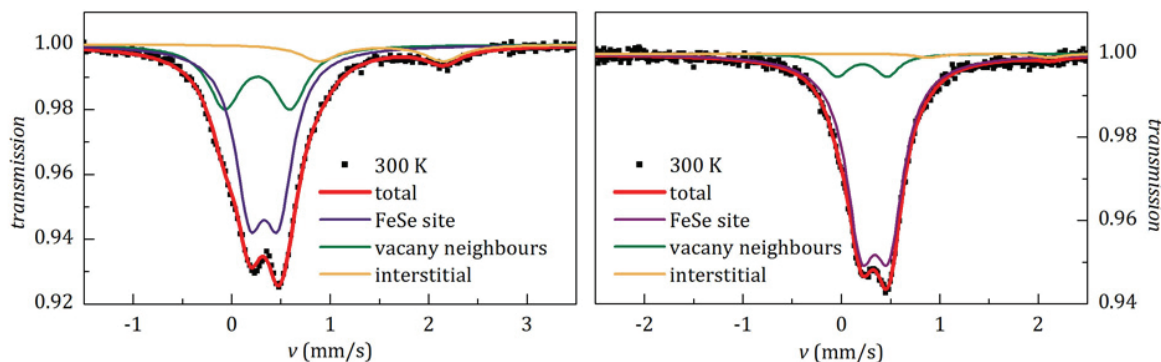


Figure 3.12 Three component fit consisting of signals from layer Fe (purple), layer Fe with Se vacancy neighbours (green) and interstitial Fe (yellow).

Thus, three components contribute to the observed signal. A main doublet ($\text{CS} = 0.46$, $\Delta = 0.26$) from Fe1 (purple curve, Figure 3.12), a second doublet ($\text{CS} = 0.32$, $\Delta = 0.51$) because of Se vacancy neighbours (green curve, Figure 3.12) and a third doublet ($\text{CS} = 1.5$ mm/s) from interstitial Fe2 (yellow curve, Figure 3.12). The latter was included with fixed hyperfine parameters determined from the as-prepared sample (10.5(2) %) and was quantified to decrease to 1.8(2) % upon annealing. For as-prepared FeSe this already gives a reasonable fit. However, a MEM fit describes the observed signal more precisely. For annealed FeSe this three components fit describes the signal quite well. At 300 K no indication for magnetic ordering is given.

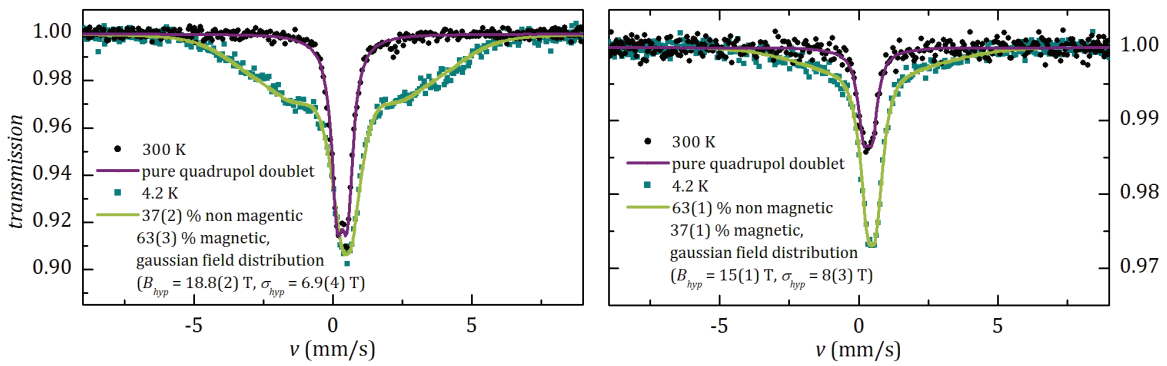


Figure 3.13 ^{57}Fe -Mössbauer signal at 300 K (black) and at 4.2 K (dark green) for as-prepared (left) and annealed (right) FeSe.

At 4.2 K large parts of the sample are magnetically ordered. The signal of as-prepared FeSe is composed of a paramagnetic doublet (37(2) %) and a broad background from a distribution of internal fields caused by magnetically ordered fractions (63(3) %). The magnetic component decreases to 37(1) % by annealing, while the magnetic parameters remain nearly constant in both samples. The main doublet is broadened by up to 25 % at low temperatures presumably due to the sense of stray fields. Thus, in as-prepared FeSe the main part of Fe orders magnetically, but with many slightly deviating environments due to Se vacancy neighbours and disorder. This is in contrast to solid state synthesized superconducting FeSe, where no magnetic moment was observed.^[64, 65]

3.7 Conclusion

β -FeSe without any hexagonal α -phase was successfully synthesized by a metathesis reaction at room temperature in THF. The compound exhibits disorder accompanied by Se vacancies. At low temperatures, large fractions of FeSe order magnetically, contrary to conventional FeSe, which is a nonmagnetic 8 K superconductor. By annealing, FeSe synthesized via metathesis, becomes more homogeneous and less magnetic. Most likely, FeSe orders antiferromagnetically below 50 K in agreement with recent literature results.^[50] Oxygen or H₂O incorporation as discussed in this reference seems plausible but cannot be verified from present data. However, this interesting new aspect should be investigated in more detail in future studies, since it seems to crucially influence the physical properties of FeSe. By future TEM measurements particle size and accurate structural features could be determined.

Neutron and/or μ SR experiments could give detailed insights into the magnetism. By using Li₂S or Li₂Te the synthesis might also be adapted to obtain tetragonal FeS and FeTe which could be appealing since tetragonal FeS cannot be obtained by a conventional solid state synthesis, but represents an interesting starting material to obtain new Fe-based superconductors.

4 Annealing effects in $\text{Fe}_{1+x}\text{Te}_{1-y}\text{Se}_y$ ($x = 0\text{-}0.1$, $y = 0.1\text{-}0.4$)

Parts of this chapter are published and reprinted with permission from G. M. Friederichs, M. Wörsching, D. Johrendt, *Supercond. Sci. Technol.* **2015**, 28, 095005. Copyright © 2015 IOP PUBLISHING, LTD; DOI: 10.1088/0953-2048/28/9/095005 <http://stacks.iop.org/0953-2048/28/095005>

4.1 Introduction

Superconducting iron chalcogenides FeCh ($\text{Ch} = \text{Se}, \text{Te}$) attract considerable interest because their simple *anti-PbO*-type crystal structures make them perfect candidates for studying unconventional superconductivity,^[66, 67] and recent reports indicate critical temperatures (T_c) up to 100 K in single-layer FeSe films.^[40-42]

Between the edge sharing $\text{FeCh}_{4/4}$ tetrahedral sheets interstitial Fe atoms of up to 25% are present (Figure 4.1).^[29]

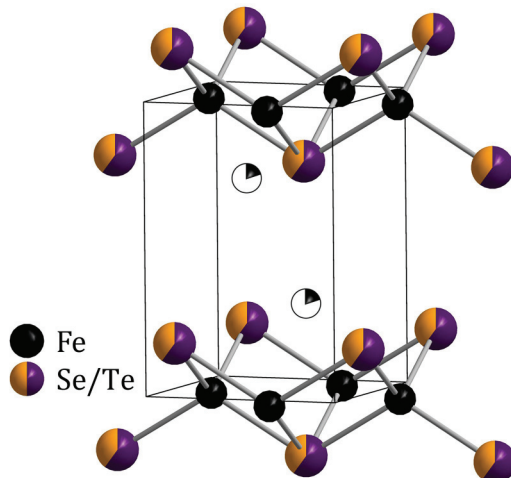


Figure 4.1 Crystal structure of $\text{Fe}_{1+x}\text{Te}_{1-y}\text{Se}_y$ (*anti-PbO*-type, space group $P4/nmm$).

The latter interfere with superconductivity by their magnetic moments and/or their unfavorable contributions to the Fermi surface. Bulk FeSe ^[34, 35] has critical temperatures of 8-10 K^[30] which increases to 36 K under pressure,^[36] while Fe_{1+x}Te is magnetic and non superconducting.^[67, 68] Only thin films of Fe_{1+x}Te become superconducting after O_2 -annealing.^[69] The amount of interstitial iron is considered as key factor for the differences in the physical properties of Fe_{1+x}Se and Fe_{1+x}Te .^[31, 32]

^{70]} While stoichiometric FeSe is accessible, a respective FeTe does not exist.^[49] In Fe_{1+x}Te , isovalent substitution of sulfur or selenium for Te induces superconductivity depending on the amount of interstitial iron.^[71\text{-}73] Optimal superconductivity within the solid solution is found around $y = 40\text{-}50\%$ with a T_c of 14 K.^[71] At higher Se contents a miscibility gap prevents homogeneous powder samples.^[74] Different post-preparation manipulations revealed a significant influence on the superconducting properties of the solid solution $\text{FeTe}_{1-y}\text{Se}_y$. These manipulations include exposure to alcoholic beverages^[75], HNO_3 ^[76], I_2 ^[75, 77], O_2 ^[14], Te^[78] and S^[79] at ambient conditions or annealing at higher temperatures as well as under N_2 ^[75] and vacuum^[80]. Especially annealing $\text{Fe}_{1+x}\text{Te}_{1-y}\text{Se}_y$ single crystals in an oxygen-containing atmosphere increased the superconducting properties significantly. As-prepared samples are superconducting only for $y = 0.5$, whereas after O_2 -annealing already compounds with $y = 0.1$ are superconducting.^[14] Since then, the mechanism of O_2 -annealing has been debated. Several assumptions including a homogenization effect, the substitution of O for Se, the intercalation of oxygen or the removal of interstitial Fe, were considered reasonable, whereby the latter is discussed preferentially.^[14, 69] Recently the removal of excess iron from a $\text{Fe}_{1+x}\text{Te}_{0.6}\text{Se}_{0.4}$ single crystal was monitored by STM measurements.^[81] However, it remains unclear, what happens with that iron and if the process is solely the removal of interstitial iron while the layer iron is unaffected. Maybe it is more complex and possibly a reversible process under reductive conditions in hydrogen atmosphere.

Here, polycrystalline $\text{Fe}_{1+x}\text{Te}_{1-y}\text{Se}_y$ ($x = 0, 0.1, y = 0.1\text{-}0.4$) with different amounts of nominal interstitial iron are investigated. The examinations were aimed to clarify the influences of oxygen- and hydrogen-annealing on the superconducting properties. If the extraction of interstitial Fe atoms is essential, the emergence of iron oxide as impurity phase can be expected in polycrystalline samples and the process should not be reversible under reductive conditions in contrast to an intercalation or substitution of oxygen.

4.2 Synthesis

$\text{Fe}_{1+x}\text{Te}_{1-y}\text{Se}_y$ ($x = 0\text{-}0.1, y = 0.1\text{-}0.4$) compounds were synthesized by using stoichio-

metric amounts of the elements. These samples will be referred to as "as-prepared" in

the following. For the synthesis of $\text{Fe}_{1.0}\text{Te}_{1-y}\text{Se}_y$ ($y = 0.1\text{-}0.4$) the samples (0.7 g) were heated to 1050 °C for 24 h, cooled down to 350 °C, kept there for 10 h and then cooled down to room temperature (step 1). Four samples were combined and annealed at 800 °C for 10 h followed by 10 h at 350 °C before cooling to room temperature (step 2). $\text{Fe}_{1.1}\text{Te}_{1-y}\text{Se}_y$ ($y = 0.1\text{-}0.4$) was synthesized in one step according to step 1 on a larger scale (2.0 g). Oxygen annealing was performed by heating samples to 300 °C for 2 h in alumina crucibles inside sealed Duran® glass ampoules under oxygen atmosphere (“O₂-annealed” samples). For hydrogen annealing, O₂-conducted samples in alumina crucibles inside a Duran tube connected to a bubble counter were heated to 200 °C for 2 h under a continuous flow of hydrogen (“H₂-annealed” samples). In order to exclude the changing properties to be annealing effects only, control experiments under Ar atmosphere were performed (2 h, 300 °C).

4.3 Crystal structure

The as-prepared, O₂- and subsequently H₂-annealed $\text{FeTe}_{1-y}\text{Se}_y$ and $\text{Fe}_{1.1}\text{Te}_{1-y}\text{Se}_y$ samples were analyzed by XRPD (Figure 4.2, Figure 4.3). Like Fe_{1+x}Te and FeSe , $\text{FeTe}_{1-y}\text{Se}_y$ crystallizes in the $\alpha\text{-PbO}$ -type structure ($P4/nmm$). With increasing Se content, reflections of the $\text{FeTe}_{1-y}\text{Se}_y$ phases are shifted to higher 2θ values, respectively, due to the smaller ionic radius of Se compared to Te.

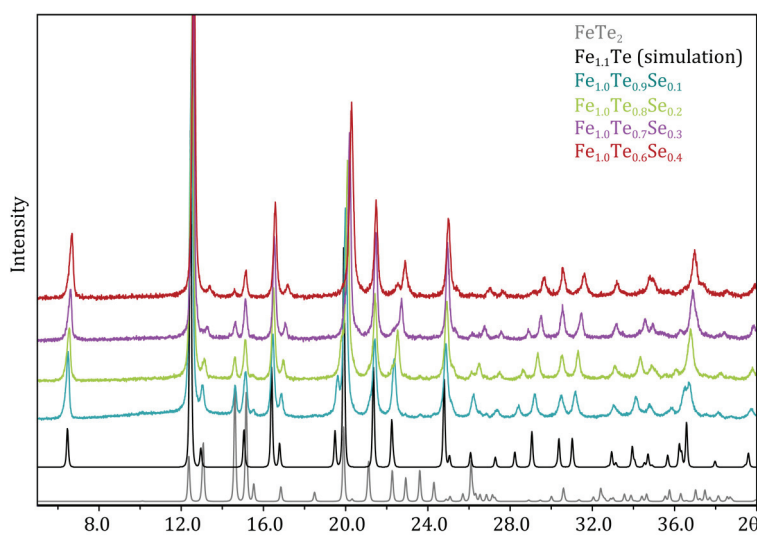


Figure 4.2 XRPD patterns of as-prepared $\text{FeTe}_{1-y}\text{Se}_y$ phases and simulated data for FeTe and FeTe_2 .

A minor impurity occurring in all as-prepared $\text{FeTe}_{1-y}\text{Se}_y$ samples can be assigned to orthorhombic FeTe_2 (Figure 4.2) absent in $\text{Fe}_{1.1}\text{Te}_{1-y}\text{Se}_y$. By using 10 % excess Fe, phase pure samples, according to XRPD can be obtained (Figure 4.3, green curve). Comparing as-prepared with O_2 - and subsequently H_2 -annealed samples reveal some minor changing intensity ratios along with an increase ($\text{FeTe}_{1-y}\text{Se}_y$) or evolution ($\text{Fe}_{1.1}\text{Te}_{1-y}\text{Se}_y, y = 0.1, 0.2$) of FeTe_2 (asterisks), as can be seen in Figure 4.3. The crystallographic details for all samples after Rietveld refinements are summarized in Table 4.2 - Table 4.9 (Chapter 4.7). In general the refinements possessed a tendency to poorer residual values upon annealing. While lattice parameter a decreases slightly (~0.4 %) with increasing Se content (values of EDX measurements), lattice parameter c decreases stronger by ~2.7 %, as expected. After annealing, small deviations not exceeding 0.1 % were determined (Figure 4.4 left). O_2 -annealed $\text{FeTe}_{1-y}\text{Se}_y$ samples (purple symbols, Figure 4.4 right) revealed reduced interstitial Fe contents compared to as-prepared samples (black and gray symbols, Figure 4.4 right). In the H_2 -annealed samples no clear tendency can be observed anymore.

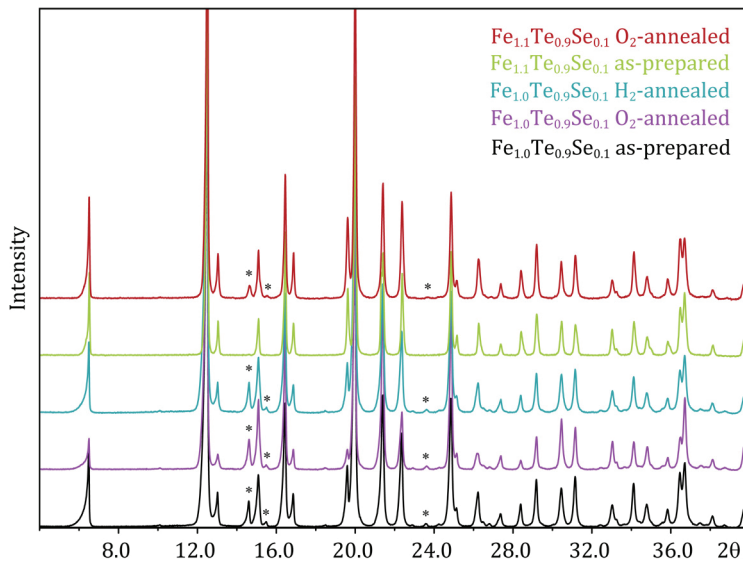


Figure 4.3 XRPD patterns of as-prepared, O_2 -annealed and H_2 -annealed $\text{FeTe}_{0.9}\text{Se}_{0.1}$.

Interestingly for $\text{Fe}_{1.1}\text{Te}_{1-y}\text{Se}_y$ the iron content is found constantly high upon annealing. Small changes of interstitial iron quantities are unreliablely detectable by XRPD because of very weak scattering of the only ≈ 10 % occupied $\text{Fe}2$ ($2c$ site). Furthermore the oxygen treatment likely proceeds from the surface leading to inhomogeneous particles.^[81] For chalcogen atoms a split position was used in order

to describe the geometrical vicinity accurately. The bond distance of Fe1-Se ($\sim 2.4 \text{ \AA}$) is found $\sim 0.2 \text{ \AA}$ shorter than for Fe1-Te (2.6 \AA) in agreement with single crystal data.^[82] The resulting "chalcogen heights" are therefore around $h_{\text{Se}} \sim 1.5 \text{ \AA}$ and $h_{\text{Te}} \sim 1.7 \text{ \AA}$.

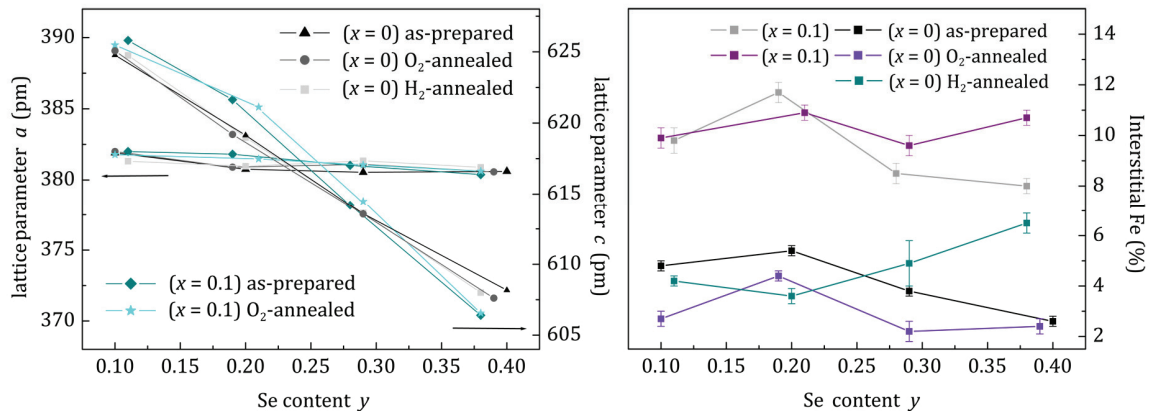


Figure 4.4 Lattice parameters obtained from Rietveld refinements of as-prepared and annealed $\text{Fe}_{1+x}\text{Te}_{1-y}\text{Se}_y$ (left) and refined amounts of interstitial iron in $\text{Fe}_{1+x}\text{Te}_{1-y}\text{Se}_y$ before and after annealing.

The compositions were determined by careful EDX analysis. The results are given as ratio of Fe to chalcogen (Te and Se) and the sum of Se to Te was constrained to 1 (see Table 4.1). The iron contents of O_2 -annealed samples are slightly reduced while selenium and tellurium contents are unaffected. Most significant is the large amount of 20-30% oxygen in all phases after O_2 -annealing (see Table 4.1).

Table 4.1 Composition of as-prepared, O_2 - and subsequently H_2 -annealed $\text{Fe}_{1+x}\text{Te}_{1-y}\text{Se}_y$ ($x = 0, 0.1, y = 0.1\text{-}0.4$) determined by EDX.

Nominal Composition	Measured as-prepared	Measured O_2 -annealed	Measured H_2 -annealed
$\text{FeTe}_{0.9}\text{Se}_{0.1}$	$\text{Fe}_{1.03}\text{Te}_{0.90}\text{Se}_{0.10}(\text{O}_{0.01})$	$\text{Fe}_{1.01}\text{Te}_{0.90}\text{Se}_{0.10}(\text{O}_{0.24})$	$\text{Fe}_{1.03}\text{Te}_{0.89}\text{Se}_{0.11}(\text{O}_{0.24})$
$\text{FeTe}_{0.8}\text{Se}_{0.2}$	$\text{Fe}_{1.07}\text{Te}_{0.80}\text{Se}_{0.20}(\text{O}_{0.02})$	$\text{Fe}_{1.02}\text{Te}_{0.81}\text{Se}_{0.19}(\text{O}_{0.20})$	$\text{Fe}_{0.99}\text{Te}_{0.80}\text{Se}_{0.20}(\text{O}_{0.25})$
$\text{FeTe}_{0.7}\text{Se}_{0.3}$	$\text{Fe}_{1.03}\text{Te}_{0.71}\text{Se}_{0.29}(\text{O}_{0.04})$	$\text{Fe}_{0.99}\text{Te}_{0.71}\text{Se}_{0.29}(\text{O}_{0.35})$	$\text{Fe}_{0.97}\text{Te}_{0.71}\text{Se}_{0.29}(\text{O}_{0.25})$
$\text{FeTe}_{0.6}\text{Se}_{0.4}$	$\text{Fe}_{1.06}\text{Te}_{0.60}\text{Se}_{0.40}(\text{O}_{0.02})$	$\text{Fe}_{1.02}\text{Te}_{0.61}\text{Se}_{0.39}(\text{O}_{0.19})$	$\text{Fe}_{1.01}\text{Te}_{0.62}\text{Se}_{0.38}(\text{O}_{0.15})$
$\text{Fe}_{1.1}\text{Te}_{0.9}\text{Se}_{0.1}$	$\text{Fe}_{1.09}\text{Te}_{0.89}\text{Se}_{0.11}(\text{O}_{0.02})$	$\text{Fe}_{1.05}\text{Te}_{0.90}\text{Se}_{0.10}(\text{O}_{0.32})$	-
$\text{Fe}_{1.1}\text{Te}_{0.8}\text{Se}_{0.2}$	$\text{Fe}_{1.11}\text{Te}_{0.81}\text{Se}_{0.19}(\text{O}_{0.02})$	$\text{Fe}_{1.07}\text{Te}_{0.79}\text{Se}_{0.21}(\text{O}_{0.25})$	-
$\text{Fe}_{1.1}\text{Te}_{0.7}\text{Se}_{0.3}$	$\text{Fe}_{1.10}\text{Te}_{0.72}\text{Se}_{0.28}(\text{O}_{0.01})$	$\text{Fe}_{1.08}\text{Te}_{0.71}\text{Se}_{0.29}(\text{O}_{0.20})$	-
$\text{Fe}_{1.1}\text{Te}_{0.6}\text{Se}_{0.4}$	$\text{Fe}_{1.11}\text{Te}_{0.62}\text{Se}_{0.38}(\text{O}_{0.01})$	$\text{Fe}_{1.08}\text{Te}_{0.62}\text{Se}_{0.38}(\text{O}_{0.21})$	-

This indicates oxidic species at the surfaces of the particles. If these are at least partially iron oxides, the iron content inside the O_2 -annealed particles is lower than given in Table 1 because EDX cannot discriminate iron in the surface oxide and in $\text{Fe}_{1+x}\text{Te}_{1-y}\text{Se}_y$. In case of $\text{Fe}_{1.1}\text{Te}_{1-y}\text{Se}_y$ isolated spots showed nearly 100 % iron, indicating some residual elemental iron due to the 10% excess Fe used.

Forcing the reaction in a continuous oxygen flow for 2 h at 300 °C instead of static O_2 pressure in sealed ampoules partly decomposes $\text{FeTe}_{1-y}\text{Se}_y$ to impurity phases. Among them, FeTe_2 and iron oxides, discernible in XRPD. These findings are consistent with recent results by *Sun et al.* who over-annealed single crystals of $\text{Fe}_{1+x}\text{Te}_{0.6}\text{Se}_{0.4}$ at 400 °C.^[81]

4.4 Magnetic measurements

Magnetic measurements were performed in order to investigate the changes of the superconducting properties of $\text{Fe}_{1+x}\text{Te}_{1-y}\text{Se}_y$ by annealing under different conditions. Figure 4.5 shows the susceptibilities of as-prepared, Ar-annealed, O_2 -annealed and H_2 -annealed $\text{FeTe}_{1-y}\text{Se}_y$ ($y = 0.1, 0.2, 0.3, 0.4$). While as-prepared $\text{FeTe}_{0.9}\text{Se}_{0.1}$ is not superconducting, $\text{FeTe}_{0.8}\text{Se}_{0.2}$ and $\text{FeTe}_{0.7}\text{Se}_{0.3}$ exhibit rather weak superconducting transitions of 8.8 K and 9.7 K, respectively. In as-prepared $\text{FeTe}_{0.6}\text{Se}_{0.4}$ bulk superconductivity with $T_c = 14.4$ K is observed (see filled circles Figure 4.5 left).

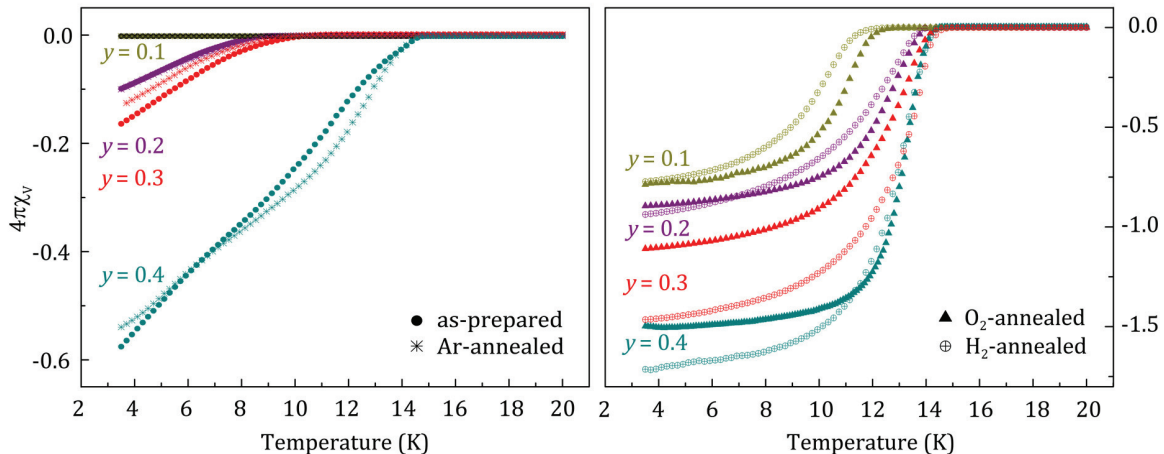


Figure 4.5 AC susceptibilities of as-prepared and Ar-annealed (left), O_2 - and H_2 -annealed (right) $\text{FeTe}_{1-y}\text{Se}_y$ ($x = 0.1, 0.2, 0.3, 0.4$).

Annealing as-prepared samples for 2 h at 300 °C under argon atmosphere does not influence the susceptibilities noteworthy (see asterisks Figure 4.5). Thus, the improved superconductivity is not caused by an annealing effect. Upon O₂-annealing all samples become bulk superconducting (see open circles Figure 4.5), even previously not superconducting FeTe_{0.9}Se_{0.1} ($T_c = 12.4$ K). Except for FeTe_{0.6}Se_{0.4}, where T_c remains at 14.4 K, FeTe_{0.8}Se_{0.2} and FeTe_{0.7}Se_{0.3} show increased critical temperatures (8.8 to 13.8 K and 9.7 to 14.3 K, respectively). By re-annealing O₂-annealed samples with hydrogen (2 h, 200 °C) T_{cs} remained constant while deviations were found merely concerning volume fractions, which are only roughly comparable (crossed circles Figure 4.5). Since the superconducting volume fraction is influenced by many different, hardly controllable factors such as grain boundary effects, particle size or powder density this value provides only a rough estimation and cannot be used as reliable parameter in order to observe actual changes by annealing.

Contrary to as-prepared FeTe_{1-y}Se_y samples all as-prepared Fe_{1.1}Te_{1-y}Se_y samples did not show superconducting properties. However, by O₂-annealing bulk superconductivity could be induced, too (Figure 4.6). With increasing Se content T_c increases from 12.5, 13.5 to 14.0 K, respectively.

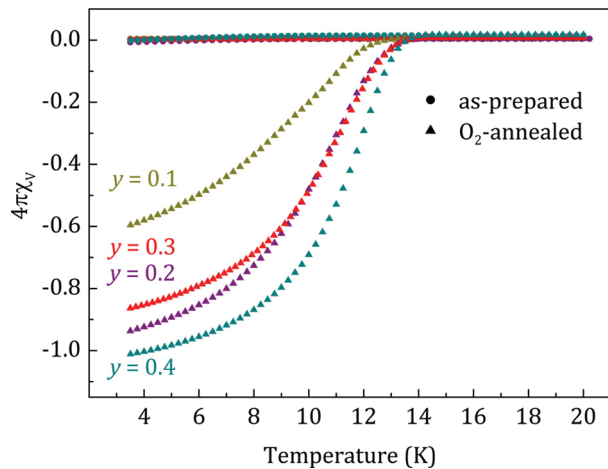


Figure 4.6 AC susceptibility measurements of as-prepared and O₂-annealed Fe_{1.1}Te_{1-y}Se_y.

The isothermal magnetization of as-prepared FeTe_{0.8}Se_{0.2} at 300 K shows solely paramagnetic behavior (black curve Figure 4.7 top left), whereas the curves of the O₂- and H₂-annealed samples feature a small fractions of some ferromagnetic impurity indicated by the s-shape of the curves with no saturation even at 50000 Oe and very

small values of $\sim 0.04 \mu/\mu_B$ (blue and green curves Figure 4.7 top left). At 1.8 K the as-prepared sample shows only a very small hysteresis without saturation at high fields (black curve Figure 4.7 top right), whereas for annealed $\text{FeTe}_{0.8}\text{Se}_{0.2}$ a typical ferromagnetic hysteresis superimposed by the magnetization of type II superconductors is found.^[83] The magnetic moment of annealed samples at 1.8 K remains constantly small with $\sim 0.05 \mu/\mu_B$ further indicating just a small magnetic impurity which is already ordered at 300 K (blue and green curves Figure 4.7 top right). This is consistent with the assumption that some ferrimagnetic iron oxide Fe_3O_4 ($T_C = 858 \text{ K}$, $\mu = 4.1 \mu_B$) or $\gamma\text{-Fe}_2\text{O}_3$ ($T_C = 948 \text{ K}$, $\mu = 2.5 \mu_B$) is formed through O_2 -annealing.^[84] Thus, already low quantities can easily be detected by magnetic measurements, contrary to XRPD. Extrapolated from the linear region (at high fields) of the isothermal magnetization at 300 K, the amounts of the magnetic impurity were estimated to be approximately 0.8 % Fe_2O_3 or 0.5 % Fe_3O_4 in O_2 -annealed $\text{FeTe}_{0.8}\text{Se}_{0.2}$.

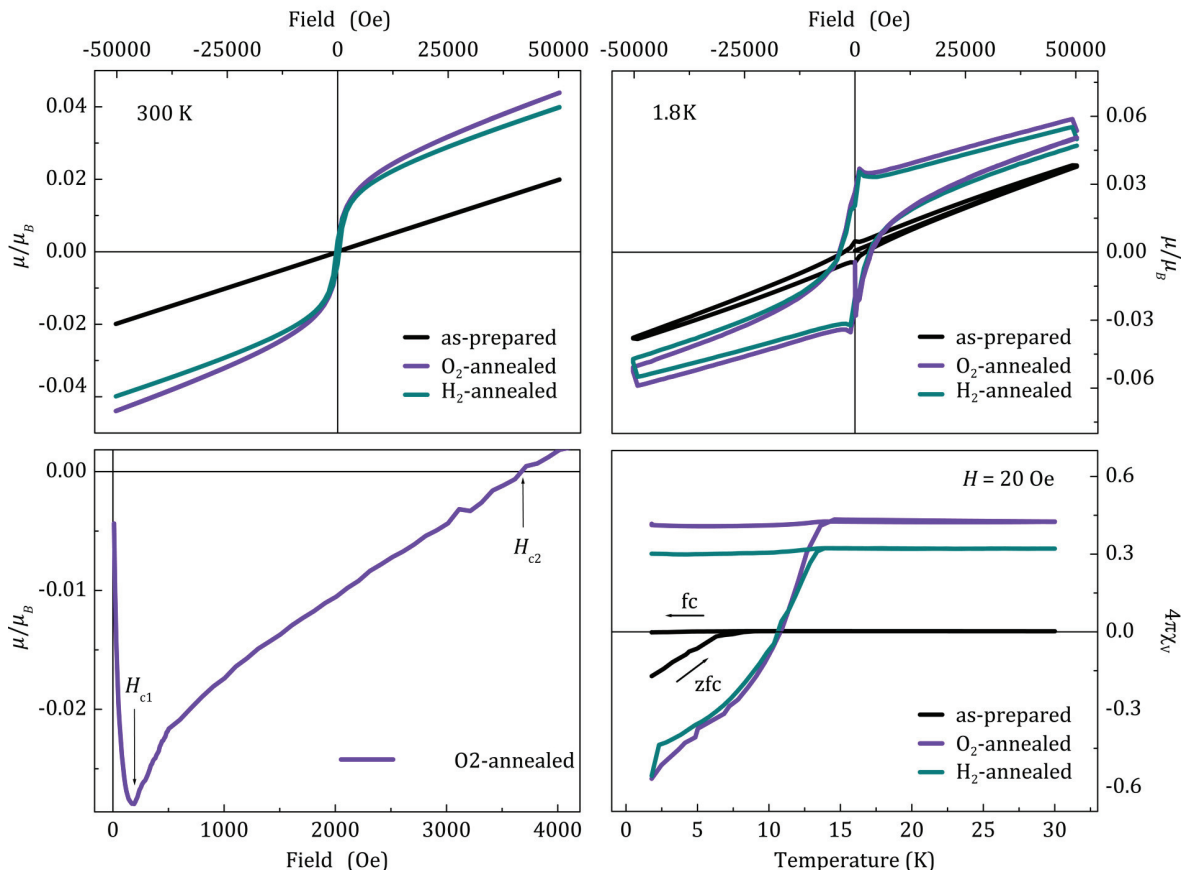


Figure 4.7 Top left: Isothermal magnetization for as-prepared, O_2 - and H_2 -annealed $\text{FeTe}_{0.8}\text{Se}_{0.2}$ at 300 K. Top right: At 1.8 K. Bottom left: Initial curve of the isothermal magnetization of O_2 -annealed $\text{FeTe}_{0.8}\text{Se}_{0.2}$. Bottom right: Zfc-fc measurements.

Such small quantities are certainly undetectable by XRPD, which strongly supports the idea that O₂-annealing extracts iron from the Fe_{1+x}Te_{1-y}Se_y compounds and forms iron oxides that probably reside at the surface of the particles. The characteristic initial curves for type II superconductors are shown in Figure 4.7 bottom, left. The magnetic susceptibility in Figure 4.7 (bottom right) shows weak superconductivity for as-prepared FeTe_{0.8}Se_{0.2}, with a T_c of 8 K (~20%). The annealed samples exhibit bulk superconductivity ($T_c = 14$ K, ~100 % shielding). As indicated by AC susceptibility, O₂-annealing increases T_c and the superconducting volume fraction, while subsequent H₂-annealing influences the magnetic susceptibility only slightly. After annealing, the magnetic susceptibility is shifted to higher values (temperature independent). This further proves a ferro- or ferrimagnetically ordered impurity absent prior to O₂-annealing.

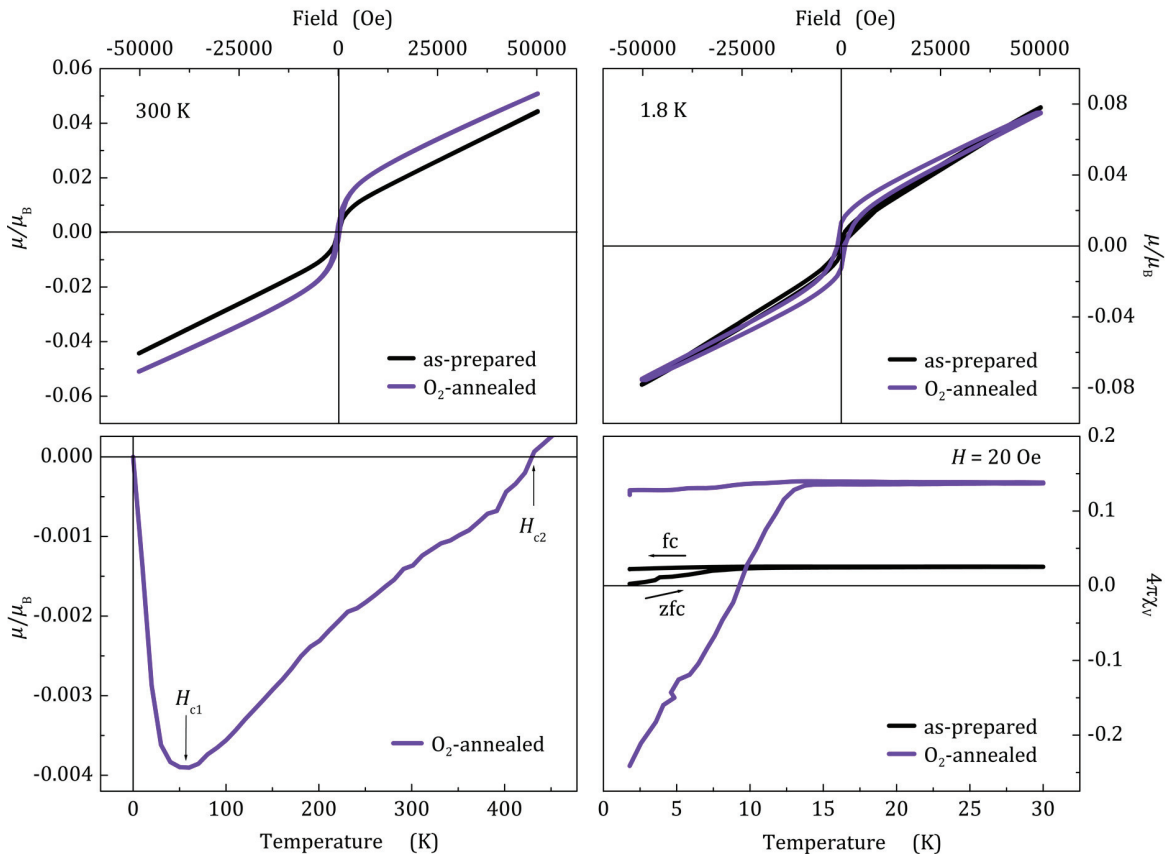


Figure 4.8 Top left: Isothermal magnetization for as-prepared and O₂-annealed Fe_{1.1}Te_{0.8}Se_{0.2} at 300 K. Top right: At 1.8 K. Bottom left: Initial curve of the isothermal magnetization of O₂-annealed Fe_{1.1}Te_{0.8}Se_{0.2}. Bottom right: Zfc-fc measurements.

For as-prepared Fe_{1.1}Te_{0.8}Se_{0.2}, the isothermal magnetization curve at 300 K (cf Figure 4.8 top left) already exhibits a small discontinuity. This indicates a magnetic impurity

already present prior to annealing, which is further increased after O_2 -annealing. The impurity in the as-prepared sample likely is some elemental Fe due to the 10% excess iron used, as indicated by EDX. The increase after O_2 -annealing originates again from iron oxide formation. The isothermal magnetization curves at 1.8 K both show less distinctive hystereses compared to $\text{FeTe}_{0.8}\text{Se}_{0.2}$. Figure 4.8 (bottom right) compares the magnetic susceptibilities under zfc and fc conditions. As-prepared $\text{Fe}_{1.1}\text{Te}_{0.8}\text{Se}_{0.2}$ shows only filamentary superconductivity interfered with the magnetic contribution of the assumed Fe impurity. As found in $\text{FeTe}_{0.8}\text{Se}_{0.2}$, the magnetic contribution significantly increases after O_2 -annealing while bulk superconductivity ($T_c = 14$ K) emerges. The weak superconducting properties of $\text{Fe}_{1.1}\text{Te}_{0.8}\text{Se}_{0.2}$ compared to $\text{FeTe}_{0.8}\text{Se}_{0.2}$ are presumably attributed to the higher amount of interstitial iron even after O_2 -annealing. The magnetic measurements of $\text{FeTe}_{0.8}\text{Se}_{0.2}$ and $\text{Fe}_{1.1}\text{Te}_{0.8}\text{Se}_{0.2}$ clearly demonstrate the important role of interstitial iron for the superconducting properties and further prove the emergence of a magnetic impurity (iron oxide) upon annealing.

4.5 Electrical resistivity

The electrical resistivities for as-prepared $\text{FeTe}_{1-y}\text{Se}_y$ samples (Figure 4.9, black curves top and middle) show zero resistivity with $x \geq 0.2$. For $\text{FeTe}_{0.9}\text{Se}_{0.1}$ only a steep drop at T_c is visible. Before reaching T_c the samples exhibit nonmetallic behavior. A logarithmic temperature dependence below ~ 100 K indicate a weak localization of the charge-carriers which could be attributed to interstitial Fe.^[85]

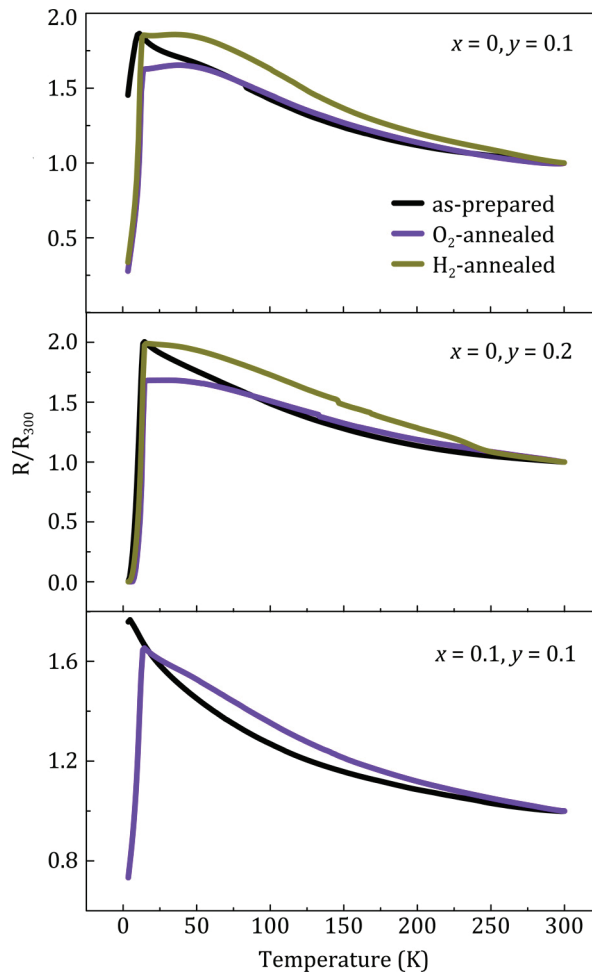


Figure 4.9 Relative electrical resistivities for as-prepared, O_2 - and H_2 -annealed $\text{Fe}_{1+x}\text{Te}_{1-y}\text{Se}_y$.

This effect is weakened by O_2 -annealing for a temperature range around 50 K. Distinctive metallic behavior, which is normally found in single crystals after O_2 -annealing^[81] was not observed. After H_2 -annealing the signature of the relative resistivity curves is preserved but exactly reaches the maximum value of the as-prepared samples at T_c indicating some effect due to hydrogen-annealing. On the contrary, $\text{Fe}_{1.1}\text{Te}_{0.8}\text{Se}_{0.2}$ is only superconducting after O_2 -treatment (Figure 4.9, bottom).

4.6 Conclusion

$\text{Fe}_{1+x}\text{Te}_{1-y}\text{Se}_y$ ($x = 0\text{-}0.1, y = 0.1\text{-}0.4$) with different nominal amounts of interstitial iron were O_2 - and subsequently H_2 -annealed and analyzed according to their structural, magnetic and electrical properties. Effects merely due to heating could be excluded by control experiments performed under Ar-atmosphere.

The superconducting properties of $\text{FeTe}_{1-y}\text{Se}_y$ depend on Se concentration and the amount of interstitial Fe. After O_2 -annealing bulk superconductivity can be induced in all samples. The process was not found reversible by hydrogen-annealing.

Thus, oxygen annealing at 300 °C improves the superconducting properties of polycrystalline $\text{Fe}_{1+x}\text{Te}_{1-y}\text{Se}_y$ by irreversible oxidative de-intercalation of interstitial iron atoms, whereby traces of magnetic iron oxides are formed. The heterogeneous process starts at the surface and likely causes inhomogeneous particles along with FeTe_2 impurity formation. Thus the *anti-PbO*-type phase obviously rather degrades when iron is extracted from within the layers, in contrast to the formation of iron-deficient layers like in $\text{K}_{1-x}\text{Fe}_{2-y}\text{Se}_2$ ^[86, 87] (Chapter 5) or $\text{Na}_{1-x}\text{Fe}_{2-y}\text{As}_2$ (Chapter 7).^[10]

4.7 Appendix

Table 4.2 Crystallographic details of as-prepared, O_2 - and H_2 -annealed $\text{FeTe}_{0.9}\text{Se}_{0.1}$.

Empirical formula	$\text{FeTe}_{0.9}\text{Se}_{0.1}$		
Diffractometer	Stoe Stadi P Mo $K_{\alpha 1}$ $\lambda = 0.71073 \text{ \AA}$, capillary 0.3 mm		
Space group	$P4/nmm$ oc 2 ($Z = 2$)		
	as-prepared	O_2 - annealed	H_2 - annealed
Refined comp.*	$\text{Fe}_{1.05(1)}\text{Te}_{0.91(1)}\text{Se}_{0.09(1)}$	$\text{Fe}_{1.03(1)}\text{Te}_{0.91(1)}\text{Se}_{0.09(1)}$	$\text{Fe}_{1.04(2)}\text{Te}_{0.91(1)}\text{Se}_{0.09(1)}$
Weight percent	94.2(1)	91.6(2)	92.6(1)
Lattice parameters (pm)	$a = 381.91(2)$ $c = 624.77(5)$	$a = 382.00(2)$ $c = 625.07(4)$	$a = 381.32(2)$ $c = 624.75(8)$
Cell volume (nm ³)	0.09113(1)	0.09121(1)	0.09084(2)
Atomic parameters			
Fe1	$2b (\frac{3}{4}, \frac{1}{4}, 0)$		
Fe2	$2c (\frac{1}{4}, \frac{1}{4}, z)$ $z = 0.711(3)$	$z = 0.69(1)$	$z = 0.710(4)$
Te	$2c (\frac{1}{4}, \frac{1}{4}, z)$ $z = 0.281(1)$	$z = 0.281(1)$	$z = 0.281(1)$
Se	$2c (\frac{1}{4}, \frac{1}{4}, z)$ $z = 0.239(4)$	$z = 0.227(8)$	$z = 0.233(5)$
Atomic displacement parameters			
$U_{\text{iso}} (\text{\AA}^2)$ Fe1 / Fe2	0.011(1)	0.015 (1)	0.015(1)
$U_{\text{iso}} (\text{\AA}^2)$ Te / Se	0.012(1)	0.017(1)	0.015(1)
Atomic distances and angles			
Fe1-Se	2.43(1)	2.38(3)	2.39(2)
Fe1-Te	2.60(1)	2.59(1)	2.59(1)
Fe ¹ -Fe ²	2.63(1)	2.70(1)	2.63(2)
Fe ¹ -Fe ¹	2.70(1)	2.70(1)	2.70(1)
Se-Fe-Se	103.9(9) 112.3(5)	106.8(2) 110.8(9)	105.3(1) 111.6(6)
Se-Fe-Te	99.3(5) 114.7(3)	100.8(9) 113.8(5)	100.0(6) 114.3(3)
Te-Fe-Te	94.7(1) 117.3(1)	94.8(1) 117.3(1)	94.7(1) 117.3(1)
R_p / R_{wp}	2.247 / 2.955	3.678 / 5.122	2.149 / 2.884
$R_{\text{Bragg}} / \chi^2$	0.438 / 2.116	0.616 / 2.384	0.384 / 2.145

*Iron quantities consist of fully occupied (occ = 1.0) Fe1 and partly occupied Fe2 (occ = 0.02-0.12).

Table 4.3 Crystallographic details of as-prepared, O₂- and H₂-annealed FeTe_{0.8}Se_{0.2}.

Empirical formula	FeTe _{0.8} Se _{0.2}	as-prepared	O ₂ - annealed	H ₂ - annealed
Refined comp.*	$\text{Fe}_{1.05(1)}\text{Te}_{0.82(1)}\text{Se}_{0.18(1)}$	$\text{Fe}_{1.04(1)}\text{Te}_{0.86(1)}\text{Se}_{0.14(1)}$	$\text{Fe}_{1.04(1)}\text{Te}_{0.87(1)}\text{Se}_{0.13(1)}$	
Weight percent	94.2(1)	90.6(2)	91.8(1)	
Lattice parameters (pm)	$a = 380.76(3)$ $c = 619.14(8)$	$a = 380.90(3)$ $c = 619.2(1)$	$a = 380.97(3)$ $c = 618.98(8)$	
Cell volume (nm ³)	0.08976(2)	0.08984(2)	0.08984(2)	
Atomic parameters				
Fe1	$2b (3/4, 1/4, 0)$			
Fe2	$2c (1/4, 1/4, z)$	$z = 0.704(3)$	$z = 0.721(5)$	$z = 0.700(5)$
Te	$2c (1/4, 1/4, z)$	$z = 0.282(1)$	$z = 0.282(1)$	$z = 0.281(1)$
Se	$2c (1/4, 1/4, z)$	$z = 0.254(4)$	$z = 0.239(4)$	$z = 0.251(5)$
Atomic displacement parameters				
$U_{\text{iso}} (\text{\AA}^2)$ Fe1 / Fe2	0.011(1)	0.008(1)	0.007(1)	
$U_{\text{iso}} (\text{\AA}^2)$ Te / Se	0.013(1)	0.012(1)	0.010(1)	
$R_{\text{P}} / R_{\text{WP}}$	2.657 / 3.586	2.589 / 3.501	2.842 / 3.714	
$R_{\text{Bragg}} / \chi^2$	0.453 / 2.837	0.557 / 2.341	0.774 / 2.226	

*Iron quantities consist of fully occupied (occ = 1.0) Fe1 and partly occupied Fe2 (occ = 0.02-0.12).

Table 4.4 Crystallographic details of as-prepared, O₂- and H₂-annealed FeTe_{0.7}Se_{0.3}.

Empirical formula	FeTe _{0.7} Se _{0.3}	as-prepared	O ₂ - annealed	H ₂ - annealed
Refined comp.*	$\text{Fe}_{1.04(1)}\text{Te}_{0.75(1)}\text{Se}_{0.25(1)}$	$\text{Fe}_{1.02(1)}\text{Te}_{0.74(2)}\text{Se}_{0.26(2)}$	$\text{Fe}_{1.05(1)}\text{Te}_{0.78(4)}\text{Se}_{0.22(4)}$	
Weight percent	95.6(1)	88.4(3)	89.1(5)	
Lattice parameters (pm)	$a = 380.54(9)$ $c = 613.58(8)$	$a = 381.10(3)$ $c = 613.55(6)$	$a = 381.35(4)$ $c = 613.63(9)$	
Cell volume (nm ³)	0.08885(4)	0.08911(2)	0.08924(3)	
Atomic parameters				
Fe1	$2b (3/4, 1/4, 0)$			
Fe2	$2c (1/4, 1/4, z)$	$z = 0.715(7)$	$z = 0.68(2)$	$z = 0.70(1)$
Te	$2c (1/4, 1/4, z)$	$z = 0.283(1)$	$z = 0.280(1)$	$z = 0.283(1)$
Se	$2c (1/4, 1/4, z)$	$z = 0.244(3)$	$z = 0.260(7)$	$z = 0.229(8)$
Atomic displacement parameters				
$U_{\text{iso}} (\text{\AA}^2)$ Fe1 / Fe2	0.010(1)	0.013(1)	0.017(1)	
$U_{\text{iso}} (\text{\AA}^2)$ Te / Se	0.013(1)	0.017(1)	0.019(1)	
$R_{\text{P}} / R_{\text{WP}}$	2.530 / 3.800	3.743 / 5.305	5.790 / 9.086	
$R_{\text{Bragg}} / \chi^2$	0.582 / 3.083	1.320 / 3.365	1.901 / 5.112	

*Iron quantities consist of fully occupied (occ = 1.0) Fe1 and partly occupied Fe2 (occ = 0.02-0.12).

Table 4.5 Crystallographic details of as-prepared, O_2 - and H_2 -annealed $\text{FeTe}_{0.6}\text{Se}_{0.4}$.

Empirical formula	$\text{FeTe}_{0.6}\text{Se}_{0.4}$	as-prepared	O_2 - annealed	H_2 - annealed
Refined comp.*	$\text{Fe}_{1.03(1)}\text{Te}_{0.67(1)}\text{Se}_{0.33(1)}$		$\text{Fe}_{1.02(1)}\text{Te}_{0.65(1)}\text{Se}_{0.35(1)}$	$\text{Fe}_{1.07(1)}\text{Te}_{0.65(4)}\text{Se}_{0.35(4)}$
Weight percent	97.2(1)		91.9(3)	91(1)
Lattice parameters (pm)	$a = 380.61(3)$ $c = 608.17(5)$		$a = 380.57(3)$ $c = 607.61(5)$	$a = 380.89(4)$ $c = 608.0(1)$
Cell volume (nm ³)	0.08810(1)		0.08800(1)	0.08821(2)
Atomic parameters				
Fe1	$2b (3/4, 1/4, 0)$			
Fe2	$2c (1/4, 1/4, z)$	$z = 0.71(1)$	$z = 0.68(1)$	$z = 0.74(1)$
Te	$2c (1/4, 1/4, z)$	$z = 0.286(1)$	$z = 0.285(1)$	$z = 0.287(1)$
Se	$2c (1/4, 1/4, z)$	$z = 0.245(2)$	$z = 0.249(3)$	$z = 0.242(5)$
Atomic displacement parameters				
$U_{\text{iso}} (\text{\AA}^2)$ Fe1 / Fe2	0.010(1)		0.004(1)	0.020(1)
$U_{\text{iso}} (\text{\AA}^2)$ Te / Se	0.014(1)		0.009(1)	0.022(1)
$R_{\text{P}} / R_{\text{WP}}$	2.309 / 3.374		2.791 / 3.838	4.504 / 7.169
$R_{\text{Bragg}} / \chi^2$	0.366 / 2.642		0.557 / 1.847	1.160 / 4.480

*Iron quantities consist of fully occupied (occ = 1.0) Fe1 and partly occupied Fe2 (occ = 0.02-0.12).

Table 4.6 Crystallographic details of as-prepared and O_2 -annealed $\text{Fe}_{1.1}\text{Te}_{0.9}\text{Se}_{0.1}$.

Empirical formula	$\text{Fe}_{1.1}\text{Te}_{0.9}\text{Se}_{0.1}$	as-prepared	O_2 - annealed
Refined comp.*	$\text{Fe}_{1.098(5)}\text{Te}_{0.97(1)}\text{Se}_{0.03(1)}$		$\text{Fe}_{1.099(4)}\text{Te}_{0.96(1)}\text{Se}_{0.04(1)}$
Weight percent	100		95.8(2)
Lattice parameters (pm)	$a = 382.00(4)$ $c = 625.80(6)$		$a = 381.78(3)$ $c = 625.48(6)$
Cell volume (nm ³)	0.09132(2)		0.09117(2)
Atomic parameters			
Fe1	$2b (3/4, 1/4, 0)$		
Fe2	$2c (1/4, 1/4, z)$	$z = 0.700(4)$	$z = 0.716(3)$
Te	$2c (1/4, 1/4, z)$	$z = 0.2827(4)$	$z = 0.282(1)$
Se	$2c (1/4, 1/4, z)$	$z = 0.245$ (fixed)	$z = 0.245$ (fixed)
Atomic displacement parameters			
$U_{\text{iso}} (\text{\AA}^2)$ Fe1 / Fe2	0.023(1)		0.021(1)
$U_{\text{iso}} (\text{\AA}^2)$ Te / Se	0.025(1)		0.027(1)
$R_{\text{P}} / R_{\text{WP}}$	6.861 / 9.565		4.064 / 6.159
$R_{\text{Bragg}} / \chi^2$	3.202 / 2.968		1.256 / 2.302

*Iron quantities consist of fully occupied (occ = 1.0) Fe1 and partly occupied Fe2 (occ = 0.02-0.12).

Table 4.7 Crystallographic details of as-prepared and O_2 -annealed $\text{Fe}_{1.1}\text{Te}_{0.8}\text{Se}_{0.2}$.

Empirical formula	$\text{Fe}_{1.1}\text{Te}_{0.8}\text{Se}_{0.2}$	
	as-prepared	O_2 - annealed
Refined comp.*	$\text{Fe}_{1.117(4)}\text{Te}_{0.89(2)}\text{Se}_{0.11(2)}$	$\text{Fe}_{1.109(3)}\text{Te}_{0.81(1)}\text{Se}_{0.19(1)}$
Weight percent	100	98.9(2)
Lattice parameters (pm)	$a = 381.81(4)$ $c = 621.64(7)$	$a = 381.48(4)$ $c = 621.12(7)$
Cell volume (nm ³)	0.09062(2)	0.09039(2)
Atomic parameters		
Fe1	$2b (\frac{3}{4}, \frac{1}{4}, 0)$	
Fe2	$2c (\frac{1}{4}, \frac{1}{4}, z)$	$z = 0.709(3)$
Te	$2c (\frac{1}{4}, \frac{1}{4}, z)$	$z = 0.284(1)$
Se	$2c (\frac{1}{4}, \frac{1}{4}, z)$	$z = 0.26(2)$
Atomic displacement parameters		
U_{iso} (Å ²) Fe1 / Fe2	0.021(1)	0.026(1)
U_{iso} (Å ²) Te / Se	0.028(1)	0.028/(1)
R_P / R_{wp}	5.449 / 7.861	3.450 / 4.997
R_{Bragg} / χ^2	2.650 / 2.376	1.072 / 1.937

*Iron quantities consist of fully occupied (occ = 1.0) Fe1 and partly occupied Fe2 (occ = 0.02-0.12).

Table 4.8 Crystallographic details of as-prepared and O_2 -annealed $\text{Fe}_{1.1}\text{Te}_{0.7}\text{Se}_{0.3}$.

Empirical formula	$\text{Fe}_{1.1}\text{Te}_{0.7}\text{Se}_{0.3}$	
	as-prepared	O_2 - annealed
Refined comp.*	$\text{Fe}_{1.085(4)}\text{Te}_{0.79(1)}\text{Se}_{0.21(1)}$	$\text{Fe}_{1.096(4)}\text{Te}_{0.73(1)}\text{Se}_{0.27(1)}$
Weight percent	100	100
Lattice parameters (pm)	$a = 381.03(6)$ $c = 614.20(4)$	$a = 381.06(6)$ $c = 614.48(8)$
Cell volume (nm ³)	0.08917(3)	0.08923(3)
Atomic parameters		
Fe1	$2b (\frac{3}{4}, \frac{1}{4}, 0)$	
Fe2	$2c (\frac{1}{4}, \frac{1}{4}, z)$	$z = 0.717(3)$
Te	$2c (\frac{1}{4}, \frac{1}{4}, z)$	$z = 0.2863(4)$
Se	$2c (\frac{1}{4}, \frac{1}{4}, z)$	$z = 0.239(4)$
Atomic displacement parameters		
U_{iso} (Å ²) Fe1 / Fe2	0.015(1)	0.022(1)
U_{iso} (Å ²) Te / Se	0.022(1)	0.027(1)
R_P / R_{wp}	3.488 / 4.905	3.251 / 4.932
R_{Bragg} / χ^2	0.631 / 1.358	0.782 / 1.532

*Iron quantities consist of fully occupied (occ = 1.0) Fe1 and partly occupied Fe2 (occ = 0.02-0.12).

Table 4.9 Crystallographic details of as-prepared and O₂-annealed Fe_{1.1}Te_{0.6}Se_{0.4}.

Empirical formula	Fe _{1.1} Te _{0.6} Se _{0.4}	
	as-prepared	O ₂ - annealed
Refined comp.*	Fe _{1.080(3)} Te _{0.64(2)} Se _{0.36(2)}	Fe _{1.107(3)} Te _{0.60(2)} Se _{0.40(2)}
Weight percent	100	100
Lattice parameters (pm)	a = 380.38(8) c = 606.4(1)	a = 380.62(3) c = 606.55(7)
Cell volume (nm ³)	0.08774(4)	0.08787(2)
Atomic parameters		
Fe1	2b (3/4, 1/4, 0)	
Fe2	2c (1/4, 1/4, z)	z = 0.684(4)
Te	2c (1/4, 1/4, z)	z = 0.288(1)
Se	2c (1/4, 1/4, z)	z = 0.258(3)
Atomic displacement parameters		
U_{iso} (Å ²) Fe1 / Fe2	0.022(1)	0.030(1)
U_{iso} (Å ²) Te / Se	0.029(1)	0.033(1)
$R_{\text{P}} / R_{\text{wP}}$	3.239 / 5.225	4.120 / 6.273
$R_{\text{Bragg}} / \chi^2$	1.540 / 2.353	1.928 / 3.289

*Iron quantities consist of fully occupied (occ = 1.0) Fe1 and partly occupied Fe2 (occ = 0.02-0.12).

5 $K_{1-x}Fe_{2-y}Se_2$ via reductive intercalation

5.1 Introduction

11-type compounds like FeSe and $FeTe_{1-y}Se_y$ represent excellent host materials for intercalation reactions since their charge neutral $FeCh_{4/4}$ layers stick together only by weak van der Waals interactions. Several recent studies revealed a large enhancement of T_c up to 45 K upon intercalation of several spacer layers into *anti-PbO*-type $FeCh$ under mild conditions.^[38, 88, 89] A common approach is the intercalation of alkaline and alkaline earth metals in liquid ammonia in order to obtain 122-type $A/AeFe_2Se_2$ phases.^[90] Hereby a co-intercalation of NH_3 and/or ANH_2 occurs.^[88] Beside these soft chemistry approaches, ternary iron selenides are commonly synthesized by solid state reactions. Especially the K-Fe-Se system has been investigated thoroughly.

KFe_2Se_2 (122-type) was found to be superconductive below 32 K.^[91] Electron counting in stoichiometric composition leads to a strongly electron overdoped system with $\sim 0.5e^-/Fe$ (corresponding to $Fe^{+1.5}$) assuming K^{+1} and Se^{-2} . These high "doping" levels strongly affect the electronic structure of the material, leading to characteristics differing from those of other iron-based superconductors. Therefore, ternary iron selenides lead to conflicts with the commonly accepted picture of the emergence of high temperature superconductivity in Fe-based materials.

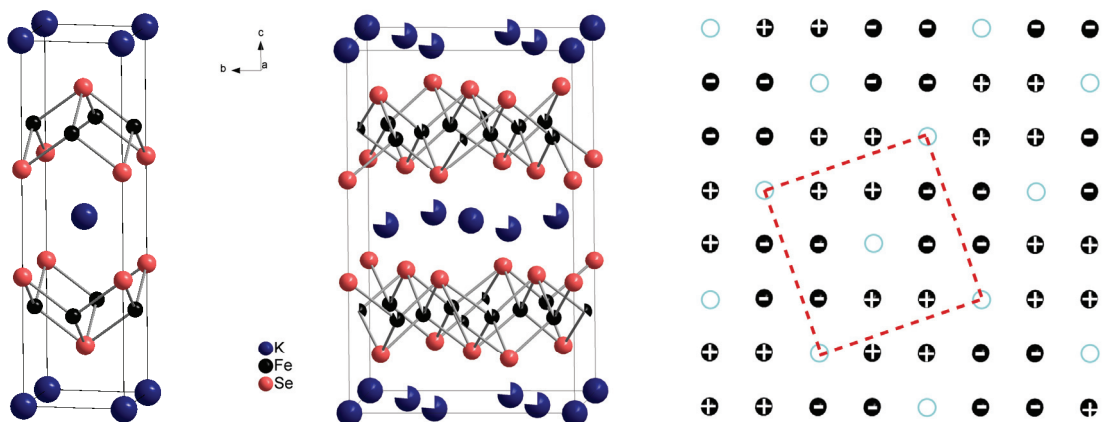


Figure 5.1 Left: 122-type crystal structure. Middle: 245-type $K_{1-x}Fe_{1.6}Se_2$ ($x = 0.2$). Right: Fe vacancy ordering in 245-type $K_{1-x}Fe_{1.6}Se_2$ ($x = 0.2$). Black spheres are Fe ions, blue circles represent Fe vacancies. + and - show the spin alignment.

A closer look revealed more complex structure properties with vacancies on the K, as well as on the Fe iron site ($K_{1-x}Fe_{2-y}Se_2$) and phase separation occurred. In the K-Fe-Se system several different phases such as $K_{1-x}Fe_2Se_2$, $K_2Fe_3Se_4$, $K_2Fe_7Se_8$, $K_3Fe_4Se_6$ and $K_2Fe_4Se_5$ with deviating physical properties exist.^[92-95] They often exhibit charge or Fe vacancy ordering and the electronic properties range from superconducting to insulating along with antiferromagnetic (AFM) ordering. $K_2Fe_4Se_5$ (also stated as $K_{0.8}Fe_{1.6}Se_2$ or 245-phase) exhibits a $\sqrt{5} \times \sqrt{5}$ Fe vacancy order as depicted in Figure 5.1. The stoichiometric phase is an AFM semiconductor ($\mu_B \sim 3$), in which 4 spins align parallel in tetramers leading to an overall chess like AFM spin alignment^[95] (cf. Figure 5.1, right). Superconductivity within such samples presumably occurs by phase separation and $K_{1-x}Fe_2Se_2$ is preferentially considered to be the superconducting phase.^[92] However, determining the superconducting and parent phase and how superconductivity is induced are still current issues in this system. Recent investigations suggest $K_2Fe_4Se_5$ to be the magnetic, Mott insulating parent compound, in which superconductivity can be induced by high temperature annealing. Thus, an Fe vacancy order to disorder transition becomes reasonable as origin of superconductivity.^[94]

A perfect $\sqrt{5} \times \sqrt{5}$ Fe vacancy order is only found for $K_{0.8}Fe_{1.6}Se_2$ (or $K_2Fe_4Se_5$). Here the Fe 4d site is empty while the 16i site is fully occupied. With increasing deviation from this stoichiometry and due to disorder the 4d site becomes more occupied. This results in a similar occupation of both sites in a deficient 122-type structure, space group $I4/mmm$ with a random Fe vacancy distribution. Thus, the quotient between the 4d and 16i site is indicative for the degree of disorder in the $\sqrt{5} \times \sqrt{5}$ Fe vacancy order.^[95]

Conventional solid state synthesis unavoidably produces phase separated samples. Therefore the identification of the true superconducting phase is very difficult.

An alternative synthesis strategy to $K_{1-x}Fe_{2-y}Se_2$ under mild conditions offers the opportunity to potentially obtain single phase samples. A promising approach could be the solvent-based reductive intercalation of K between the layers of *anti-PbO*-type FeSe under inert conditions. Beside the aforementioned liquid NH₃, several organic compounds are capable of solving K in polar-aprotic solvents like THF for enabling intercalation.

5.2 Synthesis

$K_xFe_{2-y}Se_2$ was obtained from FeSe and K by a solvent-based reductive intercalation under mild conditions in dry THF under Schlenk conditions. FeSe was synthesized by heating the elements to 700 °C for 24 h, cooling to 330 °C (40 h) and quenching to -10 °C. Potassium was solved in THF with the assistance of different organic molecules as electron acceptors. Biphenyl, naphthalene, benzophenone, crown ethers (15-crown-5, 18-crown-6) and TEMPO (2,2,6,6-Tetramethyl-piperidin-1-yl)oxyl) were used with equimolar amounts of K, except for 15-crown-5. In this case, twice the amount of crown ether is necessary. Some formal potentials E°' versus the ferrocene/ferrocenium couple, as recommended by IUPAC,^[96, 97] are listed in Table 5.1. While naphthalenide with -3.10 V exhibits a rather strong reduction potential, for example the benzophenone ketyl radical (-2.30 V) is a milder reducing agent than Li or K in NH₃. Thus, the investigated systems reveal a reduction potential range similar to A/NH₃ in which successful intercalation already has been observed. TEMPONa has been used in organic synthesis as mild organic single-electron transfer (SET) reagent.^[98] This result was adapted to form TEMPOK, respectively.

Reactions were carried out in a one or two step synthesis. Different temperatures, concentrations and molar ratios were analyzed. With less than 0.5 eq K, no full conversion to $K_xFe_{2-y}Se_2$ was achieved initially. For this reason 0.5 - 1.0 eq K were primarily used. Best results were obtained with concentrations of $\sim 0.10 \pm 0.05$ mol/L and reaction times of 4-10 days. Naphthalene, biphenyl, benzophenone or TEMPO can react in a one step synthesis at room temperature.

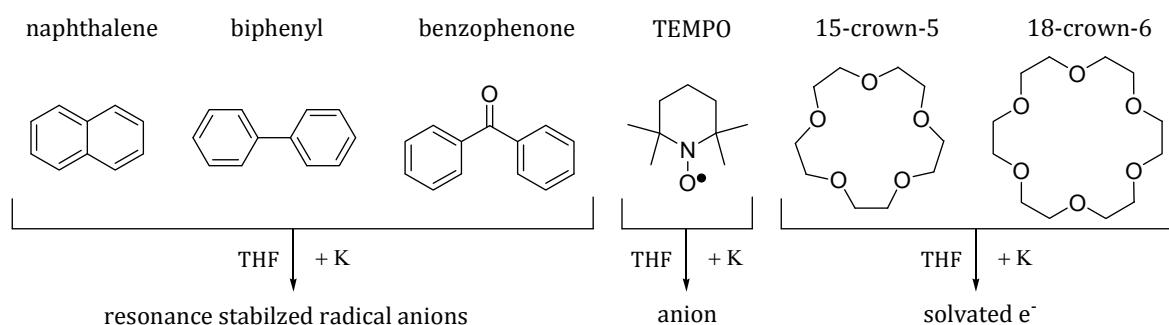


Figure 5.2 Organic compounds used for solvation of K in THF with their respective reactive species upon K addition.

Table 5.1 Formal potentials $E^{\circ'}$ (V vs ferrocene) of selected reducing agents from ref. [96]

reductant	solvent	$E^{\circ'}$
$[C_{10}H_8]^-$	THF	-3.10
Li	NH ₃	-2.64
K	NH ₃	-2.38
[anthracene] ⁻	glyme	-2.47
[benzophenone] ⁻	THF	-2.30
Na	NH ₃	-2.25
[acenaphthalene] ⁻	THF	-2.26
$[FeCp_2]$	-	0.0

In a two step synthesis, the reactive K-organic system was allowed to form in THF in the first step. The solution was subsequently cooled to the required temperature (>-78 °C) followed by the addition of FeSe. Potassium/crown ether solutions are merely stable for a short period of time (10-30 min) at room temperature. Therefore, potassium was initially melted to obtain a higher surface, allowing a more rapid solvation. THF and crown ether were added, followed by ultrasonification for 5-10 min. The blue solution was cooled to -75 °C (EtOH/N₂ liq.) for 15 min and FeSe was added. The mixture was allowed to warm up to room temperature and was stirred for 4-10 days. The slurry was allowed to settle, washed twice with THF and dried *in vacuo*. $K_xFe_{2-y}Se_2$ was obtained as air sensitive, gray powder.

Annealing at 120-230 °C for 10-170 h was conducted to selected samples in alumina crucibles inside sealed ©Duran ampoules.

5.3 Crystal structure

Upon K intercalation in FeSe every second of the tetrahedral layers have to slide by 0.5 along lattice parameter b (origin choice 1) or by 0.25 0.25 0 (origin choice 2) in order to result in a 122-type compound. Refinements in $I4/mmm$ already gave reasonable fits. However, weak superstructure reflections indicated the vacancy ordered 245-type structure in space group $I4/m$.^[93, 94]

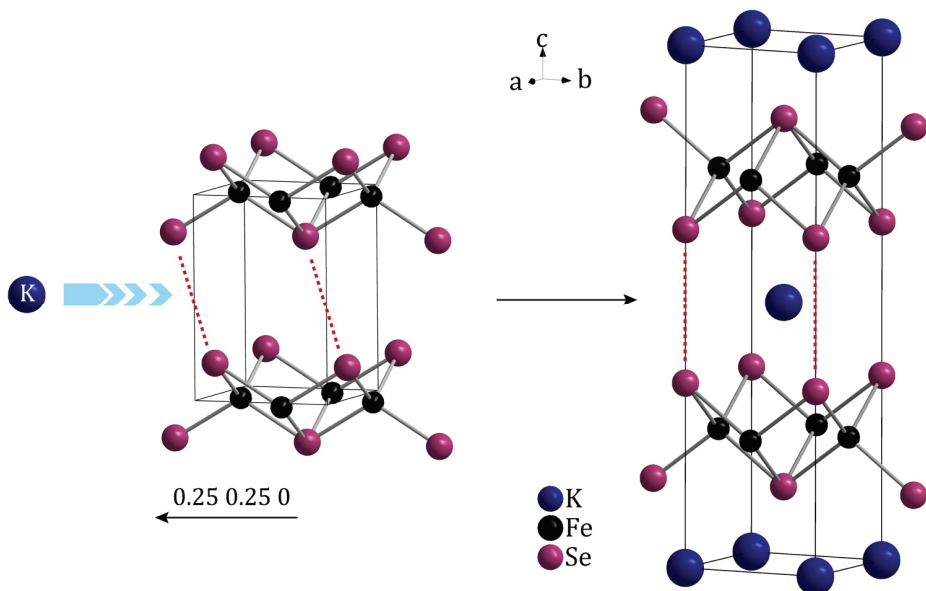


Figure 5.3 Structural relationship between FeSe (11-type) left and $K_{1-x}Fe_{2-y}Se_2$ (122-type, $x,y = 0$) upon K intercalation.

The main superstructure reflection ((110) , $6.6\ 2\theta$) was weak, but visible in all samples. Depending on the amounts and the organic species that were used, slightly different lattice parameters were found. Conditional to the synthesis conditions varying fractions of starting material and a small Fe impurity were detected. Using 0.4-0.5 eq K resulted in ~40-85 % conversion to $K_{1-x}Fe_{2-y}Se_2$. With e.g. 1.0 eq K/TEMPO and long reaction times (> 7 days) no starting material was visible in XRPD anymore, but small quantities of impurities, like iron, occurred (Figure 5.5). Iron may have arisen from the reductive conditions or as a consequence of charge compensation. If FeSe not readily accepts additional electrons (direct e^- doping), the system might evade by becoming Fe deficient, as confirmed by Rietveld refinements. In the space group $I4/mmm$ the Fe site is vacant by 18-35 % (Table 5.2). Comparing the occupancies of Fe1 ($4d$) and Fe2 ($16i$) sites reveal imperfect $\sqrt{5} \times \sqrt{5}$ vacancy ordering according to the literature.^[95] Quotients of $4d/16i$ occupancies range from 1-0.6 for as-prepared and down to 0.34 for annealed samples, significantly deviating from zero for perfect ordering. Thus the obtained phases are between the two extremes of perfect vacancy ordering ($I4/m$) and a random distribution of Fe vacancies ($I4/mmm$). Furthermore the occupancies are 0.6-1.0 for K and 0.65 - 0.82 for Fe. This prevents perfect $\sqrt{5} \times \sqrt{5}$ vacancy ordering (occ. K = 0.8, Fe = 0.8), too. Both effects contribute to the degree of disorder in the $\sqrt{5} \times \sqrt{5}$ Fe vacancy order.

Table 5.2 Crystallographic data for several $K_{1-x}Fe_{2-y}Se_2$ samples.

eq. K	1.0	1.0	0.5	1.0	0.4
System	15-crown-5	naphthalene*	biphenyl	TEMPO	biphenyl
Space group	<i>I</i> 4/ <i>mmm</i>	<i>I</i> 4/ <i>mmm</i>	<i>I</i> 4/ <i>mmm</i>	<i>I</i> 4/ <i>mmm</i>	<i>I</i> 4/ <i>mmm</i>
Lattice parameters (pm)	$a = 393.66(4)$ $c = 1394.5(4)$	$a = 393.4(1)$ $c = 1397.7(7)$	$a = 388.0(1)$ $c = 1421.2(7)$	$a = 394.19(3)$ $c = 1390.7(2)$	$a = 390.81(2)$ $c = 1408.1(2)$
Cell vol. (\AA^3)	216.10(8)	216.3(2)	213.9(2)	216.10(5)	215.05(3)
occupancies					
K	0.93(4)	0.85(5)	0.6(1)	1.00(2)	0.75(2)
Fe	0.65(4)	0.72(6)	0.8(1)	0.75(2)	0.82(2)
Se	1	1	1	1	1
Weight %	95	95	43	98	95

* Naphthalene was used catalytically (0.1 eq.)

Table 5.3 Comparison of crystallographic data in space group *I*4/*mmm* and *I*4/*m* of an annealed sample (170 h, 230 °C).

Formula	$K_{1-x}Fe_{2-y}Se_2$		$K_{1-x}Fe_{2-y}Se_2$	
eq. K	0.5		0.5	
System	biphenyl		biphenyl	
Space group	<i>I</i> 4/ <i>mmm</i>		<i>I</i> 4/ <i>m</i>	
Lattice parameters (pm)	$a = 390.66(2)$ $c = 1409.5(1)$		$a = 873.71(4)$ $c = 1409.6(1)$	
Cell volume (\AA^3)	215.11(3)		1076.0(2)	
atomic parameters	occ.		occ.	
K1 $2a (0\ 0\ 0)$	0.78(2)		0.8(1)	
K2 $8h (x\ y\ 0)$	-	-	0.83(5)	$x = 0.36(1), y = 0.19(1)$
Fe1 $4d (0\ \frac{1}{2}\ \frac{1}{4})$	0.81(2)		0.32(5)	
Fe2 $16i (x\ y\ z)$	-	-	0.93(2)	$x = 0.21(1), y = 0.10(1)$ $z = 0.25(1)$
Se1 $4e (\frac{1}{2}\ \frac{1}{2}\ z)$	1	$z = 0.3(1)$	1	$z = 0.14(1)$
Se2 $16i (x\ y\ z)$	-	-	1	$x = 0.10(1), y = 0.29(1)$, $z = 0.15(1)$
weight %	86 %		86%	
R_{wp} / R_p	1.674 / 1.183		1.620 / 1.158	
χ^2 / R_{Bragg}	1.953 / 0.169		1.890 / 0.241	

Table 5.2 summarizes the crystallographic data for $K_{1-x}Fe_{2-y}Se_2$ obtained from different approaches. To preserve clarity the refinements in space group $I4/mmm$ are presented, which results also in reasonable fits with comparable residual values compared with refinements in space group $I4/m$ as exemplarily shown in Table 5.3. Upon annealing, the full width half maximum (FWHM) of the reflections decreased and superstructure reflections became more pronounced. Furthermore, the amount of the starting material (FeSe) was reduced, if still present after the initial reaction. This indicates a persisting inhomogeneous potassium distribution after the reaction. Presumably K rich $K_{1-x}Fe_{2-y}Se_2$ forms at the surface and large fractions of FeSe remain unreacted. Annealing can overcome this state by enhancing the diffusion, which results in an increased amount of $K_{1-x}Fe_{2-y}Se_2$ with less FeSe as schematically depicted in Figure 5.4 and illustrated in Figure 5.6.

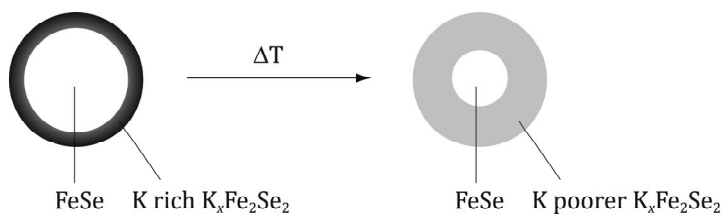


Figure 5.4 Schematic representation of an arising K gradient at the surface (left), reduced by annealing due to a more homogeneous distribution over a larger area (right).

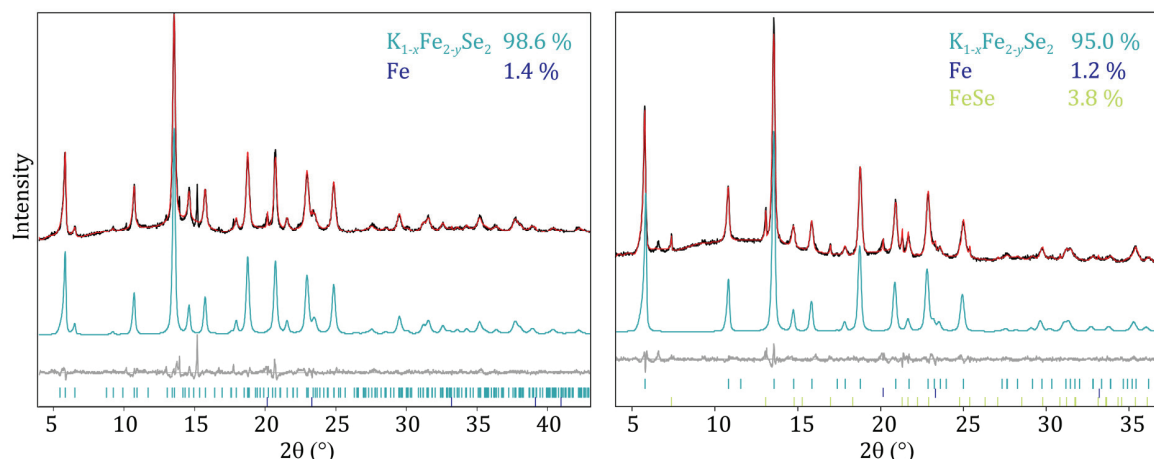


Figure 5.5 X-ray powder diffraction pattern of $K_{1-x}Fe_{2-y}Se_2$ synthesized from 1.0 eq K/TEMPO refined in $I4/m$ (left) (reflection at 15 2θ is an unknown impurity) and of $K_{1-x}Fe_{2-y}Se_2$ synthesized from 0.4 K/biphenyl after annealing for 44 h at 225 °C refined in $I4/mmm$ for comparison (right).

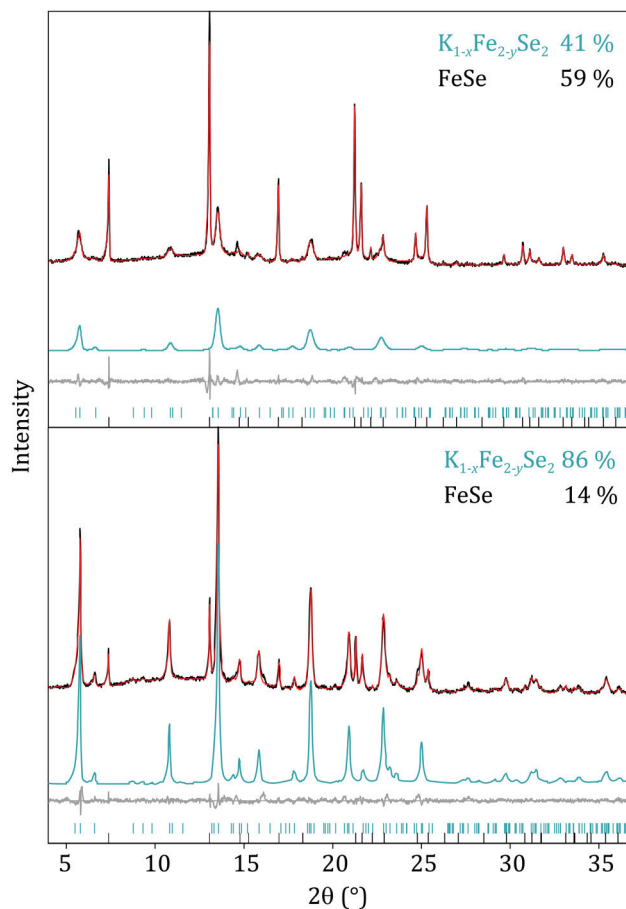


Figure 5.6 X-Ray powder diffraction pattern of $K_{1-x}Fe_{2-y}Se_2$ synthesized from slow adding of a 0.5 eq K/biphenyl solution after initial reaction (top) and after annealing for 170 h at 225 °C (bottom), refined in space group $I4/m$.

5.4 Magnetic measurements

AC susceptibility data of some samples revealed a paramagnetic curvature with a steep decrease at 12 K, whereas other samples showed a slow decrease over the whole temperature range (Figure 5.7, left and inset). The susceptibility values, however, remained positive. Annealing did not qualitatively alter the characteristics. The 12 K transition could either be AFM ordering or superconductivity. If potassium was added slowly (~ 0.5 eq. K), negative susceptibilities were visible at low temperatures and transitions occurred at around 21 K and below 9 K. The latter could be attributed to the T_c of precursor FeSe, which was still the main phase after the initial reaction. The transition at 21 K may originate from a new superconducting $K_{1-x}Fe_{2-y}Se_2$ phase. After annealing, this transition disappeared.

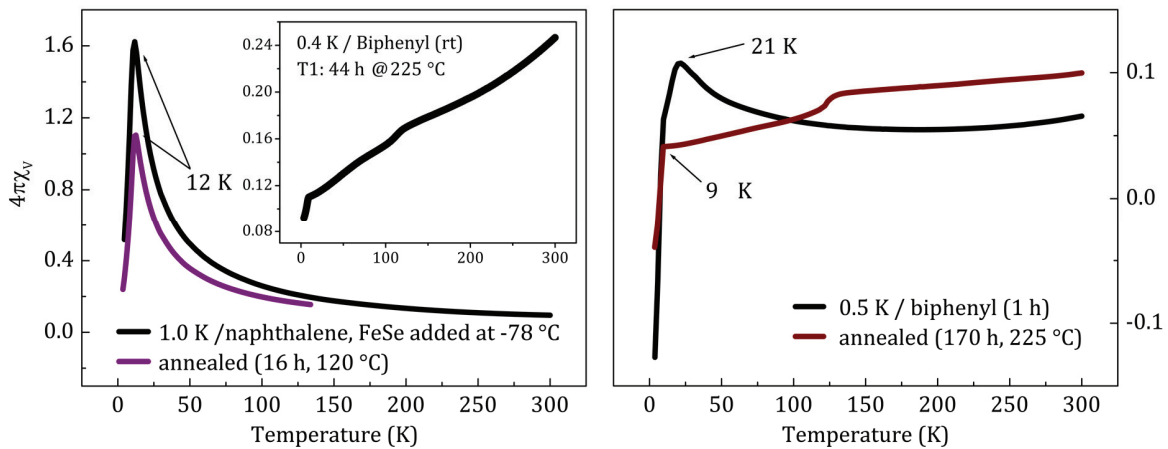


Figure 5.7 Susceptibility data of $K_{1-x}Fe_{2-y}Se_2$ synthesized by diverse approaches.

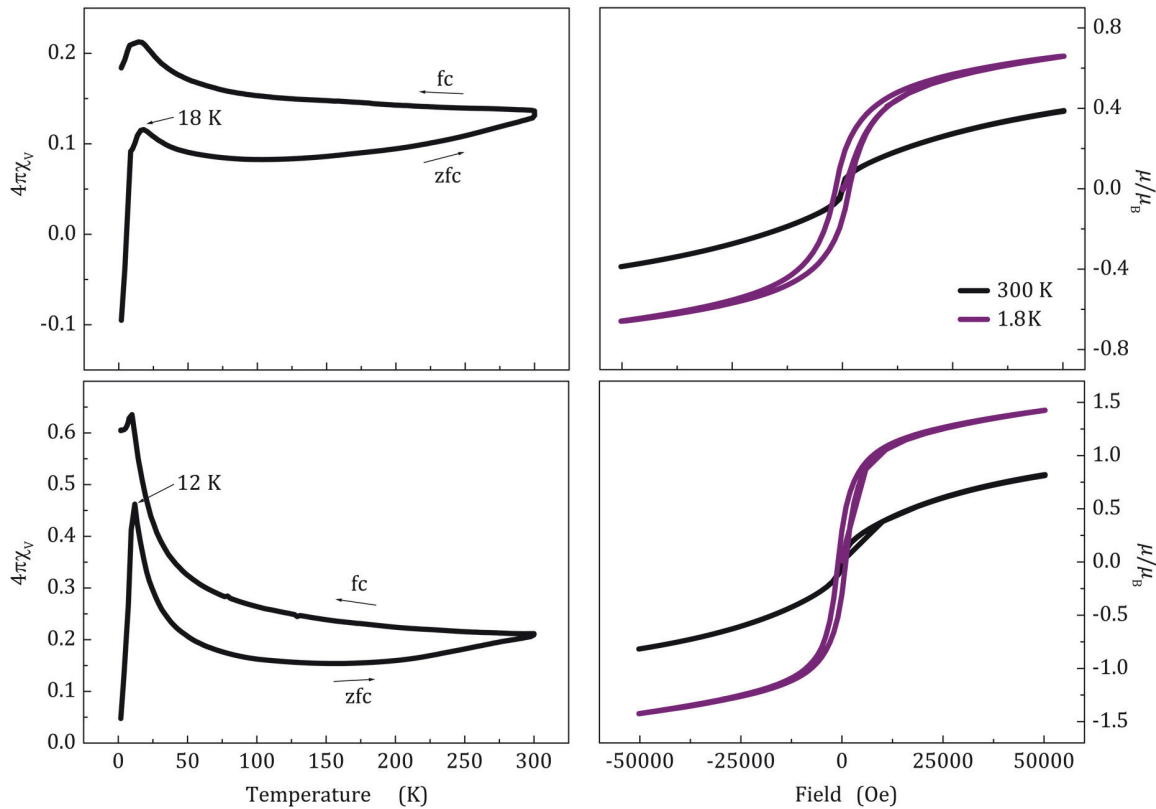


Figure 5.8 Susceptibility under zfc/fc conditions for $K_{1-x}Fe_{2-y}Se_2$ synthesized by slow adding of 0.5 eq K/biphenyl (top left) and hysteresis at 300 K (black) and 1.8 K (purple) (top right). Susceptibility under zfc/fc conditions for $K_{1-x}Fe_{2-y}Se_2$ synthesized with 1.2 K/18-crown-6 (bottom left) and hysteresis at 300 K (black) and 1.8 K (purple) (bottom right).

In susceptibility measurements under zero field cooled (zfc) and field cooled (fc) conditions the transitions at ~ 20 K and 12 K appear in both parts (zfc and fc), indicating the presence of superconductivity. For the 12 K transition antiferromagnetic ordering is also a valid theory, but the strong decrease rather indicates a superconducting transition. The splitting of the curves over the whole

temperature range with positive values is indicative for ferro- or ferrimagnetic behavior with T_C (Curie temperature) higher than 300 K. This agrees with the ferromagnetic behavior of the samples, when conducted to a permanent magnet.

This finding is presumably attributed to Fe, which is formed upon K intercalation. Isothermal magnetizations revealed magnetic moments up to $\sim 1.5 \mu/\mu_B$ with small hystereses at 1.8 K. These values presumably consist of intrinsic magnetic properties and contributions from Fe. The latter might dominate, since XRPD indicated significant Fe deficiency in $K_{1-x}Fe_{2-y}Se_2$. If the extracted iron is nano-structured as a consequence of the mild conditions, it might not be visible in XRPD but in magnetic measurements.

5.5 Electrical resistivity

The electrical resistivity reveals an increase at low temperatures reflecting semiconducting behavior (e.g. Mott insulator) (Figure 5.9). Plotting $-\ln \sigma$ against $T^{-1/4}$ according to the variable range hopping (VRH) model shows a nearly linear curvature (inset Figure 5.9). This resistivity course is consistent with literature results.^[93]

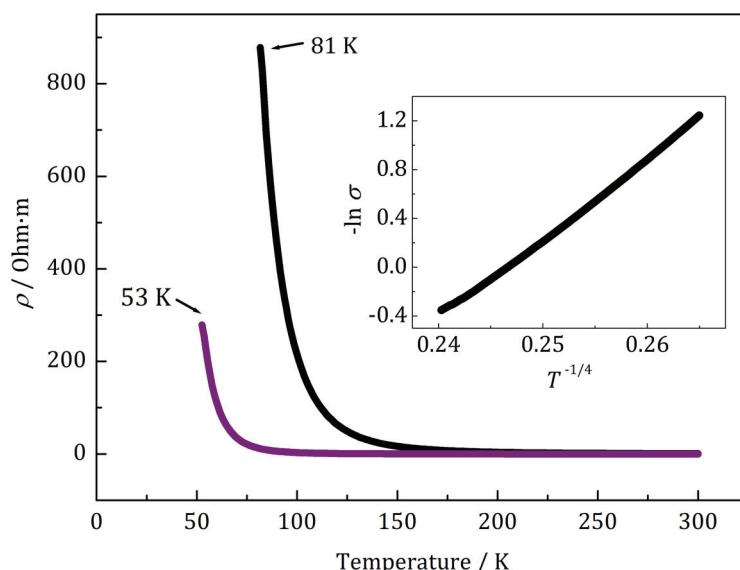


Figure 5.9 Specific resistivity of $K_{1-x}Fe_{2-y}Se_2$. 1.0 K/biphenyl (black) and 0.6 K/biphenyl (purple). Plot according to VRH model of the black curve (inset).

5.6 Conclusion

$K_{1-x}Fe_{2-y}Se_2$ was successfully synthesized via reductive intercalations, using a variety of K containing organic reducing agents. The phases obtained by these approaches showed a significant iron deficiency (~20%), whereby elemental iron appears as magnetic impurity. As indicated by small superstructure reflections, imperfectly ordered 245-phases are formed but no deficient 122-phases with a random distribution of Fe vacancies. The deviation from an ideal Fe vacancy order is a consequence of the divergence from $K_2Fe_4Se_5$ stoichiometry and disorder. Contrary to perfectly $\sqrt{5} \times \sqrt{5}$ vacancy ordered 245-phases the obtained compounds neither indicate AFM at high temperatures, nor superconductivity below 32 K, caused by phase separation with $K_{1-x}Fe_2Se_2$ formation. Instead, indications of superconducting transitions at 20 and 12 K were found. These values clearly deviate from T_c s of FeSe (8 K) or solid state synthesized $K_{1-x}Fe_{2-y}Se_2$ (32 K). Thus, these mild reductive intercalation routes offer the opportunity to receive new phases with superconducting properties within the K-Fe-Se system.

In general, this method is not restricted to potassium. First experiments with Li and Na indicated the possibility of intercalating smaller alkali metal ions into FeSe. By producing Rieke-metals even alkaline earth metals may serve as guest species. EAl_2 can be used as EA metal source and can be reduced *in situ* with A/organic species, as described in this chapter, by co-forming the respective AI and reactive EA^0 .

6 NaFe_{1-y}Co_yAs

6.1 Introduction

NaFeAs belongs to the so-called 111 class of iron-based superconductors and crystallizes in the *a*-PbFCl-type structure with space group *P4/nmm*. The structure exhibits the common edge sharing FeAs_{4/4} tetrahedral layers as present in the 11-type compounds, but in this case separated by double layers of sodium atoms. At first NaFeAs was thought to be superconductive in stoichiometric form. But the compound is highly air sensitive, which is why the partial extraction of sodium atoms had been discussed as reason for the induction of superconductivity. Hence, only slightly Na deficient compounds are superconducting with reported *T_c*s ranging from 5 to 20 K.^[99] By contrast, stoichiometric NaFeAs should exhibit the common antiferromagnetic ordering accompanied with a structural transition towards orthorhombic symmetry, as known for other parent compounds of iron-based superconductors.

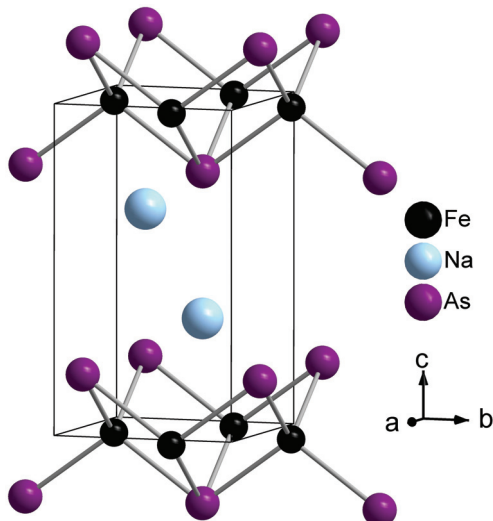


Figure 6.1 Crystal structure of NaFeAs, space group *P4/nmm* origin choice 2.

Due to its high sensitivity, stoichiometric NaFeAs is difficult to obtain, making it complicated to prove these assumptions. The current consensus is that the stoichiometric compound is indeed not superconducting and exhibits both, the structural transition as well as a collinear AFM ordering with a very low magnetic moment of the Fe atoms with only $0.090 \pm 04 \mu_B$.^[100]

Lower sodium contents suppress the magnetic state and bulk superconductivity emerges. Furthermore, the superconducting state can be induced by isovalent substitution with phosphorus on the arsenic site or by electron-doping with e.g. cobalt on the iron site. NaFeAs_{1-z}P_z single crystals are superconducting below 33 K.^[101] However, all efforts to obtain P-doped polycrystalline samples remained unsuccessful. Also for NaFe_{1-y}Co_yAs, predominantly single crystals were investigated in the literature.^[102, 103] For powder samples an ideal doping value is NaFe_{0.975}Co_{0.025}As with $T_c = 21$ K, synthesized in a two step synthesis starting from the elements.^[104] The homogeneity of the Co distribution may influence the properties. Therefore an adapted synthesis was applied, using mixed ternary Fe_{1-x}Co_xAs as precursor.

6.2 Synthesis

Polycrystalline NaFe_{1-y}Co_yAs was synthesized from Fe_{1-y}Co_yAs ($y = 0, 0.025, 0.05, 0.07, 0.1, 0.15, 0.2$) in order to realize a homogeneous distribution of cobalt. Stoichiometric mixtures of the elements (Fe, Co, As) were sealed in silica ampoules, heated to 700 °C for 65 h, homogenized and annealed at 750 °C (35 h). Sodium was added to Fe_{1-y}Co_yAs, welded in a Niobium crucible, which was put inside a silica ampoule and heated to 750 °C for 60 h. NaFe_{1-y}Co_yAs was obtained as highly air sensitive gray powder with metallic luster.

6.3 Crystal structure

Powder X-ray diffraction (XRPD) verified the tetragonal structure (space group $P4/nmm$) of the 111 compounds. Tiny amounts of an Fe impurity only occurred for $y = 0.025, 0.05$. Due to the smaller radius of cobalt (58 pm, Co²⁺)^[105] compared to iron (63 pm, Fe²⁺)^[105] the TM-As distance is shortened by 0.7 % with increasing Co content y with $y_{\max} = 0.2$ (Figure 6.3 (top left)).

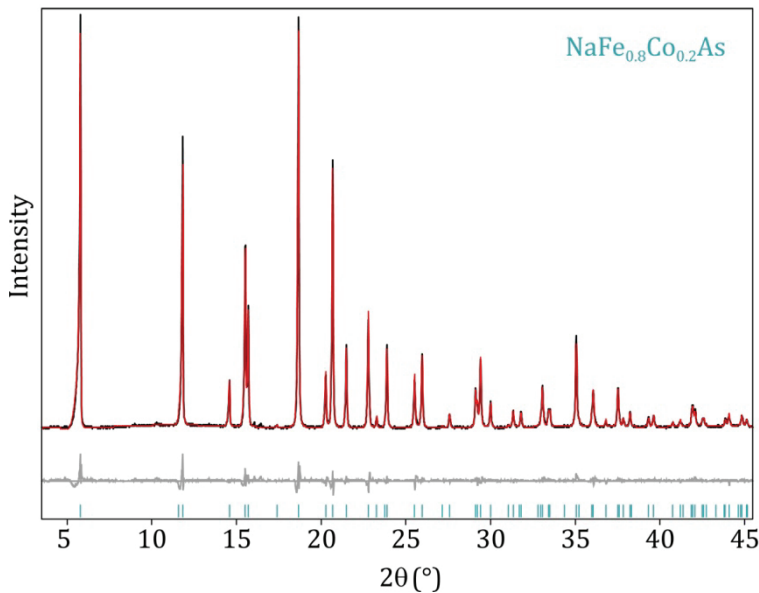


Figure 6.2 Observed (black) and calculated (red) powder X-ray diffraction pattern together with the difference profile (gray) of the Rietveld refinement of NaFe_{0.8}Co_{0.2}As. Peak positions are marked by vertical lines.

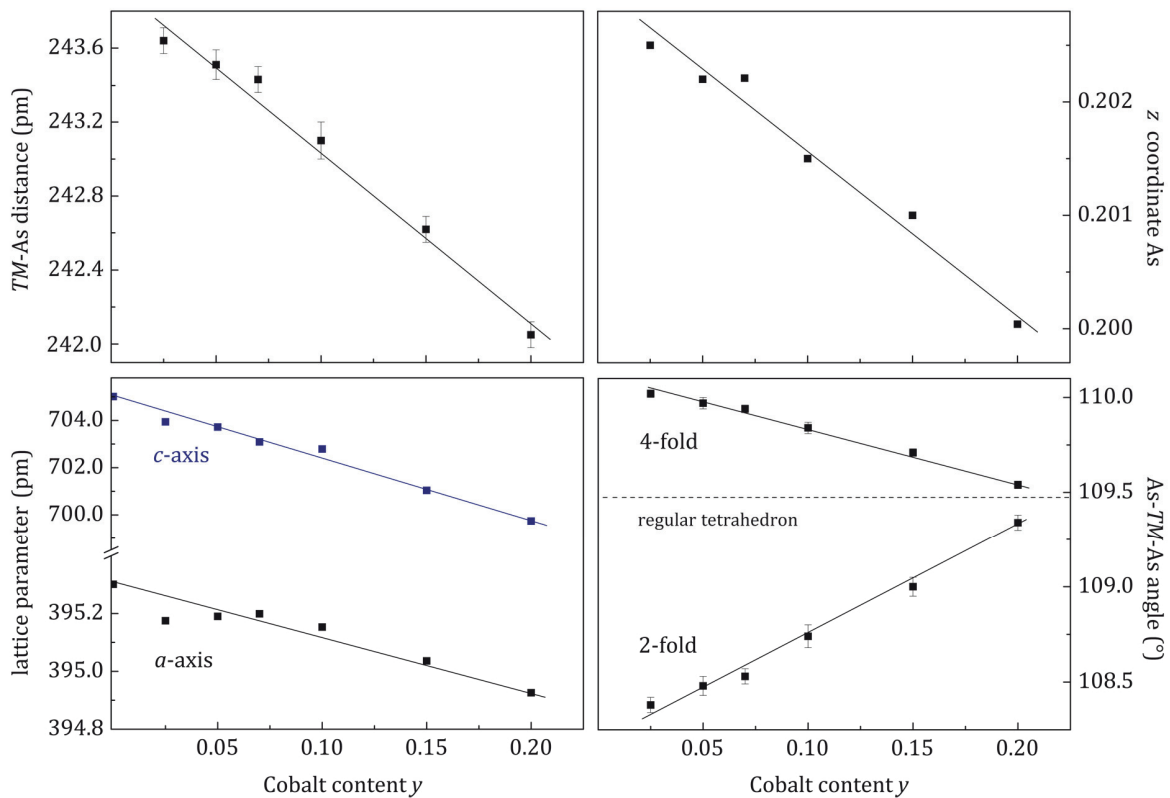


Figure 6.3 Variation of the structural parameters in NaFe_{1-y}Co_yAs. Distance TM-As (top left), z coordinate of arsenic and the lattice parameters a and c (bottom left) and TM-As tetrahedral angles (bottom right).

Resulting from this fact, the z coordinate of arsenic and the lattice parameters a and c decreased with increasing Co content y , too (Figure 6.3 (top right and bottom left)).

The lattice parameter a decreased by 0.1 % and c by 0.8 %. Due to the shorter c -axis the 2-fold angle increases, representing a flattening of the tetrahedral sheets along c . The ideal tetrahedral angle of 109.47 ° extrapolated from the plot is reached with approximately $y = 0.23$ (Figure 6.3 (bottom right)). An ideal tetrahedral angle is assumed as factor for reaching higher T_{cS} ^[106] and is further discussed in Chapter 6.4. The composition of NaFe_{1-y}Co_yAs was determined by EDX, supporting a homogeneous Co distribution (see Table 6.1). Sodium and iron are found slightly overestimated compared to the nominal composition. The Fe : Co ratio (summed to one) fits within the experimental error.

Table 6.1 Composition of NaFe_{1-y}Co_yAs as determined by EDX measurements referred to As together with the Fe : Co ratio.

Nominal composition	Measured composition	Fe : Co ratio
NaFe _{0.975} Co _{0.025} As	Na _{1.31} Fe _{1.05} Co _{0.02} As	0.98 : 0.02
NaFe _{0.95} Co _{0.05} As	Na _{1.23} Fe _{1.00} Co _{0.04} As	0.96 : 0.04
NaFe _{0.93} Co _{0.07} As	Na _{1.16} Fe _{1.02} Co _{0.05} As	0.95 : 0.05
NaFe _{0.90} Co _{0.10} As	Na _{1.24} Fe _{0.98} Co _{0.09} As	0.92 : 0.08
NaFe _{0.85} Co _{0.15} As	Na _{1.23} Fe _{0.93} Co _{0.13} As	0.88 : 0.12
NaFe _{0.80} Co _{0.20} As	Na _{1.25} Fe _{0.90} Co _{0.17} As	0.84 : 0.16

6.4 Magnetic measurements

AC susceptibilities of NaFe_{1-y}Co_yAs revealed a nearly constant T_c of 21 K irrespective of the cobalt content, but with varying volume fractions (see Figure 6.4 left). As mentioned before the tetrahedral angles become more regular with increasing Co content, whereby a raised T_c is expected. However, this was not observed, presumably because the crucial factor is the amount of substitution on the iron site. Manipulations within the active sheets are more effective to the superconducting properties than e.g. doping at interlayer sites. Thus, the superconducting region ($\sim 0 - 0.1$) is narrower for Co substitution than indirect doping.^[107] Performing the synthesis as described in the literature,^[104] led to a very broad, barely distinctive superconducting transition as depicted in Figure 6.4 right (red curve), contrary to a reported sharp transition at 11 K. A further annealing step, which was not performed according to the literature, revealed a superconducting transition, but with a T_c of

21 K (pink curve, Figure 6.4). Due to the further annealing a ferromagnetic contribution arises, visible by a positive shift of the susceptibility. In comparison, by starting from mixed Fe_{1-y}Co_yAs, the susceptibility already reveals bulk superconductivity without further annealing of NaFe_{1-y}Co_yAs. This difference may be a consequence of an inhomogeneous cobalt distribution within the sample synthesized according to the literature (without additional annealing). The deviation of T_c (11 K literature, 21 K this study) should originate from other reasons, because both syntheses led to rather sharp transitions and bulk superconductivity. Deficiencies on the Na site can crucially influence the T_c in NaFeAs as well. Hence, they probably play an important role in NaFe_{1-y}Co_yAs, too. In order to evaluate influences by Na deficiency, sample 2 (synthesized from Fe_{1-y}Co_yAs) was conducted to air. Hereby some sodium should be extracted whereby superconductivity can be affected, but should be retained. However, a subsequent measurement of the susceptibility revealed the absence of superconductivity (Figure 6.4, gray curve).

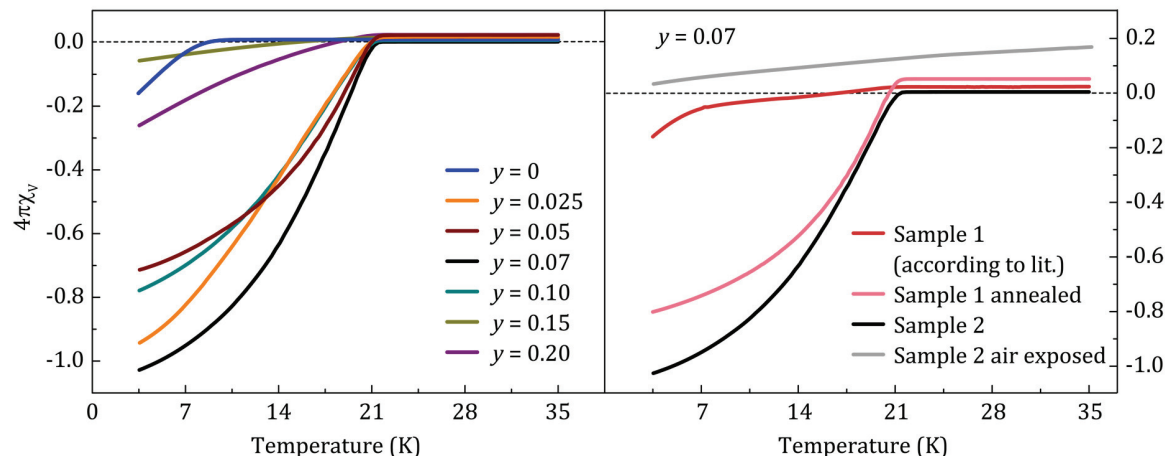


Figure 6.4 AC susceptibilities of $\text{NaFe}_{1-y}\text{Co}_y\text{As}$ synthesized from $\text{Fe}_{1-y}\text{Co}_y\text{As}$ (left) and for $y = 0.07$ (right) prepared according to literature (red curve), further annealed (pink curve), synthesized from a $\text{Fe}_{0.93}\text{Co}_{0.07}\text{As}$ precursor (black curve) and the same sample after exposure to air (gray curve).

6.5 Conclusion

NaFe_{1-y}Co_yAs samples with a homogeneous Co distribution were synthesized from Fe_{1-y}Co_yAs as precursor. The samples exhibited a constant T_c of about 21 K with varying volume fractions depending of the cobalt content, in contrast to literature results. An inhomogeneous cobalt distribution with fractions of ideally doped

NaFe_{1-y}Co_yAs in each sample causing the constant onset of T_c at 21 K is rather unlikely because the synthesis conditions were especially adapted to counteract this. The observation of sharp transitions and bulk superconductivity verifies the homogeneous Co distribution. As mentioned before, also the Na content is crucial to superconductivity. After air exposure the T_c is found increased in NaFeAs, but generally visible as rather broad, less pronounced transition, which was not observed here. Possibly small differences of the Na content, caused during synthesis and/or sample handling might explain the difference. The reason for constant T_{cS} s cannot readily be determined by common analytical methods. Further detailed investigations of e.g. the local structure and/or a very accurate determination of the Na content are necessary and might reveal the actual origin.

Nevertheless, electron doped NaFe_{1-y}Co_yAs can be used to investigate a potential oxidative deintercalation by removing e.g. half of the Na atoms, as presented in Chapter 8.

7 $\text{Na}_{1-x}\text{Fe}_{2-y}\text{As}_2$ via oxidative deintercalation

Main parts of this chapter are published and reprinted with permission from G. M. Friederichs, I. Schellenberg, R. Pöttgen, V. Doppel, L. Kienle, J. Schmedt auf der Günne, D. Johrendt, *Inorg. Chem.* **2012**, *51*, 8161.

Copyright © 2012 American Chemical Society. DOI: 10.1021/ic3005618

<http://pubs.acs.org/doi/abs/10.1021/ic3005618>

7.1 Introduction

Iron-based superconductors have inspired the field of high-temperature superconductivity research.^[108] While the already achieved progress with respect to the properties and underlying physics of these materials is enormous,^[109] the further development of their chemistry is still in the early stages. Currently, conventional solid-state synthesis at high temperatures yield thermodynamically stable compounds like $\text{La}(\text{O}_{1-x}\text{F}_x)\text{FeAs}$,^[110] $(\text{Ba}_{1-x}\text{K}_x)\text{Fe}_2\text{As}_2$,^[111] or $\text{Na}_{1-x}\text{FeAs}$,^[112] and related compounds,^[113] where superconductivity emerges in layers of edge-sharing $\infty^2(\text{FeAs}_{4/4})^-$ tetrahedra. Several kinds of doping control the charge of these layers and move the systems from antiferromagnetic^[114] to superconducting states.^[107, 115] So far, the highest critical temperature (T_c) observed in iron-based materials is around 55 K in $\text{Sm}(\text{O}_{0.85}\text{F}_{0.15})\text{FeAs}$,^[116] thus lower than in copper-oxide superconductors. However, all known iron-based superconductors are single-layer structures, with one crystallographically independent iron atom per unit cell. Keeping in mind that often multilayer copper oxides exhibit T_c 's above the temperature of liquid nitrogen, higher critical temperatures might be conceivable in multilayer iron arsenides. Generally, access to artificial FeAs multilayer superstructures seems possible by pulsed laser deposition methods,^[8, 9] which yield thin films only. It appears at least questionable, if high temperature methods alone will be able to produce novel iron-based materials, thus access to possible multilayer superstructures may require smart methods like the soft chemistry approach. The existence of the metastable iron arsenide NaFe_2As_2 with the ThCr_2Si_2 -type (122) structure has recently been reported.¹³ The authors declared a critical temperature from 12 up to 25 K, which is very high in comparison with the other known $A\text{Fe}_2\text{As}_2$

compounds ($A = \text{K}$ (4 K), Rb (3 K), Cs (2.6 K)). But already the existence of NaFe_2As_2 is remarkable, because the radius of the sodium ion was expected to be too small to fill the coordination polyhedron in the ThCr_2Si_2 -type structure. It is thus not surprising that this compound cannot be synthesized by solid state methods at higher temperatures. Indeed, NaFe_2As_2 decomposes already at 120 °C.^[117] A compound with the nominal composition $\text{Na}_{0.5}\text{FeAs}$ but a - PbFCl -type (111) structure and $T_c = 12$ K has also been reported.^[118] Further investigations of this material are important for two reasons. First, the T_c is remarkably high within this series, but more importantly, this compound may open new pathways to iron arsenide materials by soft chemistry methods. But so far, no comprehensible and reproducible method to synthesize NaFe_2As_2 has been published. In the first report,^[117] NaFeAs has been converted to NaFe_2As_2 in a not specified ionic liquid, but no further details of the experiment and the detailed composition of the product are given. According to another recent report,^[119] NaFe_2As_2 occurred as a minor byproduct in $\text{Na}_{1-x}\text{FeAs}$ during the decomposition of NaFeAs by exposing to air or water. Here, we present a reproducible method to synthesize this 122-type superconductor by topochemical deintercalation of NaFeAs at room temperature. The reaction product is thoroughly characterized by X-ray powder-diffraction (XRPD), magnetic measurements, ^{57}Fe -Mössbauer spectroscopy, energy dispersive X-ray analysis (EDX), ^{23}Na solid state nuclear magnetic resonance (NMR) spectroscopy, and high resolution transmission electron microscopy (HRTEM).

7.2 Synthesis

$\text{Na}_{1-x}\text{Fe}_{2-y}\text{As}_2$ was synthesized from NaFeAs as precursor, which was synthesized through solid state reaction from Na and FeAs, sealed in a welded niobium crucible and placed into a fused silica ampoule under argon. The mixture was heated to 700 °C for 48 h at 50 °C/h and then cooled to room temperature at 150 °C/h. Powder X-ray diffraction showed single phase NaFeAs .

To obtain $\text{Na}_{1-x}\text{Fe}_{2-y}\text{As}_2$ from NaFeAs (0.40 g, 2.60 mmol) the precursor was oxidized with iodine (0.53 g, 2.08 mmol, 0.8 equiv). The reagents were separately dispersed (NaFeAs) and solved (I_2) in dry THF (30–36 mL) respectively. The iodine solution was added slowly to NaFeAs (approximately 40 min.). The reaction mixture was stirred

for 40 h at room temperature, than the solid product Na_{1-x}Fe_{2-y}As₂, which is gray with metallic luster, was filtered off and was dried under high vacuum.

All reaction steps were carried out under *Schlenk*-conditions. This (soft-chemistry) deintercalation process is a heterogenous liquid–solid reaction, which presumably starts at the surface of the particles arising a sodium gradient. At a critical point of sodium extraction the initially formed sodium deficient 111-phase Na_{1-x}FeAs is probably no more stable and transforms to the 122-type structure. The latter requires sliding of every second FeAs-layer by 1/2 translation along the lattice parameter *b*. These structural rearrangements may not proceed homogeneously within the crystals, which is probably responsible for the poor crystallinity of the samples.

For an optimization of the synthesis conditions several attempts had been carried out, however, neither performing the reaction at lower temperatures (-10 °C, -50 °C in THF) nor at higher temperatures (60 °C in THF, 90 °C in DMSO, 90 °C in THF (autoclave)) yielded a better sample quality. Further annealing of the product below the decomposition temperature of 120 °C did not improve the crystallinity, too. A conventional high-temperature solid-state synthesis is not feasible due to the metastable character of the compound. The reaction can also be performed in acetonitrile with comparable results. Recently the compound was synthesized by another group according to our synthesis in order to investigate the local structure. They also tried to obtain more crystalline samples by varying synthesis conditions, but also could not improve crystallinity.^[120]

7.3 Crystal structure

The X-ray powder diffraction (XRPD) pattern shown in Figure 7.1 displays a large background and broad diffraction peaks. All peak positions are consistent with a tetragonal body-centered unit cell with the lattice parameters *a* = 383.1(3) pm and *c* = 1252(2) pm, in agreement with those given for NaFe₂As₂.^[117] Broad humps in the background near the peak positions are suggestive of certain fractions of the sample having very small coherently scattering domains. To support this assumption, we have decomposed the pattern into three components as shown in Figure 7.1a.

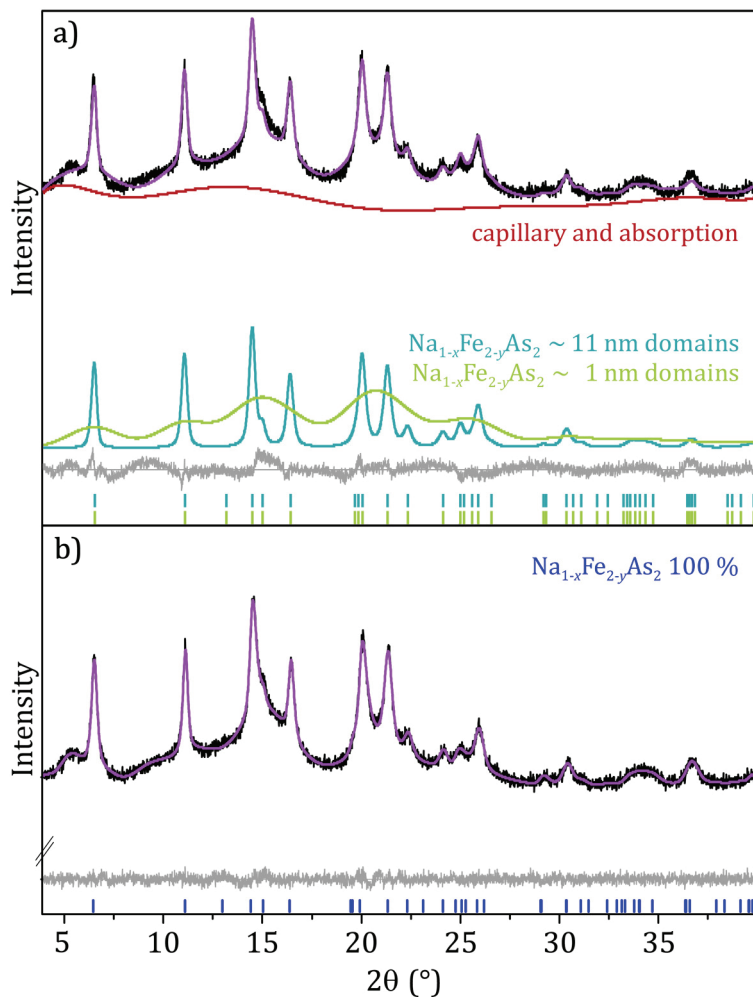


Figure 7.1 Observed (black) and calculated (violet) powder X-ray diffraction pattern together with the difference profiles (gray) of the Rietveld refinements of $\text{Na}_{1-x}\text{Fe}_{2-y}\text{As}_2$. Peak positions are marked by vertical lines. (a) Fit resulting from the addition of a simple background function with 10 parameters (red), 1 nm domains (green) and 11 nm domains (turquoise). (b) Fit with one phase and 36 parameters background function.

Table 7.1 Atomic coordinates, Wyckoff symbols, and isotropic displacement parameters U_{iso} (\AA^2) of $\text{Na}_{1-x}\text{Fe}_{2-y}\text{As}_2$, space group $I4/mmm$, $a = 383.1(3)$ pm, $c = 1252(2)$ pm, $Z = 2^{\text{a}}$

atom	Wyckoff	x	y	z	U_{iso}	occ.
Na	2a	0	0	0	0.02(1) ^b	0.99(4) ^c
Fe	4d	0	½	¼	0.020(6)	0.81(2)
As	4e	0	0	0.366(1)	0.038(5)	1

a $R_{\text{wp}} = 1.097$, $R_{\text{p}} = 0.881$, $\chi^2 = 0.97$, $R_{\text{Bragg}} = 0.0985$.

b Restrained as maximum value.

c Restrained to occ. ≤ 1 .

First, a rather simple background function (10 parameters) describes the contributions of the capillary and the sample absorption. The second component is the scattering of very small $\text{Na}_{1-x}\text{Fe}_{2-y}\text{As}_2$ domains (~ 1 nm) which produces the

humps. Finally we add the scattering of larger, but still small domains (~ 11 nm) of $\text{Na}_{1-x}\text{Fe}_{2-y}\text{As}_2$ that give rise to the peaks. The sum of these three components is already a reasonable fit of the observed pattern in Figure 7.1a. However, this model is still too simple to fit the pattern quantitatively. A significantly better fit results by the standard procedure with one crystalline phase and 36 background parameters (Figure 7.1b), which has finally been used to obtain the structure parameters compiled in Table 7.1.

Refinements of the occupation parameters revealed the composition $\text{Na}_{0.99(4)}\text{Fe}_{1.62(2)}\text{As}_2$. Due to the small scattering power, the sodium content is relatively inaccurate. We also suggest that the Rietveld refinement slightly overestimates the sodium occupation, because only domain sizes larger than ~ 11 nm are considered, while the scattering of smaller domains with probably less sodium is covered by the background function. Nevertheless, our analysis shows that the sample is one crystallographic phase, and the background as well as the broad peaks can be explained by small domain sizes and fluctuations of the chemical composition. The latter is confirmed by the EDX nanoprobe analysis of several areas. Table 7.2 shows results of the EDX nanoprobe measurements.

Table 7.2 EDX nanoprobe analysis of $\text{Na}_{1-x}\text{Fe}_{2-y}\text{As}_2$.^a

no.	Na	Fe	As	Na/Fe/As
1	21.6	36.4	42.1	1.0: 1.7: 2
2	18.5	37.1	44.4	0.8: 1.7: 2
3	13.8	36.9	49.3	0.6: 1.5: 2
4	22.9	37.0	40.1	1.1: 1.9: 2
5	24.1	36.4	39.5	1.2: 1.8: 2
6	19.1	35.6	45.3	0.8: 1.6: 2
7	19.5	35.6	44.9	0.9: 1.6: 2
8	17.1	37.7	45.1	0.8: 1.7: 2
9	19.5	36.8	43.7	0.9: 1.7: 2
Ø				0.9(2): 1.7(1): 2

a Values are given in atom-% and also normalized to 1:2:2 stoichiometry assuming fully occupied arsenic.

All areas reveal iron deficiency. The mean value is 1.7(1) in agreement with the Rietveld refinement of the XRPD data, and with the fact that dissolved iron ions were

detected in the THF solution after the reaction. The sodium content fluctuates much stronger and results in a mean value of 0.9(2). Even though some areas are close to the 122-stoichiometry, the EDX-results clearly indicate fluctuating iron and also sodium concentrations. We assume that especially the sodium disorder is responsible for the low crystallinity and thus the broadening of the X-ray diffraction peaks.

Figure 7.2 shows the crystal structures of the precursor NaFeAs and the product $\text{Na}_{1-x}\text{Fe}_{2-y}\text{As}_2$. Both compounds contain layers of edge sharing $\text{FeAs}_{4/4}$ tetrahedra, which are separated either by double layers of sodium ions in NaFeAs or by single layers of sodium atoms in $\text{Na}_{1-x}\text{Fe}_{2-y}\text{As}_2$. Thus in the course of the topochemical transformation from NaFeAs to $\text{Na}_{1-x}\text{Fe}_{2-y}\text{As}_2$, half of the sodium ions are removed, and every second FeAs-layer has to slide 1/2 period along the lattice parameter b (Figure 7.2).

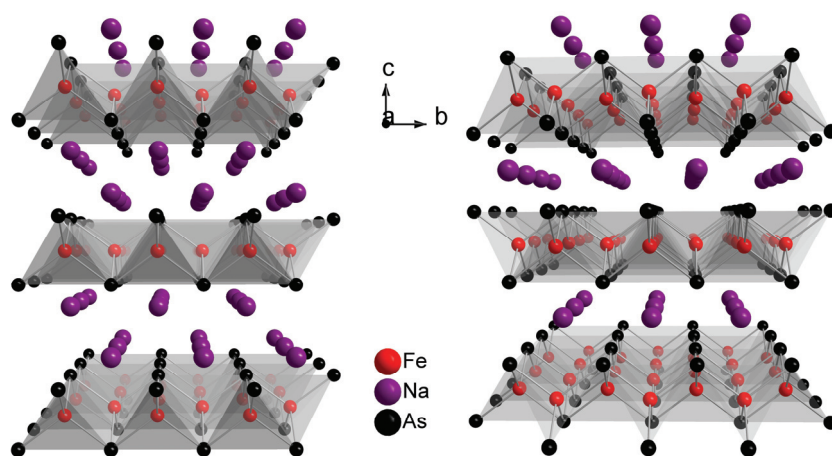


Figure 7.2 Crystal structures of NaFeAs (left) and $\text{Na}_{1-x}\text{Fe}_{2-y}\text{As}_2$ (right).

The Fe–As distance of 240.5(12) pm is typical for iron–arsenide superconductors, and also the slightly elongated FeAs_4 tetrahedron in terms of the 2-fold As–Fe–As angle ($105.6(8)^\circ$) has been observed, for example, in KFe_2As_2 ($107.02(5)^\circ$). Remarkably, the arsenic atoms of adjacent layers remain in a nonbonding state according to a distance of 335.0(9) pm in spite of the much smaller radius of Na^+ (116 pm) in comparison to K^+ (151 pm).

7.4 Magnetic measurements

The magnetic susceptibility of $\text{Na}_{1-x}\text{Fe}_{2-y}\text{As}_2$ was measured in a 15 Oe magnetic field under zero-field-cooled (zfc) and field-cooled (fc) conditions (Figure 7.3). Strong diamagnetism associated with the shielding-/Meissner-effect of superconductivity was detected below a critical temperature of 11 K. In contrast to this, *Gooch et al.*^[117] reported a weak onset of diamagnetism already at 25 K prior to a steep decrease of the susceptibility below 10 K. The 25 K feature is not visible in our measurement, while the second transition near to 11 K is observed in our sample. *Todorov et al.* likewise reported a critical temperature around 25 K, but for sodium-deficient $\text{Na}_{1-x}\text{FeAs}$ with 111-type structure, while a T_c of 12 K has been assigned to a compound referred to as NaFe_2As_2 , which is in agreement with our results.^[119] From this we suspect that the 25 K transition reported in ref. [117] is due to a small impurity of sodium deficient $\text{Na}_{1-x}\text{FeAs}$.

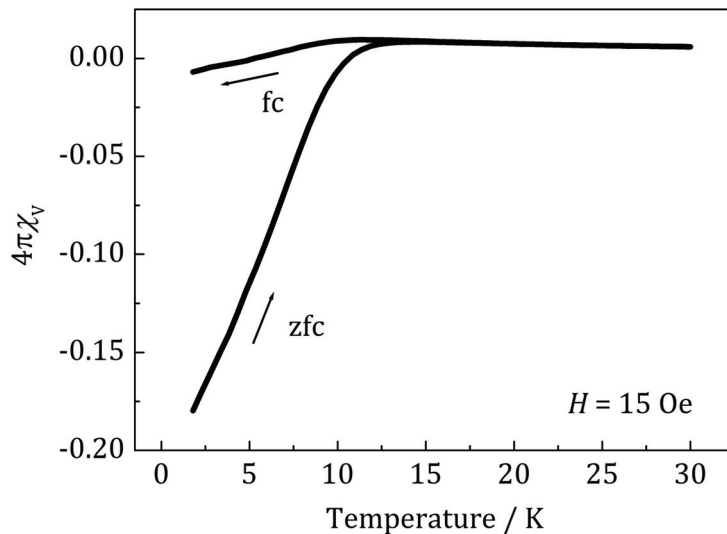


Figure 7.3 Susceptibility of $\text{Na}_{1-x}\text{Fe}_{2-y}\text{As}_2$ under zero field cooled (zfc) and field cooled (fc) conditions.

The estimated superconducting volume fraction is about 20%, which can safely be assigned to $\text{Na}_{1-x}\text{Fe}_{2-y}\text{As}_2$ because no residual NaFeAs is discernible in the X-ray powder pattern. However, the relatively broad transition indicates a certain distribution of the composition. One may assume that the superconducting phase is close to or even identical with the stoichiometric (1:2:2), however, from our data it is only clear that the superconducting phase has the 122-type structure, while the exact

composition with respect to the values of x and y in the superconducting fraction of $\text{Na}_{1-x}\text{Fe}_{2-y}\text{As}_2$ is still an open question.

7.5 ^{57}Fe -Mößbauer spectroscopy

Figure 7.4 presents ^{57}Fe Mössbauer spectra of the $\text{Na}_{1-x}\text{Fe}_{2-y}\text{As}_2$ sample at 298, 80, and 4.2 K together with transmission integral fits. The corresponding fitting parameters are listed in Table 7.3. All three spectra are well reproduced with single signals which were subjected to weak quadrupole splitting. The increase of the isomer shift with decreasing temperature ($0.24 \rightarrow 0.38 \text{ mm/s}$) is a consequence of a second order Doppler shift, similar to recent investigations on SrFe_2As_2 , SrFeAsF , and KFe_2As_2 .^[121-123] Weak quadrupole splitting results from a deviation of the ideal tetrahedral $\text{FeAs}_{4/4}$ coordination.

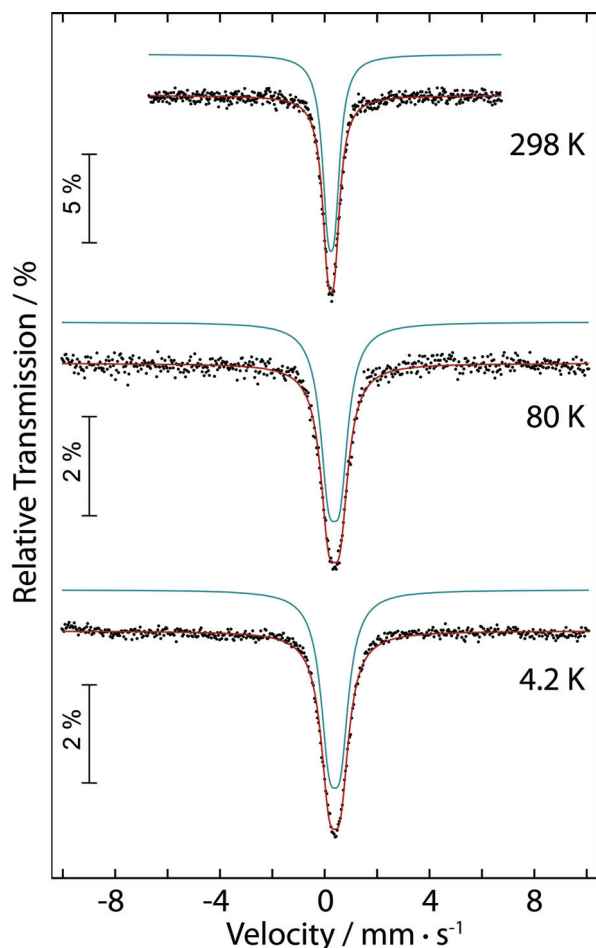


Figure 7.4 Experimental and simulated ^{57}Fe Mössbauer spectra of $\text{Na}_{1-x}\text{Fe}_{2-y}\text{As}_2$ at 298, 80, and 4.2 K.

In contrast to other iron arsenides, we observe a significant increase of the experimental line width. Although one might expect that the small refined quadrupole splitting parameters and the increased line width parameters might correlate, the high quality of the fits clearly point to the increased line width parameters. We ascribe this line width increase to the distribution of very small sized domains within the Na_{1-x}Fe_{2-y}As₂ particles. Such a behavior has also been observed for amorphous SnO₂,^[124] which shows much higher line width than well crystallized SnO₂. Another reason might be the homogeneity range of Na_{1-y}Fe_{2-x}As₂. ⁵⁷Fe Mössbauer spectra of NaFeAs reported by Todorov^[119] showed higher isomer shifts than the Na_{1-x}Fe_{2-y}As₂ sample reported herein. Since we observe no shoulder in our spectra at higher velocity, we can exclude a notable residual NaFeAs in our sample in agreement with XRPD and TEM. No magnetic hyperfine field splitting is evident down to 4.2 K. This is another hint for the purity of our sample, since NaFeAs shows charge-density-wave formation below 40 K with a small, but notable hyperfine field at low temperatures.

Table 7.3 Fitting parameters of the ⁵⁷Fe mössbauer spectra of Na_{1-x}Fe_{2-y}As₂ at different temperatures.^a

T (K)	δ (mm·s ⁻¹)	Γ (mm·s ⁻¹)	ΔEQ (mm·s ⁻¹)
298	0.24(1)	0.52(1)	0.26(1)
80	0.36(1)	0.77(2)	0.44(1)
4.2	0.38(1)	0.78(1)	0.44(1)

^a Numbers in parentheses represent the statistical errors in the last digit. (δ) isomer shift; (Γ) experimental line width, (ΔEQ) quadrupole splitting parameter.

7.6 Solid state NMR spectroscopy

So far all results consistently point to deviations from the ideal 1:2:2 composition in Na_{1-x}Fe_{2-y}As₂. In order to examine this finding more closely, we have further analyzed the sample by ²³Na solid-state NMR spectroscopy and transmission electron microscopy (TEM).

²³Na MAS spectra of Na_{1-x}Fe_{2-y}As₂ have been measured, and for comparison also of the precursor NaFeAs and Ba_{0.6}Na_{0.4}Fe₂As₂, the latter has an inherent Ba/Na site disorder (Figure 7.5). Moreover we obtained T_1 relaxation time constants in order to get an indication whether relaxation contributes differently to the line width via

lifetime broadening of the resonances. However T_1 relaxation time constants at room temperature are all in the range of $0.3 \pm 0.2\text{s}$. We can also exclude a dominant contribution to the line width by the paramagnetic chemical shift caused by hyperfine coupling to unpaired electron spins because the observed chemical shift values hardly change when the sample temperature is increased by about 10 K. Furthermore we have estimated the quadrupole coupling constant C_Q of NaFeAs at room temperature from a ^{23}Na satellite transition MAS NMR spectrum^[125] ($|C_Q| = 0.9 \text{ MHz}$, not shown) and that of NaFe_2As_2 theoretically by DFT calculations ($C_Q = 1.0 \text{ MHz}$). The asymmetry parameter, η_Q is zero by symmetry in both cases. The expected second-order quadrupolar broadening of the central transition is only of the order of 250 Hz under the chosen experimental conditions and thus not significant. The ^{23}Na line width of NaFeAs and of $\text{Ba}_{0.6}\text{Na}_{0.4}\text{Fe}_2\text{As}_2$ is an order of magnitude less than that of the title compound $\text{Na}_{1-x}\text{Fe}_{2-y}\text{As}_2$. We can exclude also second order quadrupolar shift, relaxation effects and a paramagnetic broadening mechanism as the source of broadening as shown above. Hence we conclude that the broadening of the ^{23}Na resonance gives evidence of disorder of Na on an atomic scale.

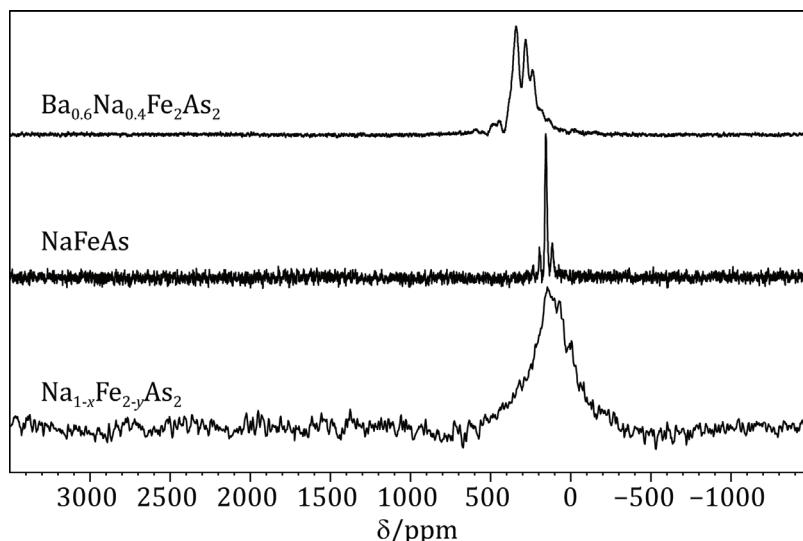


Figure 7.5 ^{23}Na solid-state MAS NMR spectra of $\text{Na}_{1-x}\text{Fe}_{2-y}\text{As}_2$ (bottom), NaFeAs (middle), and $\text{Ba}_{0.6}\text{Na}_{0.4}\text{Fe}_2\text{As}_2$ (top).

7.7 TEM measurements

According to bright field images, the sample does not contain nanoparticles but crystals with a low expansion of the coherently scattering domains/areas. This is

consistent with the powder XRD pattern and explains the observed reflection profiles. EDX nanoprobe measurements indicate the absence of oxygen contaminations. Several crystals which can be assigned via electron diffraction to the 122-type structure were chemically analyzed by EDX (see Table 7.2). During the experiments it emerged that the crystallites are quite radiation sensitive under standard emission settings. However, when adjusting low-dose settings, particularly by reducing emission, the samples do not change significantly their structure and chemical composition within the time slice of observation. Remarkably, all crystals exhibit planar defects which are well seen even immediately after the initial irradiation. Thus, the defects represent an intrinsic real structural feature and no artifact produced by electron beam impact. When adjusting the crystals along the zone axis [100], cf. Figure 7.6a, the planar defects appear as stripes parallel to the planes (001) in high resolution contrast. The presence of (001) defects is further supported by the presence of diffuse 00l-streaks in Fourier transforms of HRTEM micrographs (see Fourier transform from larger circle attached to Figure 7.6a). However in smaller areas the structure and the corresponding Fourier transforms do not exhibit any indication for disordering, cf. Fourier transform from the smaller circle attached to Figure 7.6a. Generally the PEDs which are recorded on large circular areas (diameter 250 nm) clearly show the diffuse streaks. Note, that all Bragg intensities are streaked, thus, the sizes of the perfectly crystalline areas are small. The PED patterns (e.g., Figure 7.6b and c, each left) recorded on single crystalline areas comply with the structure model from powder XRD as indicated by the convincing agreement with simulated patterns based on the kinematic approximation (Figure 7.6b and c, each right).

The local view on the structure by high-resolution imaging is demonstrated by the micrograph of Figure 7.7. The image was recorded close to Scherzer focus, thus, the dark contrasts correlate with the positions of the heavy atoms Fe and As, as indicated by the inserted simulated micrograph. The layered arrangement of these atoms along [010] is clearly seen, but the correlation between experimental and simulated micrograph is not perfect. However, such deviations are expected since the structure model for the simulation is based on the XRPD results, which take not into account

local deformations of the structure by fluctuations of the chemical composition, particularly concerning the Na content.

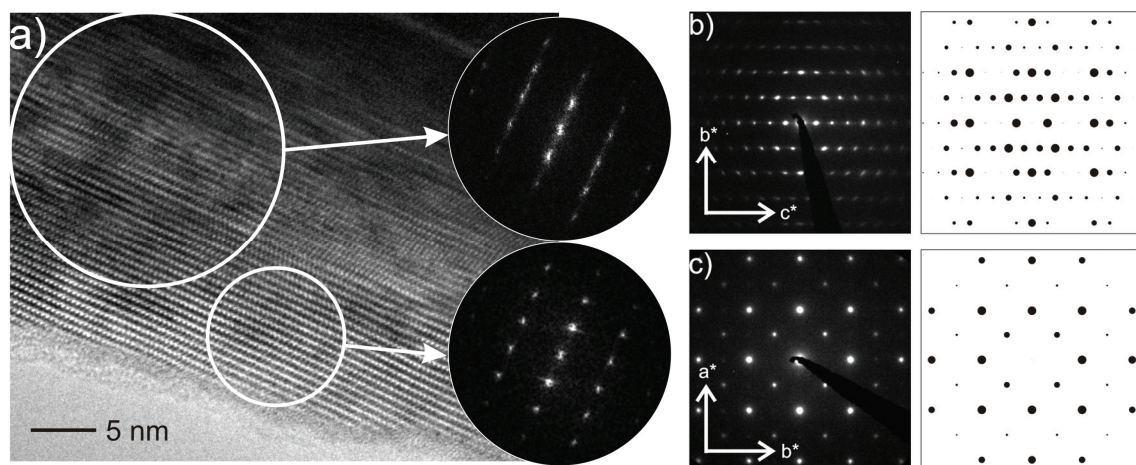


Figure 7.6 (a) HRTEM micrograph recorded on $\text{Na}_{1-x}\text{Fe}_{2-y}\text{As}_2$, zone axis [100] with attached Fourier transforms from the highlighted circular areas. (b and c) PED patterns (each left) and simulated patterns (each right) for the zone axes [100] and [001], respectively.

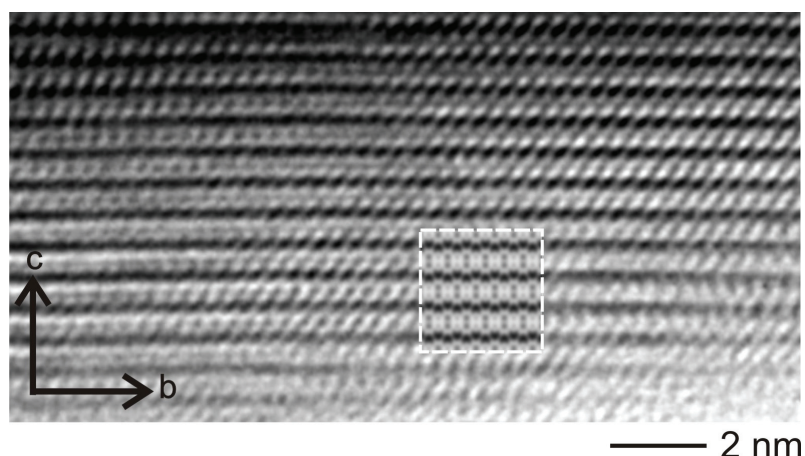


Figure 7.7 High resolution micrograph after Fourier filtering and inserted simulation for zone axis [100]. Parameters for simulation: thickness 3.8 nm, $\Delta f = -65$ nm.

7.8 Conclusion

We have presented a reproducible synthesis method and an extensive characterization of the iron arsenide $\text{Na}_{1-x}\text{Fe}_{2-y}\text{As}_2$. Our results show that the metastable compound has a deficient ThCr_2Si_2 -type structure with mean compositions $\text{Na}_{0.9(2)}\text{Fe}_{1.7(2)}\text{As}_2$ from EDX and $\text{Na}_{0.99(4)}\text{Fe}_{1.67(2)}\text{As}_2$ from Rietveld-refinements. Electron microscopy detects well crystalline and strongly distorted areas associated with a significant disorder of sodium in agreement with ^{23}Na -NMR data. This is probably the origin of the poor crystallinity of the sample that reduces

the accuracy of the X-ray powder diffraction experiment. However we could show that the large scattering background is caused by very small domain sizes of Na_{1-x}Fe_{2-y}As₂, and not by an amorphous foreign phase. This is supported by the ⁵⁷Fe Mössbauer spectrum which shows only one type of iron on the local scale. From this we infer that the sample is one crystallographic phase which suffers from fluctuating composition and very small coherently scattering domains. The latter is probably a consequence of the heterogeneous solid/liquid reaction at low temperature. We note that the exact composition of the compounds referred to as NaFe₂As₂ in two earlier reports^[117, 119] has not been scrutinized. Our susceptibility measurements reveal one superconducting transition at 11 K in agreement with the main transition in ref.^[117] and also with the transition that has been associated to NaFe₂As₂ in ref.^[119]. However, the shielding fraction is only 20% and with respect to the observed fluctuations of sodium and iron occupations, the true composition of the superconducting phase remains still unclear. Anyway the critical temperature of Na_{1-x}Fe_{2-y}As₂ is about three times higher than those of the higher homologues (K, 4 K; Rb and Cs, 3 K), and one may argue if this is a volume effect or connected to the nonstoichiometry. The iron deficiency is actually surprising because electron counting according to Na_{~1}⁺Fe_{1.67}³⁺As₂ reveals Fe³⁺, equivalent to very strong hole doping. This would mean that T_c increases again beyond the hole-overdoped stoichiometric compounds (K,Rb,Cs)Fe_{2.5+}As₂, which is appealing, but rather unlikely. We rather suggest that superconductivity occurs in the more ordered fractions of the sample indicated in the HRTEM mappings, where the chemical composition is near to, or even exactly NaFe₂As₂.

Even though the crystallinity of the compound is still rather poor, we point out that this material represents the first metastable iron-based superconductor. This can pave the way to new iron-based superconducting materials, which are not accessible by high temperature methods.

8 $\text{Na}(\text{Fe}_{1-y}\text{Co}_y)_2\text{As}_2$ via oxidative deintercalation

8.1 Introduction

Alkali metal 122 compounds are extremely hole doped compared to the 111 (e.g. NaFeAs) or alkaline earth 122 (e.g. BaFe_2As_2) compounds. Stoichiometric NaFe_2As_2 formally possesses Fe^{2+} and Fe^{3+} one half each, whereas NaFeAs exhibits only Fe^{2+} . A sodium 122 compound is only accessible under mild conditions, as described in the previous chapter. Due to the inhomogeneous oxidative deintercalation process the target compound NaFe_2As_2 exhibited a distribution of deficiencies on the sodium as well as on the iron site, being partly even more hole doped than in stoichiometric composition. This hole doped state formally can be reduced by introducing electrons e.g. by substituting Fe with Co in the solid solution $\text{Na}(\text{Fe}_{1-y}\text{Co}_y)_2\text{As}_2$ in order to investigate influences on the physical properties herein.

$\text{Na}(\text{Fe}_{1-y}\text{Co}_y)_2\text{As}_2$ compounds have recently been reported for the first time in literature by using our synthesis method for $\text{Na}_{1-x}\text{Fe}_{2-y}\text{As}_2$.^[10, 120] No superconductivity was observed.

8.2 Synthesis

Polycrystalline $\text{Na}(\text{Fe}_{1-y}\text{Co}_y)_2\text{As}_2$ ($y = 0.025\text{-}0.2$) was synthesized from precursor $\text{NaFe}_{1-y}\text{Co}_y\text{As}$, which was described in Chapter 6. A solution of iodine (1.6 eq) in tetrahydrofuran (THF) was slowly added to $\text{NaFe}_{1-y}\text{Co}_y\text{As}$ suspended in dry THF and the reaction mixture was stirred at room temperature for 40 h in order to receive $\text{Na}(\text{Fe}_{1-y}\text{Co}_y)_2\text{As}_2$. The solid was allowed to settle, washed twice with THF and dried *in vacuo*. As reaction products, very fine, dark gray powders with metallic luster, sensitive to air, were obtained.

8.3 Crystal structure

The structure and composition of $\text{Na}(\text{Fe}_{1-y}\text{Co}_y)_2\text{As}_2$ compounds were investigated by X-ray powder diffraction with Rietveld refinements (Figure 8.1, Table 8.1) and EDX measurements (Table 8.2). Like $\text{Na}_{1-x}\text{Fe}_{2-y}\text{As}_2$ the Co-doped samples also crystallized

in space group *I4/mmm* and showed broad peaks in consequence of very small sizes of coherently scattering domains along with a sodium and iron distribution. With increasing Co content the *a*-axis slightly increases by 0.26 %, while the *c*-axis decreases by 5.6 % (Figure 8.1). Due to the more significant change of the *c*-axis the cell volume overall decreases by 2.73 %.

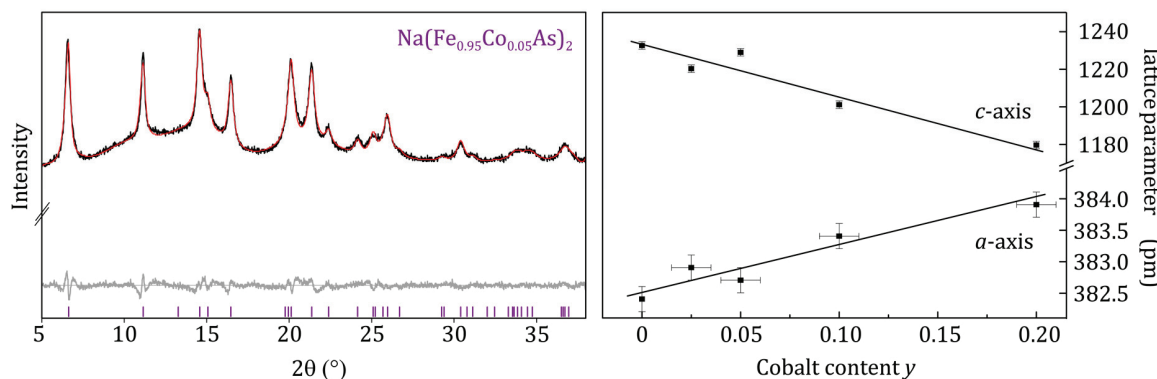


Figure 8.1 Left: Observed (black) and calculated (red) powder X-ray diffraction pattern together with the difference profiles (gray) of the Rietveld refinements of Na(Fe_{0.95}Co_{0.05})₂As₂. Peak positions are marked by vertical lines. Right: Lattice parameters for Na(Fe_{1-y}Co_y)₂As₂.

EDX measurements revealed a low sodium content ranging from 0.35 to 0.63 instead of the expected amount of 1 equivalent (see Table 6.1). A possible explanation is the inhomogeneous extraction of sodium during the oxidative deintercalation process and/or the rough estimation of sodium by EDX. The Co amounts fit well with the nominal composition, whereas the iron content was found to be lowered. The transition metal site is deficient by about 30 %. Furthermore, the Fe to Co ratio is decreased in 122-type Na(Fe_{1-y}Co_y)₂As₂ compared to 111-type NaFe_{1-y}Co_yAs. This indicates the preferential extraction of Fe rather than Co atoms. Probably Fe²⁺ can be oxidized easier than Co²⁺ in this case. Thus, a higher substitution level than predefined by the precursor might be present in the Na_{1-x}(Fe_{1-y}Co_y)₂As₂ samples.

Table 8.1 Atomic coordinates, Wyckoff symbols, isotropic displacement parameters U_{iso} (\AA^2) and occupancies of Na_{1-x}(Fe_{1-y}Co_y)₂As₂, space group $I4/mmm$, $Z = 2$.

atom	Wyckoff	x	y	z	U_{iso}	occ.
<i>y = 0^a</i>						
Na	2a	0	0	0	0.02(1)b	0.95(3)
Fe	4d	0	½	¼	0.020(6)	0.83(1)
As	4e	0	0	0.363(1)	0.038(5)	1
<i>y = 0.025^b</i>						
Na	2a	0	0	0	0.01(1)	1.00(5)
Fe/Co	4d	0	½	¼	0.03(1)	0.84(2)
As	4e	0	0	0.3612(8)	0.025(7)	1
<i>y = 0.05^c</i>						
Na	2a	0	0	0	0.02(1)	1.00(3)
Fe/Co	4d	0	½	¼	0.037(4)	0.87(1)
As	4e	0	0	0.3605(4)	0.046(3)	1
<i>y = 0.1^d</i>						
Na	2a	0	0	0	0.02(1)	0.99(3)
Fe/Co	4d	0	½	¼	0.037(6)	0.80(2)
As	4e	0	0	0.3624(6)	0.058(5)	1
<i>y = 0.2^e</i>						
Na	2a	0	0	0	0.01(1)	1.00(3)
Fe/Co	4d	0	½	¼	0.017(6)	0.80(2)
As	4e	0	0	0.3639(5)	0.044(5)	1

^a $R_{\text{wp}} = 1.216$, $R_p = 0.975$, $\chi^2 = 1.071$, $R_{\text{Bragg}} = 0.099$;^b $R_{\text{wp}} = 0.880$, $R_p = 0.688$, $\chi^2 = 1.935$, $R_{\text{Bragg}} = 0.203$;^c $R_{\text{wp}} = 1.056$, $R_p = 0.798$, $\chi^2 = 2.852$, $R_{\text{Bragg}} = 0.180$;^d $R_{\text{wp}} = 0.796$, $R_p = 0.623$, $\chi^2 = 1.605$, $R_{\text{Bragg}} = 0.137$;^e $R_{\text{wp}} = 0.788$, $R_p = 0.622$, $\chi^2 = 1.917$, $R_{\text{Bragg}} = 0.150$

Table 8.2 Composition of $\text{Na}_{1-x}(\text{Fe}_{1-y}\text{Co}_y)_2\text{As}_2$ as determined by EDX measurements, normalized to As together with the occupancy of the TM site (Fe+Co), the Fe : Co ratio of the "122" and the precursor 111-compounds.

Nominal composition	Measured composition	TM site	Fe : Co ratio (122-type)	Fe : Co ratio (111-type)
$\text{Na}(\text{Fe}_{0.975}\text{Co}_{0.025})_2\text{As}_2$	$\text{Na}_{0.35}(\text{Fe}_{0.69}\text{Co}_{0.03})_2\text{As}_2$	0.72	0.96 : 0.04	0.98 : 0.02
$\text{Na}(\text{Fe}_{0.95}\text{Co}_{0.05})_2\text{As}_2$	$\text{Na}_{0.63}(\text{Fe}_{0.67}\text{Co}_{0.05})_2\text{As}_2$	0.72	0.94 : 0.06	0.96 : 0.04
$\text{Na}(\text{Fe}_{0.93}\text{Co}_{0.07})_2\text{As}_2$	$\text{Na}_{0.45}(\text{Fe}_{0.60}\text{Co}_{0.10})_2\text{As}_2$	0.70	0.86 : 0.13	0.95 : 0.05
$\text{Na}(\text{Fe}_{0.90}\text{Co}_{0.10})_2\text{As}_2$	$\text{Na}_{0.36}(\text{Fe}_{0.58}\text{Co}_{0.11})_2\text{As}_2$	0.69	0.85 : 0.15	0.92 : 0.08
$\text{Na}(\text{Fe}_{0.85}\text{Co}_{0.15})_2\text{As}_2$	$\text{Na}_{0.47}(\text{Fe}_{0.55}\text{Co}_{0.18})_2\text{As}_2$	0.73	0.75 : 0.25	0.88 : 0.12
$\text{Na}(\text{Fe}_{0.80}\text{Co}_{0.20})_2\text{As}_2$	$\text{Na}_{0.51}(\text{Fe}_{0.50}\text{Co}_{0.21})_2\text{As}_2$	0.71	0.71 : 0.29	0.84 : 0.16

8.4 Magnetic measurements

The magnetic properties of $\text{Na}(\text{Fe}_{1-y}\text{Co}_y)_2\text{As}_2$ determined by AC susceptibilities are represented in Figure 8.2. For $y = 0.025$ a weak superconducting transition was found at approximately 10 K, but shifted to higher susceptibility values due to a presumed ferromagnetic impurity (e.g. Fe from the precursor), causing the broad hump. The sample with $y = 0.05$ is superconducting below 10 K with a shielding fraction of 20 %. This transition strongly deviates from the one of precursor $\text{NaFe}_{0.95}\text{Co}_{0.05}\text{As}$ ($T_c = 21$ K). Hence, Co substitution on the Fe site up to 5 % result in transition temperatures comparable to those in $\text{Na}_{1-x}\text{Fe}_{2-y}\text{As}_2$.

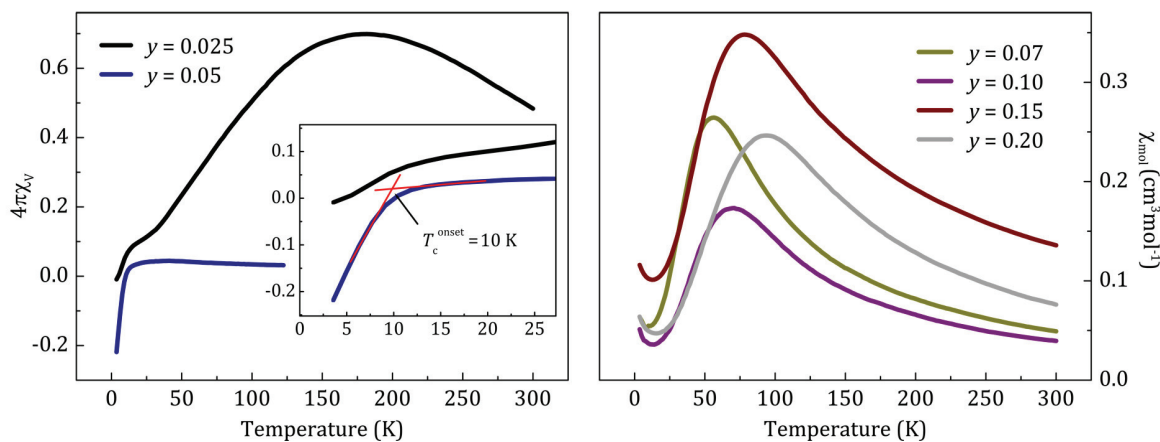


Figure 8.2 AC susceptibilities of $\text{Na}(\text{Fe}_{1-y}\text{Co}_y)_2\text{As}_2$. $y = 0.025$ and 0.05 (left), low temperature region enlarged (inset) and $y = 0.07, 0.10, 0.15, 0.20$ (right).

Samples with higher Co contents did not indicate superconductivity, but exhibited similar curve shapes. With decreasing temperature the susceptibility initially increased, followed by a decrease with a small upturn at low temperatures. With

increasing Co content the maximum of the curves shifted to higher temperatures. This behavior is assumed to be attributed to antiferromagnetic coupling (e.g. SDW scenario). At low temperatures ferromagnetic ordering may occur, indicated by a less distinctive upturn.

A susceptibility measurement of Na(Fe_{0.93}Co_{0.07})₂As₂ performed under zero field cooled (zfc) and field cooled (fc) conditions showed that only the zfc branch decreases below 50 K, while the fc part further increases after splitting of the curves around 65 K (Figure 8.3, left). An isothermal magnetization measurement at 300 K exhibited only a small discontinuity at low fields without the appearance of a hysteresis, indicative for e.g. small amounts of a magnetic impurity. At 1.8 K a small hysteresis opened and the maximum value ($0.15 \mu/\mu_B$) at high fields remained small.

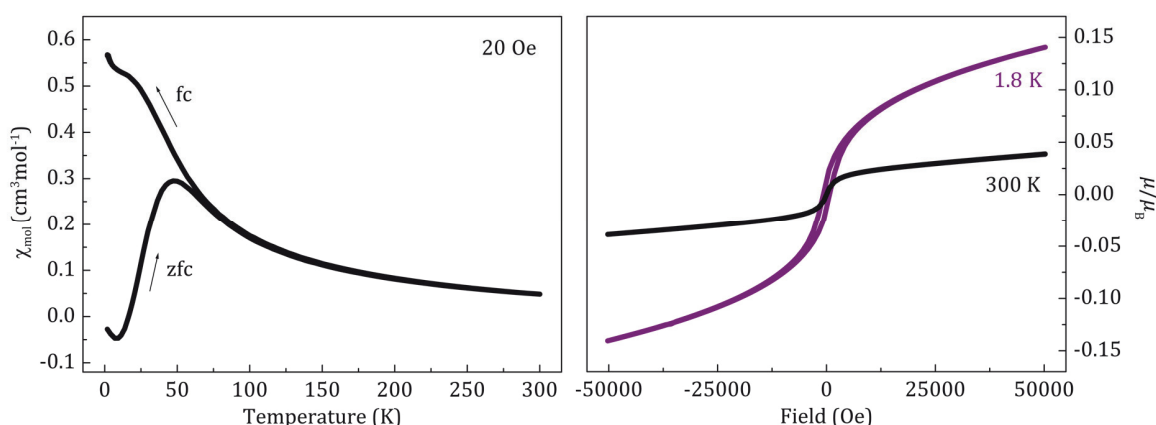


Figure 8.3 Magnetic susceptibility (zfc/fc) of Na(Fe_{0.93}Co_{0.07})₂As₂ with an applied field of 20 Oe (left) and with higher fields (fc) (inset). Isothermal magnetization at 300 K (red curve) and 1.8 K (blue curve) of Na(Fe_{0.93}Co_{0.07})₂As₂.

8.5 Electrical resistivity

The resistivity of Na(Fe_{0.8}Co_{0.2})₂As₂ is almost temperature independent. The relative resistivity overall increased but only by a factor of 1.37 at 3.5 K relative to the value at 300 K. The increase becomes steeper around 30 K. The specific resistivity at 300 K is $7.6 \cdot 10^{-5} \Omega\text{m}$ and therefore characteristic for poor metal conductors. However, the resistivity slightly increased instead of decreasing with lower temperatures as expected for metallic behavior.

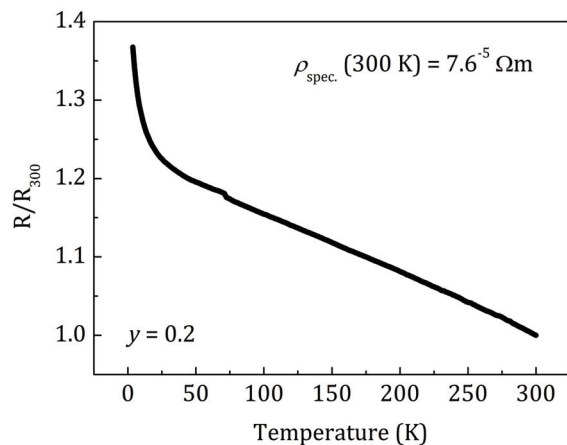


Figure 8.4 Relative resistivity of $\text{Na}(\text{Fe}_{0.8}\text{Co}_{0.2})_2\text{As}_2$.

8.6 Conclusion

$\text{Na}_{1-x}((\text{Fe}_{1-y}\text{Co}_y)_{1-z}\text{As})_2$ samples were successfully synthesized from $\text{NaFe}_{1-y}\text{Co}_y\text{As}$ precursors via an oxidative deintercalation. Hence, the strongly hole doped state of $\text{Na}_{1-x}\text{Fe}_{2-y}\text{As}_2$ could formally and partly be compensated by electron doping with Co on the Fe site. Whereas all 111 precursor ($y = 0 - 0.2$) are superconducting, this property is suppressed in most of the Co-doped 122 compounds. Samples with low Co quantities ($y = 0.025, 0.05$) revealed superconductivity below 10 K, comparable to $\text{Na}_{1-x}\text{Fe}_{2-y}\text{As}_2$. Although the unfavorable strongly hole doped state is increasingly compensated for higher substitution levels, no superconductivity occurred for $y > 0.05$. Instead, AFM ordering presumably appears. Superconductivity below 11 K in $\text{Na}_{1-x}\text{Fe}_{2-y}\text{As}_2$ is rather unexpected, due to the strong hole doped state. However, electron doping with Co cannot stabilize the superconducting state but instead suppresses superconductivity for $y > 0.05$. The direct manipulation within the superconducting sheets by Co substitution, along with the vacancy quantity might be the reason for the absence of superconductivity.

9 Summary

This thesis comprises synthesis routes under mild conditions in the scope of iron-based superconductors. The main focus lay on syntheses covering metathesis reactions as well as reductive intercalation and oxidative deintercalation processes which were either solvent-assisted or due to O₂-annealing effects. The obtained compounds were investigated concerning their structural, magnetic and electrical properties. The work presented in this thesis is summarized below.

FeSe

Tetragonal FeSe was successfully synthesized via a metathesis reaction at room temperature in THF. Contrary to solid state synthesis, this method avoids the formation of the hexagonal α -phase. The compound exhibited disorder accompanied by Se vacancies, indicated by XRPD and ⁵⁷Fe-Mössbauer spectroscopy. Electrical resistivity indicated Mott insulating properties. At low temperatures, large fractions of FeSe ordered magnetically, contrary to conventional FeSe, which is a nonmagnetic 8 K superconductor. Upon annealing, FeSe became more homogeneous and less magnetic. Most likely, FeSe orders antiferromagnetically below 50 K in agreement with recent literature results.^[50] Herein, oxygen or H₂O incorporation was considered to be responsible for this behavior. In future studies, this interesting new aspect should be investigated in more detail, since it seems to crucially influence the physical properties of FeSe, obtained under mild conditions. By using Li₂S or Li₂Te the metathesis reaction might also be adapted to synthesize tetragonal FeS and FeTe, which in turn might act as interesting starting materials to obtain new Fe-based superconductors.

Fe_{1+x}Te_{1-y}Se_y

Fe_{1+x}Te_{1-y}Se_y ($x = 0\text{--}0.1$, $y = 0.1\text{--}0.4$) samples were O₂- and subsequently H₂-annealed in order to investigate influences on superconductivity. FeTe_{1-y}Se_y samples show weak to bulk superconductivity depending on Se concentrations, while Fe_{1.1}Te_{1-y}Se_y samples lack superconducting properties. After O₂-annealing, all samples exhibited bulk superconductivity. The process is irreversible by hydrogen-annealing. Magnetic measurements revealed small fractions of magnetic Fe₃O₄ and/or γ -Fe₂O₃ due to

deintercalation of interstitial iron atoms. This heterogeneous process starts at the surface and likely causes inhomogeneous particles along with FeTe₂ impurity formation. Thus the *anti-PbO*-type phase obviously rather degrades when iron is extracted from within the layers, than to form iron-deficient layers like in K_{1-x}Fe_{2-y}Se₂^[86, 87] or in Na_{1-x}Fe_{2-y}As₂ as described in chapters 5, 7 and 8.

K_{1-x}Fe_{2-y}Se₂

K_{1-x}Fe_{2-y}Se₂ was successfully synthesized from FeSe via reductive intercalations, using a variety of K containing organic reducing agents. Potassium intercalated FeSe crystallized in an imperfect $\sqrt{5} \times \sqrt{5}$ Fe vacancy ordered 245-type phase due to deviation from a K_{0.8}Fe_{1.6}Fe₂ (or K₂Fe₄Se₅) stoichiometry and disorder. Upon annealing the amount of K_{1-x}Fe_{2-y}Se₂ increased along with a more pronounced crystallinity, while the remaining FeSe fraction decreases. The obtained phases were significantly iron deficient (~20%) whereby elemental iron appears as magnetic impurity. Indications for superconducting transitions were found at 20 and 12 K. These values clearly deviate from T_{cs} of FeSe (8 K) or solid state synthesized K_{1-x}Fe_{2-y}Se₂ (32 K). Thus, these mild reductive intercalation routes offer the opportunity to receive new phases with superconducting properties within the K-Fe-Se system.

Furthermore, this method is applicable universally to intercalate other metals, like alkaline or alkaline earth metals, into layered *anti-PbO*-type FeChs. For example EA₂I₂ can serve as EA metal source for producing Rieke-metals, which *in situ* can be reduced to highly dispersed EA⁰ with e.g. Alkaline metal/organic species.

NaFe_{1-y}Co_yAs

NaFe_{1-y}Co_yAs samples with a homogeneous Co distribution were synthesized from Fe_{1-y}Co_yAs as precursor. Bulk superconductivity was found for $y = 0.025\text{-}0.1$ with a constant T_c of 21 K. An inhomogeneous cobalt distribution with fractions of ideally doped NaFe_{1-y}Co_yAs in each sample causing the constant onset of T_c at 21 K could be excluded. In addition, deficiencies on the Na site, caused by air-exposure, can increase the T_c in NaFeAs and were investigated as reason for the constant T_c . However, air conducted NaFe_{1-y}Co_yAs did not exhibit superconductivity. Hence, the reason for the

unaltered T_c could not readily be determined by common analytical methods. Further detailed investigations of e.g. the local structure and/or a very accurate determination of the Na content might reveal the actual origin.

Na_{1-x}Fe_{2-y}As₂

Na_{1-x}Fe_{2-y}As₂ was synthesized via an oxidative deintercalation reaction with iodine in THF. The metastable, poorly crystalline compound has a deficient ThCr₂Si₂-type structure with a mean composition of Na_{0.9(2)}Fe_{1.7(2)}As₂. Electron microscopy detected well crystalline and strongly distorted areas associated with a significant disorder of sodium in agreement with ²³Na-NMR data. The latter are probably a consequence of the heterogeneous solid/liquid reaction at low temperature. The compound is an 11 K superconductor with a shielding fraction of 20%. Electron counting reveals Fe³⁺ in Na_{~1}⁺Fe_{1.67}³⁺As₂ which is far beyond the already strongly hole-overdoped stoichiometric compounds (K,Rb,Cs)Fe_{2.5+}As₂. Due to the T_c , which is about three times higher than those of the higher homologues (K, 3.8 K; Rb and Cs, 2.6 K), superconductivity presumably occurs in the more ordered fractions of the sample where the chemical composition is near to, or even exactly NaFe₂As₂. Na_{1-x}Fe_{2-y}As₂ represents the first metastable iron-based superconductor. This can pave the way to new iron-based superconducting materials, which are not accessible by high temperature methods.

Na_{1-x}((Fe_{1-y}Co_y)_{1-z}As)₂

Na_{1-x}((Fe_{1-y}Co_y)_{1-z}As)₂ samples were successfully synthesized from NaFe_{1-y}Co_yAs precursors via an oxidative deintercalation with iodine in THF at room temperature. Like Na_{1-x}Fe_{2-y}As₂ the compounds are cation deficient, rather poorly crystalline and adopt the ThCr₂Si₂-type structure. Samples with low Co quantities ($y = 0.025, 0.05$) revealed superconductivity below 10 K, comparable to Na_{1-y}Fe_{2-x}As₂. Although the unfavorable strongly hole doped state is increasingly compensated for higher substitution levels, no superconductivity occurred for $y > 0.05$. Instead, AFM ordering was indicated. The direct manipulation within the superconducting sheets by Co substitution, along with the vacancy quantity are possible reasons for the absence of superconductivity.

Conclusion

This thesis provides new soft chemistry approaches to Fe-based superconductors. Mild syntheses were demonstrated to be able to overcome difficulties, occurring in conventional synthesis and to enable the access to new metastable phases.

A solvent-based metathesis reaction led to β -FeSe exclusively. Contrary to solid state syntheses, the formation of hexagonal α -FeSe could be avoided under mild conditions. The deintercalation of interstitial Fe (by formation of Fe_3O_4) could be proven by low temperature O_2 -annealing of $\text{Fe}_{1+x}\text{Te}_{1-y}\text{Se}_y$. By using redox (de)intercalations $\text{K}_{1-x}\text{Fe}_{2-y}\text{Se}_2$, metastable $\text{Na}_{1-x}\text{Fe}_{2-y}\text{As}_2$ and $\text{Na}_{1-x}((\text{Fe}_{1-y}\text{Co}_y)_{1-z}\text{As})_2$ could successfully be obtained at room temperature. The mild synthesis conditions led to compounds like FeSe and $\text{K}_{1-x}\text{Fe}_{2-y}\text{Se}_2$ which exhibited different physical properties than found by conventional high temperature methods.

In general, the developed (de)intercalation reactions represent a new, universally applicable tool in order to manipulate the structure along with the properties of Fe-based superconductors. The basic structural features of the characteristic $\text{FeX}_{4/4}$ tetrahedral layers, however, are preserved. A schematic representation of the structural relationship of the investigated compounds is depicted in Figure 9.1.

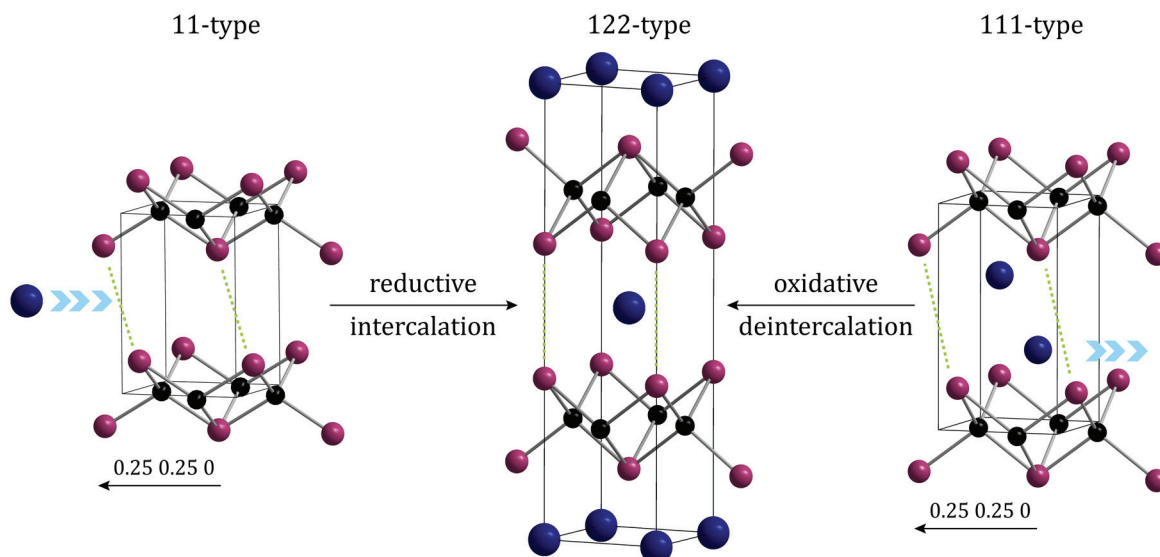


Figure 9.1 Schematic representation of the structural relationship between 11-, 122- and 111-type Fe-based compounds upon reductive intercalation and oxidative deintercalation reactions. Black spheres represent Fe, purple ones pnictide or chalcogenide and blue ones e.g. alkaline metals.

Soft chemistry syntheses have been shown to allow the formation of a variety of phases, like $\text{Na}_{1-x}\text{Fe}_{2-y}\text{As}_2$, $\text{Na}_{1-x}[(\text{Fe}_{1-y}\text{Co}_y)_{1-z}\text{As}]_2$ and $\text{K}_{1-x}\text{Fe}_{2-y}\text{Se}_2$. Hence, especially low temperature approaches may enable the realization of complex stacking sequences, potentially leading to the fulfillment of the greatest goal in the research of superconductors – room temperature superconductivity.

Abbreviations

2θ	diffraction angle
<i>a b c</i>	lattice constants
acac	acetyl acetonate
Å	Ångström
<i>a</i>	anti (concerning crystal structures)
<i>A</i>	alkaline metals
AC	alternating current
<i>Ae</i>	alkaline earth metals
AFM	antiferromagnetic
BCS	Bardeen-Cooper-Schrieffer, names of the inventors of BCS-theory
CCD	charge coupled device
<i>Ch</i>	chalcogenide
CS	center shift
DFT	density functional theory
EDX	energy dispersive X-ray analysis
eq	equivalent
fc	field cooled (part of the susceptibility)
FWHM	full width at half maximum
h	hours
<i>H</i>	magnetic field
<i>H</i> _{c1}	lower critical magnetic field
<i>H</i> _{c2}	upper critical magnetic field
HRTEM	high resolution transmission electron microscopy
<i>I</i>	body centered (concerning crystal structures)
K	Kelvin
<i>m</i>	mirror plane
MAS	magic angle spinning
MBE	molecular beam epitaxy
MEM	maximum entropy method

min	minutes
MPMS	magnetic property measurement system
<i>n</i>	glide mirror plane
nm	nanometer
NMR	nuclear magnetic resonance
O2	origin choice 2 – representation of a unit cell
occ.	occupancies of atomic sites
Oe	Ørsted (magnetic unit)
<i>P</i>	primitive (concerning crystal structures)
PED	precession electron diffraction
<i>Pn</i>	Pnictide
XRPD	X-ray powder diffraction
<i>R</i> ...	residual factor
<i>RE</i>	rare earth metal
S	Siemens
SAED	selected area electron diffraction
SDW	spin density wave
SEM	scanning electron microscopy
SQUID	superconducting quantum interference device
SSM	solid state metathesis
<i>T</i> c	superconducting transition
<i>T</i> C	Curie temperature
<i>T</i> N	Néel temperature
TEM	transmission electron microscopy
THF	tetrahydrofuran
U	displacement parameter
VRH	variable range hopping
Vzz	main component of the electric field gradient tensor (Mössbauer)
<i>z</i>	atomic coordinate
zfc	zero field cooled (part of the susceptibility)
μSR	muon spin relaxation
μB	Bohr magneton

Abbreviations

χ^2	goodness of fit
χ_v	magnetic susceptibility per volume
χ_{mol}	magnetic susceptibility per mole
δ	isomer shift (Mössbauer)
ΔE_Q	quadrupole splitting parameter (Mössbauer)
Γ	experimental line width (Mössbauer)
λ	wavelength

Bibliography

- [1] H. J. Meyer, *Dalton Transactions* **2010**, *39*, 5973.
- [2] P. R. Bonneau, R. F. Jarvis, R. B. Kaner, *Nature* **1991**, *349*, 510.
- [3] M. J. McKelvy, M. S. Glaunsinger, *Annual Review of Physical Chemistry* **1990**, *41*, 497.
- [4] R. Schöllhorn, *Comments on Inorganic Chemistry* **1983**, *2*, 271.
- [5] J. G. Bednorz, K. A. Müller, *Zeitschrift für Physik B* **1986**, *64*, 189.
- [6] Y. Ohta, T. Tohyama, S. Maekawa, *Physical Review Letters* **1991**, *66*, 1228.
- [7] C. d. l. Cruz, Q. Huang, J. W. Lynn, J. Li, W. Ratcliff(II), J. L. Zarestky, H. A. Mook, G. F. Chen, J. L. Luo, N. L. Wang, P. Dai, *Nature* **2008**, *453*, 899.
- [8] H. Hiramatsu, T. Katase, T. Kamiya, M. Hirano, H. Hosono, *Applied Physics Letters* **2008**, *93*, 162504.
- [9] H. Hiramatsu, T. Katase, T. Kamiya, M. Hirano, H. Hosono, *Applied Physics Express* **2008**, *1*, 101702.
- [10] G. M. Friederichs, I. Schellenberg, R. Pöttgen, V. Duppel, L. Kienle, J. S. auf der Günne, D. Johrendt, *Inorganic Chemistry* **2012**, *51*, 8161.
- [11] Y. Kamihara, T. Watanabe, M. Hirano, H. Hosono, *Journal of the American Chemical Society* **2008**, *130*, 3296.
- [12] F. Hummel, Y. Su, A. Senyshyn, D. Johrendt, *Physical Review B* **2013**, *88*, 144517.
- [13] C. Löhnert, T. Stürzer, M. Tegel, R. Frankovsky, G. Friederichs, D. Johrendt, *Angewandte Chemie International Edition* **2011**, *50*, 9195.
- [14] Y. Kawasaki, K. Deguchi, S. Demura, T. Watanabe, H. Okazaki, T. Ozaki, T. Yamaguchi, H. Takeya, Y. Takano, *Solid State Communications* **2012**, *152*, 1135.
- [15] 5.0 build 2 ed., HUBER.
- [16] D. STOE & Cie GmbH, 2.12 ed. (Ed.: D. STOE & Cie GmbH), STOE & Cie GmbH, Darmstadt, STOE & Cie GmbH, Darmstadt, **2005**.
- [17] A. Coelho, *TOPAS-Academic*, v. 4.1, Coelho Software, Brisbane, **2007**.
- [18] INCA, v. 4.02, Oxford Instruments, Analytical Limited, **1998-2002**.

- [19] *SmartSEM*, v. Version 5.07 Beta, Carl Zeiss Microscopy Ltd., **2014**.
- [20] *QUANTAX 200*, v. Version 1.9.4.3448, Bruker Nano GmbH, **2013**.
- [21] *MPMS MultiVU*, v. 1.56 Build 72, Quantum Design Inc., San Diego, **2005**.
- [22] M. Tegel, *Iron pnictide superconductors*, dissertation thesis, LMU (München), **2011**.
- [23] N. F. Mott, *Philosophical Magazine* **1969**, *19*, 835.
- [24] J. M. Marshall, C. Main, *Journal of Physics* **2008**, *20*, 285210.
- [25] R. A. Brand, *Normos Mössbauer Fitting Program* **2002**.
- [26] P. Jeitschko, A. Simon, R. Ramlau, H. Mattausch, *Zeitschrift fuer Anorganische und Allgemeine Chemie* **1997**, *623*, 1447.
- [27] P. Jeitschko, A. Simon, R. Ramlau, H. Mattausch, *European Journal of Microscopy and Microanalysis* **1997**, *46*, 21.
- [28] A. Stadelmann, *Ultramicroscopy* **1987**, *21*, 131.
- [29] G. Hagg, A. L. Kindstrom, *Zeitschrift für Physikalische Chemie B* **1933**, *22*, 453.
- [30] F. Hsu, J. Luo, K. Yeh, T. Chen, T. Huang, P. Wu, Y. Lee, Y. Huang, Y. Chu, D. Yan, M. Wu, *Proceedings of the National Academy of Sciences* **2008**, *105*, 14262.
- [31] T. J. Liu, J. Hu, B. Qian, D. Fobes, Z. Q. Mao, W. Bao, M. Reehuis, S. A. J. Kimber, K. Prokeš, S. Matas, D. N. Argyriou, A. Hiess, A. Rotaru, H. Pham, L. Spinu, Y. Qiu, V. Thampy, A. T. Savici, J. A. Rodriguez, C. Broholm, *Nature Materials* **2010**, *9*, 718.
- [32] M. J. Han, S. Y. Savrasov, *Physical Review Letters* **2009**, *103*, 067001.
- [33] H. Okamoto, *Journal of Phase Equilibria* **1991**, *12*, 383.
- [34] A. J. Williams, T. M. McQueen, R. J. Cava, *Solid State Communications* **2009**, *149*, 1507.
- [35] T. M. McQueen, Q. Huang, V. Ksenofontov, C. Felser, Q. Xu, H. Zandbergen, Y. S. Hor, J. Allred, A. J. Williams, D. Qu, J. Checkelsky, N. P. Ong, R. J. Cava, *Physical Review B* **2009**, *79*, 014522.
- [36] S. Medvedev, T. M. McQueen, I. A. Troyan, T. Palasyuk, M. I. Eremets, R. J. Cava, S. Naghavi, F. Casper, V. Ksenofontov, G. Wortmann, C. Felser, *Nature Materials* **2009**, *8*, 630.

- [37] M. Burrard-Lucas, D. G. Free, S. J. Sedlmaier, J. D. Wright, S. J. Cassidy, Y. Hara, A. J. Corkett, T. Lancaster, P. J. Baker, S. J. Blundell, S. J. Clarke, *Nature Materials* **2013**, *12*, 15.
- [38] U. Pachmayr, F. Nitsche, H. Luetkens, S. Kamusella, F. Brückner, R. Sarkar, H.-H. Klauss, D. Johrendt, *Angewandte Chemie International Edition* **2015**, *54*, 293.
- [39] U. Pachmayr, D. Johrendt, *Chemical Communications* **2015**, *51*, 4689.
- [40] D. Liu, W. Zhang, D. Mou, J. He, Y.-B. Ou, Q.-Y. Wang, Z. Li, L. Wang, L. Zhao, S. He, Y. Peng, X. Liu, C. Chen, L. Yu, G. Liu, X. Dong, J. Zhang, C. Chen, Z. Xu, J. Hu, X. Chen, X. Ma, Q. Xue, X. J. Zhou, *Nature Communications* **2012**, *3*, 931.
- [41] S. He, J. He, W. Zhang, L. Zhao, D. Liu, X. Liu, D. Mou, Y.-B. Ou, Q.-Y. Wang, Z. Li, L. Wang, Y. Peng, Y. Liu, C. Chen, L. Yu, G. Liu, X. Dong, J. Zhang, C. Chen, Z. Xu, X. Chen, X. Ma, Q. Xue, X. J. Zhou, *Nature Materials* **2013**, *12*, 605.
- [42] J.-F. Ge, Z.-L. Liu, C. Liu, C.-L. Gao, D. Qian, Q.-K. Xue, Y. Liu, J.-F. Jia, *Nature Materials* **2015**, *14*, 285.
- [43] C.-C. Chang, C.-H. Wang, M.-H. Wen, Y.-R. Wu, Y.-T. Hsieh, M.-K. Wu, *Solid State Communications* **2012**, *152*, 649.
- [44] K. D. Oyler, X. L. Ke, I. T. Sines, P. Schiffer, R. E. Schaak, *Chemistry of Materials* **2009**, *21*, 3655.
- [45] L. Q. Chen, H. Q. Zhan, X. F. Yang, Z. Y. Sun, J. Zhang, D. Xu, C. L. Liang, M. M. Wu, J. Y. Fang, *CrystEngComm* **2010**, *12*, 4386.
- [46] L. Q. Chen, X. F. Yang, X. H. Fu, C. M. Wang, C. L. Liang, M. M. Wu, *European Journal of Inorganic Chemistry* **2011**, 2098.
- [47] S. J. Li, D. Li, J. J. Jiang, G. B. Liu, S. Ma, W. Liu, Z. D. Zhang, *Journal of Applied Physics* **2014**, *115*, 17B502.
- [48] X. Mao, J. G. Kim, J. Han, H. S. Jung, S. G. Lee, N. A. Kotov, J. Lee, *Journal of the American Chemical Society* **2014**, *136*, 7189.
- [49] F. Nitsche, T. Goltz, H. H. Klauss, A. Isaeva, U. Muller, W. Schnelle, P. Simon, T. Doert, M. Ruck, *Inorganic Chemistry* **2012**, *51*, 7370.
- [50] J. T. Greenfield, S. Kamali, K. Lee, K. Kovnir, *Chemistry of Materials* **2015**, *27*, 588.
- [51] T.-K. Chen, C.-C. Chang, H.-H. Chang, A.-H. Fang, C.-H. Wang, W.-H. Chao, C.-M. Tseng, Y.-C. Lee, Y.-R. Wu, M.-H. Wen, H.-Y. Tang, F.-R. Chen, M.-J. Wang, M.-K. Wu, D. Van Dyck, *Proceedings of the National Academy of Sciences* **2014**, *111*, 63.

- [52] D. P. Thompson, P. Boudjouk, *Journal of Organic Chemistry* **1987**, *53*, 2109.
- [53] R. Peng, H. C. Xu, S. Y. Tan, H. Y. Cao, M. Xia, X. P. Shen, Z. C. Huang, C. H. P. Wen, Q. Song, T. Zhang, B. P. Xie, X. G. Gong, D. L. Feng, *Nature Communications* **2014**, *5*.
- [54] F. C. Hsu, J. Y. Luo, K. W. Yeh, T. K. Chen, T. W. Huang, P. M. Wu, Y. C. Lee, Y. L. Huang, Y. Y. Chu, D. C. Yan, M. K. Wu, *Proceedings of the National Academy of Sciences* **2008**, *105*, 14262.
- [55] M. K. Wu, F. C. Hsu, K. W. Yeh, T. W. Huang, J. Y. Luo, M. J. Wang, H. H. Chang, T. K. Chen, S. M. Rao, B. H. Mok, C. L. Chen, Y. L. Huang, C. T. Ke, P. M. Wu, A. M. Chang, C. T. Wu, T. P. Perng, *Physica C: Superconductivity*, *469*, 340.
- [56] M. C. Ding, H. Q. Lin, Y. Z. Zhang, *Low Temperature Physics* **2014**, *40*, 113.
- [57] A. S. Sefat, *Current Opinion in Solid State and Materials Science* **2013**, *17*, 59.
- [58] R. T. Gordon, H. Kim, N. Salovich, R. W. Giannetta, R. M. Fernandes, V. G. Kogan, T. Prozorov, S. L. Bud'ko, P. C. Canfield, M. A. Tanatar, R. Prozorov, *Physical Review B* **2010**, *82*, 054507.
- [59] R. Khasanov, K. Conder, E. Pomjakushina, A. Amato, C. Baines, Z. Bukowski, J. Karpinski, S. Katrych, H. H. Klauss, H. Luetkens, A. Shengelaya, N. D. Zhigadlo, *Physical Review B* **2008**, *78*, 220510.
- [60] R. Hu, H. Lei, M. Abeykoon, E. S. Bozin, S. J. L. Billinge, J. B. Warren, T. Siegrist, C. Petrovic, *Physical Review B* **2011**, *83*, 224502.
- [61] M. H. Fang, H. M. Pham, B. Qian, T. J. Liu, E. K. Vehstedt, Y. Liu, L. Spinu, Z. Q. Mao, *Physical Review B* **2008**, *78*, 224503.
- [62] A. Sklyarova, G. C. Tewari, J. Linden, E. L. Rautama, M. Karppinen, *Journal of Magnetism and Magnetic Materials* **2014**, *357*, 82.
- [63] S. Staniland, W. Williams, N. Telling, L. Van Der, A. Harrison, B. Ward, *Nature Nanotechnology* **2008**, *3*, 158.
- [64] A. Blachowski, K. Ruebenbauer, J. Zukrowski, J. Przewoznik, K. Wojciechowski, Z. M. Stadnik, *Journal of Alloys and Compounds* **2010**, *494*, 1.
- [65] A. K. Dutta, S. K. Maji, D. N. Srivastava, A. Mondal, P. Biswas, P. Paul, B. Adhikary, *Applied Materials and Interfaces* **2012**, *4*, 1919.
- [66] S. Borisenko, *Nature Materials* **2013**, *12*, 600.
- [67] Y. Mizuguchi, Y. Takano, *Zeitschrift für Kristallographie* **2011**, *226*, 417.

- [68] E. E. Rodriguez, P. Zavalij, P.-Y. Hsieh, M. A. Green, *Journal of the American Chemical Society* **2010**, *132*, 10006.
- [69] Y. F. Nie, D. Telesca, J. I. Budnick, B. Sinkovic, B. O. Wells, *Physical Review B* **2010**, *82*, 020508.
- [70] W. Bao, Y. Qiu, Q. Huang, M. A. Green, P. Zajdel, M. R. Fitzsimmons, M. Zhernenkov, S. Chang, M. Fang, B. Qian, E. K. Vehstedt, J. Yang, H. M. Pham, L. Spinu, Z. Q. Mao, *Physical Review Letters* **2009**, *102*, 247001.
- [71] B. C. Sales, A. S. Sefat, M. A. McGuire, R. Y. Jin, D. Mandrus, Y. Mozharivskyj, *Physical Review B* **2009**, *79*, 094521.
- [72] V. P. S. Awana, A. Pal, A. Vajpayee, B. Gahtori, H. Kishan, *Physica C: Superconductivity* **2011**, *471*, 77.
- [73] A. Martinelli, A. Palenzona, M. Tropeano, C. Ferdeghini, M. Putti, M. R. Cimberle, T. D. Nguyen, M. Affronte, C. Ritter, *Physical Review B* **2010**, *81*, 094115.
- [74] A. Sala, A. Palenzona, C. Bernini, F. Caglieris, M. R. Cimberle, C. Ferdeghini, G. Lamura, A. Martinelli, M. Pani, J. Hecher, M. Eisterer, M. Putti, *Journal of Physics* **2014**, *507*, 012044.
- [75] Y. Sun, T. Taen, Y. Tsuchiya, Z. X. Shi, T. Tamegai, *Superconductor Science and Technology* **2013**, *26*, 015015.
- [76] J. Hu, G. C. Wang, B. Qian, Z. Q. Mao, *Superconductor Science and Technology* **2012**, *25*, 084011.
- [77] E. E. Rodriguez, C. Stock, P.-Y. Hsieh, N. P. Butch, J. Paglione, M. A. Green, *Chemical Science* **2011**, *2*, 1782.
- [78] Y. Koshika, T. Usui, S. Adachi, T. Watanabe, K. Sakano, S. Simayi, M. Yoshizawa, *Journal of the Physical Society of Japan* **2012**, *82*, 023703.
- [79] K. Deguchi, A. Yamashita, T. Yamaki, H. Hara, S. Demura, S. J. Denholme, M. Fujioka, H. Okazaki, H. Takeya, T. Yamaguchi, Y. Takano, *Journal of Applied Physics* **2014**, *115*, 053909.
- [80] M. Ohno, T. Kawamata, T. Noji, K. Naruse, Y. Matsuoka, T. Adachi, T. Nishizaki, T. Sasaki, Y. Koike, *Journal of the Physical Society of Japan* **2014**, *83*, 044704.
- [81] Y. Sun, Y. Tsuchiya, T. Taen, T. Yamada, S. Pyon, A. Sugimoto, T. Ekino, Z. Shi, T. Tamegai, *Scientific Reports* **2014**, *4*, 4585.
- [82] M. Tegel, C. Löhnert, D. Johrendt, *Solid State Communications* **2010**, *150*, 383.

- [83] W. Buckel, R. Kleiner, *Supraleitung - Grundlagen und Anwendungen, 6. Auflage*, Wiley-VCH Verlag GmbH &Co. KGaA, Weinheim, **2004**.
- [84] H. Lueken, *Magnetochemie*, Teubner Stuttgart, Leipzig, **1999**.
- [85] T. J. Liu, X. Ke, B. Qian, J. Hu, D. Fobes, E. K. Vehstedt, H. Pham, J. H. Yang, M. H. Fang, L. Spinu, P. Schiffer, Y. Liu, Z. Q. Mao, *Physical Review B* **2009**, *80*, 174509.
- [86] W. Li, H. Ding, P. Deng, K. Chang, C. Song, K. He, L. Wang, X. Ma, J.-P. Hu, X. Chen, Q.-K. Xue, *Nature Physics* **2012**, *8*, 126.
- [87] A. Ricci, N. Poccia, B. Joseph, G. Campi, A. Bianconi, *Journal of Superconductivity and Novel Magnetism* **2012**, *25*, 1383.
- [88] M. Burrard-Lucas, D. G. Free, S. J. Sedlmaier, J. D. Wright, S. J. Cassidy, Y. Hara, A. J. Corkett, T. Lancaster, P. J. Baker, S. J. Blundell, S. J. Clarke, *Nature Materials* **2013**, *12*, 15.
- [89] S. J. Sedlmaier, S. J. Cassidy, R. G. Morris, M. Drakopoulos, C. Reinhard, S. J. Moorhouse, D. O'Hare, P. Manuel, D. Khalyavin, S. J. Clarke, *Journal of the American Chemical Society* **2014**, *136*, 630.
- [90] T. P. Ying, X. L. Chen, G. Wang, S. F. Jin, T. T. Zhou, X. F. Lai, H. Zhang, W. Y. Wang, *Scientific Reports* **2012**, *2*.
- [91] J. Guo, S. Jin, G. Wang, S. Wang, K. Zhu, T. Zhou, M. He, X. Chen, *Physical Review B* **2010**, *82*, 180520.
- [92] S. V. Carr, D. Louca, J. Siewenie, Q. Huang, A. Wang, X. Chen, P. Dai, *Physical Review B* **2014**, *89*, 134509.
- [93] Y. J. Song, Z. Wang, Z. W. Wang, H. L. Shi, Z. Chen, H. F. Tian, G. F. Chen, H. X. Yang, J. Q. Li, *Europhysics Letters* **2011**, *95*, 37007.
- [94] C.-H. Wang, T.-K. Chen, C.-C. Chang, C.-H. Hsu, Y.-C. Lee, M.-J. Wang, P. M. Wu, M.-K. Wu, *arXiv: 1502.01116v2* **2015**.
- [95] W. Bao, *Journal of Physics* **2015**, *27*, 023201.
- [96] N. G. Connelly, W. E. Geiger, *Chemical Reviews* **1996**, *96*, 877.
- [97] G. Gritzner, J. Kuta, *Pure and Applied Chemistry* **1984**, *56*, 461.
- [98] M. Hartmann, Y. Li, A. Studer, *Journal of the American Chemical Society* **2012**, *134*, 16516.
- [99] C. W. Chu, F. Chen, M. Gooch, A. M. Guloy, B. Lorenz, B. Lv, K. Sasnal, Z. J. Tang, J. H. Tapp, Y. Y. Xue, *Physica C: Superconductivity*, *469*, 326.

- [100] S. Li, C. de la Cruz, Q. Huang, G. F. Chen, T. L. Xia, J. L. Luo, N. L. Wang, P. Dai, *Physical Review B* **2009**, *80*, 020504.
- [101] J. B. H. T.-L. Xia, D. M. Wang, G. F. Chen, *arXiv:1001.3311v2* **2010**.
- [102] P. Cai, X. Zhou, W. Ruan, A. Wang, X. Chen, D.-H. Lee, Y. Wang, *Nature Communications* **2013**, *4*, 1596.
- [103] A. F. Wang, X. G. Luo, Y. J. Yan, J. J. Ying, Z. J. Xiang, G. J. Ye, P. Cheng, Z. Y. Li, W. J. Hu, X. H. Chen, *Physical Review B* **2012**, *85*, 224521.
- [104] D. R. Parker, M. J. P. Smith, T. Lancaster, A. J. Steele, I. Franke, P. J. Baker, F. L. Pratt, M. J. Pitcher, S. J. Blundell, S. J. Clarke, *Physical Review Letters* **2010**, *104*, 057007.
- [105] R. Shannon, *Acta Crystallographica Section A* **1976**, *32*, 751.
- [106] D. Bérardan, L. Pinsard-Gaudart, N. Dragoe, *Journal of Alloys and Compounds* **2009**, *481*, 470.
- [107] D. Johrendt, *Journal of Materials Chemistry* **2011**, *21*, 13726.
- [108] D. Johrendt, R. Pöttgen, *Angewandte Chemie, International Edition* **2008**, *47*, 4782.
- [109] D. C. Johnston, *Advanced Physics* **2010**, *59*, 803.
- [110] Y. Kamihara, T. Watanabe, M. Hirano, H. Hosono, *Journal of the American Chemical Society* **2008**, *130*, 3296.
- [111] M. Rotter, M. Tegel, D. Johrendt, *Physical Review Letters* **2008**, *101*, 107006.
- [112] D. R. Parker, M. J. Pitcher, P. J. Baker, I. Franke, T. Lancaster, S. J. Blundell, S. J. Clarke, *Chemical Communications* **2009**, 2189.
- [113] D. Johrendt, H. Hosono, R. D. Hoffmann, R. Pöttgen, *Zeitschrift fuer Kristallographie* **2011**, *226*, 435.
- [114] C. de la Cruz, Q. Huang, J. W. Lynn, J. Y. Li, W. Ratcliff, J. L. Zarestky, H. A. Mook, G. F. Chen, J. L. Luo, N. L. Wang, P. C. Dai, *Nature* **2008**, *453*, 899.
- [115] V. Zinth, T. Dellmann, H. H. Klauss, D. Johrendt, *Angewandte Chemie, International Edition* **2011**, *50*, 7919.
- [116] Z. A. Ren, W. Lu, J. Yang, W. Yi, X. L. Shen, Z. C. Li, G. C. Che, X. L. Dong, L. L. Sun, F. Zhou, Z. X. Zhao, *Chinese Physics Letters* **2008**, *25*, 2215.

- [117] M. Gooch, B. Lv, K. Sasmal, J. H. Tapp, Z. J. Tang, A. M. Guloy, B. Lorenz, C. W. Chu, *Physica C: Superconductivity* **2010**, 470, S276.
- [118] K. Sasmal, B. Lv, Z. J. Tang, F. Chen, Y. Y. Xue, B. Lorenz, A. M. Guloy, C. W. Chu, *Physical Review B* **2009**, 79, 184516.
- [119] I. Todorov, D. Y. Chung, H. Claus, C. D. Malliakas, A. P. Douvalis, T. Bakas, J. He, V. P. Dravid, M. G. Kanatzidis, *Chemistry of Materials* **2010**, 22, 3916.
- [120] S. J. Cassidy, S. Ramos, S. J. Clarke, *Zeitschrift Fur Anorganische Und Allgemeine Chemie* **2014**, 640, 2889.
- [121] M. Tegel, M. Rotter, V. Weiss, F. Schappacher, R. Pöttgen, D. Johrendt, *Journal of Physics* **2008**, 20, 452201.
- [122] M. Tegel, S. Johansson, V. Weiss, I. Schellenberg, W. Hermes, R. Pöttgen, D. Johrendt, *Europhysics Letters* **2008**, 84, 67007.
- [123] M. Rotter, M. Tegel, I. Schellenberg, F. M. Schappacher, R. Pöttgen, J. Deisenhofer, A. Gunther, F. Schrettle, A. Loidl, D. Johrendt, *New Journal of Physics* **2009**, 11, 025014.
- [124] G. S. Collins, T. Kachnowski, N. Benczer-Koller, M. Pasternak, *Physical Review B* **1979**, 19, 1369.
- [125] H. J. Jakobsen, J. Skibsted, H. Bildsøe, N. C. Nielsen, *Journal of Magnetic Resonance* **1989**, 85, 173.

Full list of publications

Superconductivity up to 35 K in the iron platinum arsenides $(\text{CaFe}_{1-x}\text{Pt}_x\text{As})_{10}\text{Pt}_{4-y}\text{As}_8$ with layered structures

C. Löhner, T. Stürzer, M. Tegel, R. Frankovsky, G. Friederichs, D. Johrendt, *Angew. Chem. Int. Ed.* **2011**, *50*, 9195.

Metastable 11 K superconductor $\text{Na}_{1-y}\text{Fe}_{2-x}\text{As}_2$

G. Friederichs, I. Schellenberg, V. Doppel, L. Kienle, J. Schmedt auf der Günne, D. Johrendt, *Inorg. Chem.* **2012**, *51*, 8161. (Chapter 7)

Structural and magnetic phase transitions in triclinic $\text{Ca}_{10}(\text{FeAs})_{10}(\text{Pt}_3\text{As}_8)$

T. Stürzer, G. Friederichs, H. Lütkens, A. Amato, H.-H. Klauss, D. Johrendt, *J. Phys.: Condens. Matter* **2013**, *25*, 122203.

Superconductivity and Crystal Structure of the Palladium-Iron-Arsenides $\text{Ca}_{10}(\text{Fe}_{1-x}\text{Pd}_x\text{As})_{10}\text{Pd}_3\text{As}_8$

C. Hieke, J. Lippmann, T. Stürzer, G. Friederichs, F. Nitsche, F. Winter, R. Pöttgen, D. Johrendt, *Phil. Mag.* **2013**, *93*, 3680.

Electronic and Ionic Conductivity in Alkaline Earth Diazenides $\text{M}_{\text{AE}}\text{N}_2$

($\text{M}_{\text{AE}} = \text{Ca, Sr, Ba}$) and in Li_2N_2

S. Schneider, M. Mangstl, G. Friederichs, R. Frankovsky, J. Schmedt auf der Günne, W. Schnick, *Chem. Mater.* **2013**, *25*, 4149.

High-pressure synthesis and characterization of $\text{Li}_2\text{Ca}_3[\text{N}_2]_3$ - An uncommon metallic diazenide with $[\text{N}_2]^{2-}$ ions

S. Schneider, M. Seibald, V. Deringer, R. Stoffel, R. Frankovsky, G. Friederichs, H. Laqua, V. Doppel, G. Jeschke, R. Dronskowski, W. Schnick, *J. Am. Chem. Soc.* **2013**, *135*, 16668.

Oxygen-annealing effects on superconductivity in polycrystalline $\text{Fe}_{1-x}\text{Te}_{1-y}\text{Se}_y$

G. Friederichs, M. Wörsching, D. Johrendt, *Supercond. Sci. Technol.* **2015**, *28*, 095005.
(Chapter 4)

Conference contributions

Talks

G. Friederichs, D. Johrendt

Topotaktische Synthese von metastabilem NaFe₂As₂

Festkörper-Seminar Hirscheegg, Hirscheegg (Austria), 2011.

G. Friederichs, D. Johrendt

Soft Chemistry Approach – Metastable Na_{1-x}Fe_{2-y}As₂

EU-Project (Super Iron) summer school, Bad Schandau, Germany, 2013.

Poster

G. Friederichs, I. Schellenberg, R. Pöttgen, D. Johrendt

Topotactic synthesis and properties of metastable NaFe₂As₂

DFG Kick off Meeting, Dresden, Germany, 2011.

G. Friederichs, I. Schellenberg, V. Duppel, L.Kienle, J. Schmedt auf der Günne,
D. Johrendt

Metastable 11 K superconductor Na_{1-y}Fe_{2-x}As₂

International Workshop on Novel Superconductors and Super Materials, Tokyo,
Japan, 2013.

Curriculum Vitae

Personal Information

Name	Gina Maya Friederichs
Date of Birth	18 March 1986
Place of Birth	Dachau, Germany

Education

since 10/2010	Ph.D. thesis in inorganic solid state chemistry in the group of Prof. Dr. Dirk Johrendt, Department of Chemistry, Ludwig-Maximilians University Munich, Title: "Iron-based superconductors via soft chemistry"
12/2010	Römer-Award (Dr. Klaus Römer Foundation) in category Master thesis
3/2010 - 9/2010	Master thesis in the group of Prof. Dr. D. Johrendt, Ludwig-Maximilians-University Munich, Title: "Alternative synthesis routes to iron arsenide superconductors".
10/2005 - 9/2010	Bachelor/Master studies at the Ludwig-Maximilians University Munich. <i>B. Sc, M.Sc.</i>
9/1996 - 6/2005	Carl-Spitzweg-Gymnasium (secondary school), Germering. <i>Abitur</i>
9/1992 - 7/1996	Grundschule an der Kirchenstraße (primary school), Germering.